SLAC-R-495

A MEASUREMENT OF THE b QUARK FRAGMENTATION FUNCTION AT $\sqrt{Q^2} = 45.6$ GeV*

Eric Church

Stanford Linear Accelerator Center
Stanford University, Stanford, CA 94309

June 1996

Prepared for the Department of Energy
under contract number DE-AC03-76SF00515.

*PhD thesis, University of Washington

DISCLAIMER

University of Washington

Abstract

A Measurement of the b Quark Fragmentation Function at $\sqrt{Q^2} = 45.6$ GeV

by Eric D. Church

Chairperson of Supervisory Committee:

Victor Cook
Department of Physics

Presented here is a measurement of the b quark fragmentation function $D_b(x)$, taken from a sample of 504 semi-leptonic B decays which were selected from the $150,000$ Z^0 decays collected between 1993 and 1995 at the SLD at SLAC. The energy of each tagged B hadron is reconstructed using missing jet energy, based on the information from the lepton and a partially-reconstructed charm-decay vertex. Account is taken of the effect of primary orbitally excited mesons (B^{**}s). An iterative unfolding procedure is used which serves to effectively extract the true fragmentation function from the reconstructed B energy spectrum. The final result is shown to be compatible with many theoretical models. A comparison is made with other b fragmentation function measurements at 45.6 GeV, and this measurement is shown to be consistent with those results. The average scaled energy is found to be $\langle x_E \rangle = 0.697 \pm 0.017(stat) \pm 0.034(sys)$.

TABLE OF CONTENTS

LIST OF FIGURES

LIST OF TABLES

ACKNOWLEDGMENTS

I'm very fortunate and happy to have been able to achieve my goal of obtaining my PhD in experimental particle physics. I consider myself very fortunate to have been able to devote five years of my life to the study of physics at the University of Washington and at the Stanford Linear Accelerator Center. I am indebted to many people for helping me along the way.

A bigger thanks than I can ever give is owed to my parents, Hugh and Kathleen Church whose patience with my seemingly-endless pursuit of higher education has always been admirable. Their steady encouragement paved the way a long time ago. I have a great debt of gratitude to Vic Cook, my advisor, who's offered me the freedom to chart my own course from our first work together. I hope I have gained at least a small sense of his physics insight. I am also grateful to the members of the High Energy Physics Group at the University of Washington for input on this work, particularly to Joe Rothberg and Steve Wasserbaech. Thanks are owed to many of the great professors from the Particle Theory Group I'm lucky to have had as teachers: Peter Arnold, Lowell Brown, Steve Ellis, Ann Nelson and Larry Yaffe. The time I spent in their classes and seminars I count as some of the most enjoyable in my graduate career.

I would also like to thank the many talented people on the SLD experiment under whose tutelage I learned everything I know about experimental high energy physics and whose hard work has made my little study possible. More specifically, I am indebted to Gary Bower, Phil Burrows, Richard DuBois, Donatella Falciai, David Jackson, Tom Junk, Matt Langston, Giampiero Mancinelli, Dave Muller, Tom Pavel, Joe Perl, Homer Neal, Jim Quigley, Bruce Schumm, Eric Torrence, Eric Vella, Eric Weiss, Stephane Willocq, David Williams, and Jingchen Zhou. And Geordie Zapalac too, whose efforts formed the basis of this analysis.

Thanks go also to my physics colleagues at the University of Washington who've

helped make my years in graduate school hugely enjoyable. In particular, I thank Tim Peterson, Bill Schief, Pam Krauss (our IM ultimate legacy may never be topped), Steve Sutlief, Jon Eisenberg, Keith Clay and Hwi Kim. Especially, thanks go to my officemate John Putz, whose physics input has been very helpful and whose input in the form of discussions of non-physics matters has been even more appreciated. I will miss our deconstructions of various elements of popular culture and our sometimes-cruel, but always-fair, analyses of the problems of society, government and the people who hang out on the lawn outside our office window.

DEDICATION

This dissertation is dedicated to my wife and partner Andrea Ensign, who gave me the strength (and permission) to get my PhD.

Andrea's degree of patience and her encouragement have been greater than anyone should be allowed to ask. For her sacrifices – made for no obvious, foreseeable reward – I offer my greatest thanks, and all the love in my heart. (Thanks also for doing the bibliography.) I'm glad we'll always be together. To Emma too, who's been the greatest thing I've done with my life. Someday we'll have a house with a yard and a proper life.

Chapter 1

INTRODUCTION

1.1 Motivation

The work of many physicists in the 1960's through the 1980's led first to the formulation of the Standard Model of particle physics, and then to its extensive testing. In the late 1980's and into the 1990's with the construction and operation of the four experiments at the Large Electron Positron ring (LEP) in Geneva and SLAC's Large Detector (SLD) in California, the Standard Model has gained the status of *the correct* low energy theory[1]. These detectors each observe e^+e^- collisions at an energy of $\sqrt{s} = 91.2\ \text{GeV} = m_{Z^0}c^2$. They have tested Electroweak parameters of the SM to better than 1% accuracy [1, 2].

The Strong interactions, which are governed by the symmetry of SU(3), (and will get a rather thorough treatment in chapter 2) are a different matter. The SU(3) of color contains a much smaller number of parameters than the EW theory, due mainly to the absence of the complicated mechanism – called the CKM matrix – that allows for flavor changing in EW decays. The masses of the quarks arise from EW symmetry breaking, and so those parameters are also not contained in the SU(3) part of the theory. The only parameter of the Strong interactions is, in fact, α_S, or equivalently, Λ_{QCD} (see equation 2.4). However, in contrast to many of the 18+ parameters of the EW theory, it has been measured to only $\approx 5\%$ accuracy. This lack of precision is due, largely, to the phenomenon of *hadronization.* Hadronization is the process whereby the quarks and gluons of SU(3) turn into hadrons. To date there exists no exact formulation for this process. This too will be discussed in chapter 2. Essentially it means that the perturbative calculations come with an inherent fuzziness which will always prevent the levels of accuracy achieved by EW theory.

---

[1] low, here, means $\lesssim 100\ \text{GeV}$

Given this, it is important to try to parametrize our ignorance of various (for now) incalculable phenomena. An example of such an exercise is the measurement of the proton structure functions. There, in fact, one is at a loss to predict the shape of such functions, but is able to demonstrate nicely what's known as Altarelli-Parisi scaling violation if variation with Q, the relevant energy scale, is considered. This is a direct consequence of perturbative QCD. In exactly the same way, one is able to show that such scaling will apply to fragmentation functions. The perturbative QCD (pQCD) behavior of the fragmentation function must be considered one of the major motivations for this thesis. This will be made explicit in chapter 2.

Second, one is struck by the number of analyses which list as their largest systematic error the variation of the shape and/or mean of the fragmentation function. References [3, 4], studying B physics topics ranging from lifetimes to mixing parameters, all cite the b fragmentation function as their biggest single source of error.

Third, it is necessary in order to measure the b quark fragmentation function to measure the initial B energy in each event. Until recently it was common to read papers [5] in which a plot of the b fragmentation function was produced from a measurement of the mean B scaled energy $< x_E >$ alone. One measured the high end of a lepton spectrum (to ensure that the lepton came from a semi-leptonic B decay), then used a B decay model to determine the average boost necessary for the Bs to have produced such a spectrum, and then inferred the shape of the curve with the one parameter Peterson model. Only very recently have workers tried to actually measure the whole b fragmentation *function* [7, 6, 8] in a model independent way. This work furthers that effort. Also, as a practical matter, any technique that is able to measure the B energy well on an event-by-event basis is useful to other analyses – most notably B oscillation measurements, where the proper time $t = l/\gamma\beta$, with $\gamma = E/m_B$, must be known quite well [9, 3]. Such a technique is presented here.

1.2 Outline

In this chapter we will have many things to say about the Electroweak part of the lagrangian of what's known as the Standard Model of particle physics. A treatment of the Strong interactions of the Standard Model (Quantum Chromodynamics, or QCD) is reserved for chapter 2. In that chapter there will be a particular emphasis on the physical ideas that go into the four calculations to be compared in this analysis

against the measurement of the b quark fragmentation function. Chapter 3 presents a description of the detector with which our measurements was performed. Chapter 4 describes the way in which events were selected for this analysis, and Chapter 5 gives the details of the measurement and the final result.

1.3 Units

We employ in this thesis *natural* units: $\hbar = c = 1$, with $\hbar$ Planck's constant over 2π and c the speed of light. Units of length and 1/Energy will be used interchangeably, with $\hbar c = 0.197$ GeV·fm used to recover the relevant unit of measure.

1.4 Particle Physics

1.4.1 The Long View

The language of quantum field theory tells us that what we know to be the four fundamental forces[2] are in fact the results of the exchange of individual virtual particles with other particles. These exchanged particles are called gauge bosons or vector bosons (tensors, in the case of gravity), and their interactions with the fermions of which matter is made arise in various theories from the imposition of symmetries. One demands that under certain mathematical operations the physics described by the theory does not change. This is a symmetry. The tool for discovering the structure of Nature and making predictions about its behavior based on its symmetries is the lagrangian.

The idea that the equations of motion for a physical system are derivable from its lagrangian, is used heavily in modern physics and will be understood by those familiar with classical mechanics, where Newton's equation of motion $\vec{F} = m\vec{a}$, for example, is derivable from the lagrangian that describes the motion of a body in a particular potential. Similarly, an exploration of the symmetries of such a lagrangian reveals the possible existence of the conserved quantities energy, momentum and angular momentum. What is new in quantum mechanics is the quantization of the theory – imposing commutation relations between x and p. What is new, further, in relativistic quantum field theory is the extension from x to *fields* $\psi(x)$ and the

[2] namely, electromagnetism, gravity and the strong and weak forces

leap into Fock space, which allows particles to be created and annihilated by these fields with all possible four-momenta over all space-time. Such an approach is quite powerful and all evidence suggests it is directly connected with reality.

1.4.2 The Theory of the Electroweak Interactions, the Standard Model and Z^0 physics

Subsequent to work spanning the 1930's through the late 1950's when Gamow, Teller and Fermi, *et al.* were tackling the Weak interactions, it became clear that for reasons of unitarity, the concept due to Fermi of the 4-point "contact" interaction had to be abandoned in favor of the

introduction of a massive gauge boson. That is to say, the product of a coupling constant with dimensions, $G_F = 1.166 \cdot 10^{-5}$ GeV^{-2}, and various matter fields gave operators in the Hamiltonian that were of dimension higher than 4. At high energies the theory does not conserve probability – i.e. unitarity is violated. It was observed that a propagator just like the photon, but with mass, could be mediating the observed charged current Weak interactions and that the momentum of the process was low enough that it would in fact *appear* to be the act of a dimensionful coupling constant. The observation in 1973 of $\nu_\mu N \rightarrow \nu_\mu X$ neutral current events [10] implied the existence of the neutral gauge boson, the Z^0, as well. When the Z^0 was found [11] with the $W^\pm$ in 1983 at the CERN $p\overline{p}$ collider, UA1 detector, the predictions were born out.

However, it was also known that the addition of such massive gauge bosons to the theory destroyed the theory's gauge symmetry. Gauge symmetry is the idea that the lagrangian is unchanged under a certain class of simultaneous transformations in the fermion and gauge fields. However, this symmetry does not hold for massive gauge bosons. It is also true that just naively adding the required term to the lagrangian does not fix the unitarity violation[3].

It seemed reasonable to try to extend the success of QED to the domain of the Weak interactions, but immediately the presence of a mass term, $m_W^2 W_\mu W^\mu$, for the new bosons of the theory was seen to destroy gauge invariance. The next advance required the introduction of a new idea: the Higgs mechanism. The Higgs mechanism

[3] In QED, when gauge symmetry is enforced Maxwell's equations are unchanged and the electron is coupled to the photon according to a precise prescription. Quantum corrections to the electron's magnetic moment $g - 2$ have been calculated and verified to the 12^{th} significant digit [12].

begins with the introduction of a scalar (spin 0) particle to the theory. The scalar may (and does) gain a non-zero vacuum expectation value. In general, it may be shown that the gauge bosons which couple to the generators of the group which leave the vacuum invariant remain, themselves, massless. But those gauge bosons which couple to the generators which do not leave the vacuum invariant gain a mass. Work continued on this front, culminating in the mid-1970's with the Weinberg-Glashow-Salam model of the Electroweak (EW) interactions. This theory, together with the SU(3) of the Strong interactions forms what we call the Standard Model, $SU(2)_L \otimes U(1)_Y$, where the L and Y stand for left and hypercharge, respectively, and the SU and U describe the group under which we demand invariance.

The Weinberg-Glashow-Salam model is a wonderful piece of work, in which a scalar is introduced in the SU(2) part of the theory which gains a vacuum expectation value (vev) in just the right way so as to leave the photon massless and make the $W^{\pm}$ and Z^0 massive, which is what we asked for initially. Additionally, however there are other beneficial consequences: (1) the Higgs mechanism will give all the leptons and quarks their masses; (2) the appropriate placement of the leptons into SU(2) doublets reproduces the famous parity-violating nature of the Weak interactions; (3) the theory is magically free of so-called triangle anomalies, due to a combination of the placement of quarks and leptons into doublets and singlets, their electric charges and the fact that the quarks have three colors each (the first of at least three arguments for colored quarks!); (4) and finally, fiddling with the parameters of the three generation model (which is the number seen in Nature) to the extent allowed by constraints on conservation of probability (unitarity), allows one to accommodate the observed suppression of flavor-changing neutral currents (the GIM mechanism) and (seemingly) CP violation.

Of relevance to physics at the Z^0 is, for example, the production rate for $b\bar{b}$ pairs, $\Gamma(Z^0 \rightarrow b\bar{b})$. The relevant coupling arises from two parts of the lagrangian: one where the doublet containing the left-handed b (Q_b in equation 1.1 below) interacts with the SU(2) *and* U(1) gauge fields and the other part where the right-handed b (b_R in 1.1 below) interacts with just the U(1) gauge field. The whole process amounts to taking the Dirac equation, and making it gauge invariant in the usual way to create QED, but with the gauge invariance enforced under a bigger group of parameters which are combined in the appropriate linear combination that reproduces the Weak

interactions (and the fermion mass is obtained from the Higgs sector, as mentioned above):

$$\mathcal{L}_{Weak_b} = \overline{Q}_b \not{\mathcal{D}}_{2\otimes 1} Q_b + \overline{b}_R \not{\mathcal{D}}_1 b_R, \tag{1.1}$$

where here the $\not{\mathcal{D}}$s are the covariant derivatives contracted with the Dirac γ matrices, $\not{\mathcal{D}} = \mathcal{D} \cdot \gamma$. After symmetry breaking – i.e. the gaining of the vev by the Higgs scalar, and the identification of the linear combination of SU(2) and U(1) fields that *does* pick up a mass with the Z^0 – this looks like

$$\mathcal{L}_{Zbb} = Z^\mu \overline{b}[g_v \gamma_\mu - g_a \gamma_5 \gamma_\mu] b \tag{1.2}$$

with

$$g_v = -\frac{1}{2} + \frac{2}{3}\sin^2\theta_W \quad \text{and} \quad g_a = -\frac{1}{2}. \tag{1.3}$$

One can re-arrange the $g_v\gamma_\mu$ and $g_a\gamma_5\gamma_\mu$ so that instead we can see the couplings of the Z^0 to left- and right-handed bs and $\overline{b}$s separately. Suffice it to say that the inequality of production of left- and right-handed quarks leaves them with a net polarization that could in principle be measured[4]. Similarly, this inequality of left- and right-handed couplings produces an asymmetry of production of bs along the e^- beam direction compared with the opposite direction. This is called $A_{FB}^{(b)}$. It and similar observables yield measurements of $\sin^2\theta_W^{\text{eff}}$ [14, 2],

$$\sin^2\theta_W^{\text{eff}} = g_1/(g_1^2 + g_2^2)^{\frac{1}{2}}, \tag{1.4}$$

and other electroweak parameters.

In general, to calculate scattering amplitudes, one carefully follows Feynman rules – instructions for re-creating products of specific terms in the lagrangian and inserting the appropriate propagators (all in momentum space).

The full cross-section for $e^+e^- \to Z^0/\gamma \to$ anything, may be obtained at leading order from a consideration of Feynman diagrams of the type in figure 1.1. Upon doing this, figure 1.2 is obtained, showing the big resonance at the Z^0 pole. The width of the $/Z$ may be computed by generalizing the calculation considered above, $\Gamma(Z^0 \to b\overline{b})$, to include all fermions, $\Gamma(Z^0 \to f^+f^-)$.

---

[4] However, evidence suggests that the polarization of the partons is lost after the hadronization process [13].

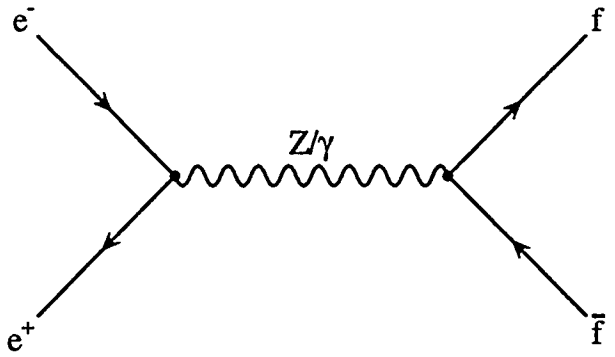

Figure 1.1: The leading order Feynman diagram for production and decay of the Z^0 at the SLD. The extra diagram necessary for consideration of the special case of $f = e$ is shown in the lower right hand corner of figure 3.10 (where the photon-exchange diagrams which we generally ignore are also shown).

The above recipe applies equally to efforts to derive *loop* corrections to various processes, with the added instruction to integrate over all internal loop momenta. Exactly this procedure could lead in a more boring thesis into a long discussion of the process of *renormalization* – a property that all theories must be careful about satisfying. Here, we merely note that the SM is renormalizeable and anomaly free.

The bottom line is that the value of $\sin^2\theta_W^{\text{eff}}$ taken from SM predictions for $A_{FB}^{(f)}$, where f is the energetically available fermions, along with that taken from other electroweak observables are all consistent with each other. Measurements of asymmetries, productions rates, the Z^0 width to hadrons, etc. all seem to demonstrate the correctness of the SM. Especially gratifying is the recent discovery of the top quark [15, 16], leaving the Higgs(es) as the only SM particle(s) undiscovered.

1.4.3 Quarks in the Standard Model

In the 1960's Gell-Mann and Zweig, among others, participated actively in the exciting endeavor to catalogue the many particles that were being discovered at that time. This essentially consisted of looking for bumps in cross-sections of varying-energy fixed-target experiments: $\pi^{\pm}$ and $K^{\pm}$ on p, $\overline{p}$ on p, p on p. These were interpreted as new particles.

By observing the decay products of these (sometimes very-short lived) particles,

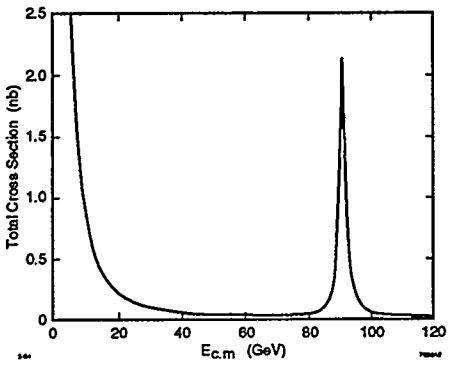

Figure 1.2: $\sigma(e^+e^- \to \mu^-\mu^+)$ vs. $\sqrt{s}$

spin, charge and *isospin* quantum numbers were assigned. It became clear (to Gell-Mann) that there was an underlying structure to the picture. If one postulated the existence of fractionally-charged, spin $\frac{1}{2}$ quarks and anti-quarks and combined them in $q\overline{q}$ and qqq groups with each q assigned a quantum number called *flavor*, with $f = u, d$ or s, the resulting *hadrons* were seen to be members of the allowed group theoretical multiplets. Gell-Mann termed this $SU(3)_{\text{flavor}}$ model the Eightfold Way. Vaguely motivated mass relations were seen to work well, and gave predictive power to the model. Most of the *uds* hadrons were soon found and catalogued[5]. The picture was very tidy and illuminating and gave the first evidence for the constituent quarks.

The true theory of the interactions of the quarks and gluons, SU(3) of color (bearing no relationship to $SU(3)_{\text{flavor}}$), was yet to come. Its discussion consumes much of chapter 2. It will be seen to complete the Standard Model, $SU(3)_C \otimes SU(2)_L \otimes$

[5] Inclusion of the c and b quarks was done later, owing to their significant masses.

$U(1)_Y$.

1.4.4 Beyond the Standard Model

One hopes that particle physicists will be able to explain physics at the energy $\approx M_{Planck} \approx 10^{19}$ GeV – where gravity, electromagnetism, the Weak interactions and the Strong interactions may all be unified – and the way in which physics at lower energies has come into being. In this regard the SM is only a small piece of the puzzle.

Despite its success, the SM lacks a certain elegance due to its sheer number of free parameters (18+). No explanation is made for charge quantization, such as $Q_e = -\frac{3}{2}Q_u$. It is evidently not complete in the sense that it is made up of a direct product of three groups, rather than one large one. And finally, the Higgs sector as it stands has one great difficulty. Namely, corrections to the Higgs mass – due to loop diagrams – diverge quadratically and require repeated fine-tuning with the inclusion of more and more loops in the calculation. This is the naturalness problem [17]. We turn to a discussion of its cure here.

Essentially one has two choices: (1) Adopt the notion of Technicolor which proposes that the Higgs itself is a composite object made up of so-called techni-quarks, each labeled with a techni-color index. In this scheme one imposes confinement as in QCD in order to achieve the spectrum of Higgses desired. *Or* (2) Adopt the notion of Supersymmetry which proposes that there exist particles which couple to the Higgs with the same strength as it couples to itself, but whose loops give contributions of the opposite sign, *e.g.* fermions of roughly the same mass. Technicolor, is considered to be in deep trouble due to the corrections it requires – but that are not seen – to the ρ parameter of the Electroweak interactions [18]. However, there remains much hope for Supersymmetry.

Supersymmetry accomplishes what was once thought to be impossible [19]: it combines both internal symmetries of the fields with the Poincarè symmetries (invariance under boosts, rotations, translations). It is a finite theory (except for wave-function renormalization) that removes the need for the subtraction of infinities that made people as important as Dirac uncomfortable [18]. In particular it solves the fine-tuning problem mentioned above with the Higgs. Its main consequence is that every known boson and (Weyl) fermion has a super-partner of the same mass. Since

it is clear from the absence of such particles, that such a situation does not exist[6], Supersymmetry (SUSY) must be broken. SUSY can, in fact, be gracefully broken at the desired scale [18]. Thus, for it to be a true symmetry of Nature and to simultaneously solve the naturalness problem – the reason for which we initially invoked it – one requires the discovery of super-partners at the mass scale $\lesssim 1$ TeV. Some such particles are guaranteed to be found at detectors which are currently being built [20] if this is the case.

It is a compelling idea, which may or may not be correct. We proceed with its discussion here only to outline the steps that remain for any candidate theory with ambitions of providing the full picture of particle physics.

There is next the need for unifying the three groups of the Supersymmetric Standard Model. This is called Grand Unification. It is the next step of any physics beyond the Standard Model. There is in fact evidence for Grand Unified SUSY already, if one chooses to interpret the unification of the running coupling constants at a high energy scale $M_{GUT} \approx 10^{16}$ GeV [21] as such evidence. It is also true that non-extended, non-Supersymmetric Grand Unification fails to unify the coupling constants at an energy which is consistent with the bound on proton decay, and thus it is dead. The next step would be to make local the parameters of SUSY transformations, just as is done with gauge symmetries. This has the extremely nice consequence of incorporating gravity. Last, it is also true that local SUSY can be made to be a consequence of super*string* theories, which has the benefit of being able to avoid the problems of the quantization of a spin-2 field like gravity [22]. It should be re-stated here that Supersymmetry is certainly only at the level of a candidate theory that can satisfy our lofty goals of unifying the four known forces, and we have pursued it only as an academic exercise. Even if evidence surfaces for super-partners in the next ten years, SUSY Grand Unification would certainly have the unattractive feature of not being verifiable in the foreseeable future, due to the enormous technological hurdles that will need to be passed to achieve an energy 13 orders of magnitude higher than that which current experiments provide.

---

[6] *i.e.* the masses of the spartners are so heavy as to not have been observed yet

Chapter 2

INTRODUCTION TO QCD AND B PHYSICS

2.1 QCD

2.1.1 Theoretical Motivation

In chapter 1 we discussed the conjecture by Gell-Mann that the observed hadrons were in fact bound states of the more fundamental entities that he called quarks. One of the most important hadrons to be discovered was the Ω^- baryon, the existence of which was predicted by Gell-Mann's model. All of the quantum numbers of the three quarks are identical in the absence of color. The Pauli exclusion principle requires that if an object is to be a bound state of fermions, the fermions must not be identical. That is, the overall wavefunction must be anti-symmetric. This leads to the invention of color and the assignment of three colors of quarks.

Given these results along with some more to be presented in the next subsection and presuming that the fermions reside in the fundamental representation in gauge theories as usual, $SU(3)_C$, a non-abelian theory of three colored quarks and eight colored, self-interacting gluons, emerges as a candidate theory for the strong interactions.

Soon after this formulation, the notion that Quantum Chromodynamics (QCD) could be the theory of the strong interactions became a tenable one with the discovery [23] in 1973 of "asymptotic freedom" and "infrared slavery" in non-Abelian gauge theories. That is, the coupling constant of QCD describes freely interacting quarks (asymptotic freedom) at small distances that are never allowed to separate to large distances (infrared slavery).

The idea that our constituent quarks and antiquarks are unable to be separated by more than ≈ 1 fm explains in a qualitative way why the physically realized states are bound quarks, or hadrons. Further, it is interesting that in a naive perturbative approach, enforcing color confinement – the postulate that any combination of quarks, which reside in the 3 representation of SU(3) and the antiquarks, which reside in

the $\overline{3}$, must combine to be in the 1 of whichever representation is formed by the combination – an idea for which there is compelling justification [24, 25], but no proof, leads directly[1] to the mesons ($q\overline{q}$) and baryons(qqq).

2.1.1.1 A Possible Explanation of Hadronization: The QCD Vacuum as Color Magnetic Superconductor

At the low energy scale ($\lesssim 10$ GeV) the fact that the realized states are hadrons, and not the quarks, leads to a few questions. 'Why is this so?' and 'How does this affect our ability to explore QCD?' are two among them. We turn to the first question here. The structure of the QCD vacuum is a subject of intense recent work [32, 27] in quantum field theory. Rosenzweig in [28] reviews progress on the idea [29, 30] that the QCD vacuum is a color magnetic superconductor. One has in mind in such a picture the mechanism of superconductivity in which, under certain conditions, actual electron pairs form and become the relevant degrees of freedom of the system. The resulting scalar field can acquire a negative vacuum expectation value in the usual way, and the effect is that the photon becomes massive. (A nice review may be found in [31].) From this and Maxwell's equations one can demonstrate the expulsion of the magnetic field from the interior of a superconductor (the Meissner effect via the London equations). Magnetic superconductivity requires the formalism of *dual* QCD. With it one can demonstrate the expulsion of the color *electric* field [32] subsequent to the breaking of a symmetry similar to the one broken in the usual BCS theory of superconductivity (the formation of "condensates"). Other nice consequences are that a linear potential between quark-antiquark pairs arises, as do Regge trajectories where the angular momentum J and E are related in the usual way, $J \sim E^2$. The implication of this expulsion of the color electric field is that any colored particle (quark) that somehow does find itself in this medium, which we claim now fills all of space, must find the appropriate colored quarks with which to form a color singlet. Hence, color confinement. It is a very nice idea which, when its various hurdles are overcome, will probably turn out to be right, according to Rosenzweig in [28], who says "If Nature used a good idea once (BCS theory of superconductivity), why not use it again?"

---

[1] by which we mean here that if one considers the hyperfine 2-body interaction the configurations that have the lowest energies are $q\overline{q}$ and qqq [26].

At the high energy scale ($\gtrsim 10$ GeV) asymptotic freedom in Yang-Mills theories – of which SU(3) is one – implies the existence of freely interacting quarks and gluons whose behavior is calculable in perturbation theory (perturbative QCD or pQCD). This is handy, as otherwise we have only a vastly complicated numerical problem to solve with a computer, and we quit and go home or pursue the field of lattice QCD. pQCD ideas will form the bulk of the rest of this chapter.

2.1.2 QCD Experimental Verification

Experimentally, the quantities

$$R = \frac{\Gamma(e^+e^- \to \gamma \to q\bar{q})}{\Gamma(e^+e^- \to \gamma \to \mu\bar{\mu})} \tag{2.1}$$

(see figure 2.1) and

$$\Gamma(\pi^0 \to \gamma\gamma), \tag{2.2}$$

the ratio of hadronic to muonic production and the π^0 decay rate respectively, require that we have three colors of quarks. The calculated value of equation 2.1, whose value is given in figure 2.1, is seen to be simply 1/3 too small if the number of colors, $N_c = 1$. And in the calculation of the π^0 decay rate the result depends on the number of types (colors) of quarks that are allowed to run around inside the fermion loop in the Feynman diagram that describes the decay.

Experiments at SLAC [34] in 1972 first showed the existence of the asymptotically free behavior of quarks in Bjorken scaling. That is, (for a particular value of x) the structure functions that parametrize our ignorance of the internal structure of the proton are independent of the exchanged 4-momentum squared. This observation provided the first evidence for the existence of constituents inside the proton. Simultaneously, (for all other x than the one magical one at which scaling takes place, $x \approx 0.25$) scaling *violation* was seen as q^2, the 4-momentum squared, was increased, effectively probing the proton at ever-smaller length-scales. These experiments, taken together, largely ushered in QCD as the correct theory of the strong interactions.

The QCD lagrangian

$$\mathcal{L} = \frac{1}{4}F^a_{\mu\nu}F^{a\mu\nu} - \bar{\psi}_{f,i}[i(\gamma^\mu\partial_\mu\delta_{ij} - gA^{a\mu}\lambda_{a_{ij}}\gamma_\mu) - m_f]\psi_{f,j} \tag{2.3}$$

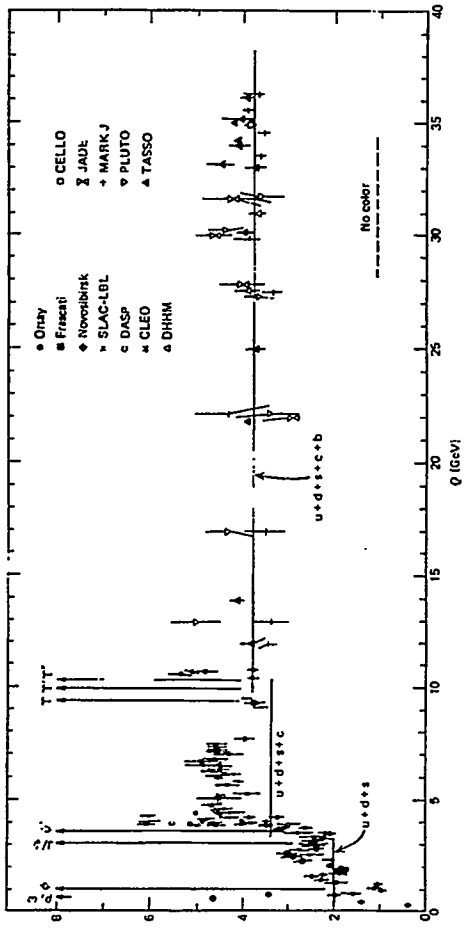

Figure 2.1: $\Gamma(e^+e^- \to \text{hadrons})/e^+e^- \to \mu^+\mu^-)$ as a function of $Q = \sqrt{s}$. Reprinted from [33].

where

$$F^a_{\mu\nu} = \partial_\mu A^a_\nu - \partial_\nu A^a_\mu + g f^{abc} A^b_\mu A^c_\nu$$

with the λs obeying the SU(3) algebra,

$$[\lambda^a_{ij}, \lambda^b_{jk},] = f^{abc}\lambda^c_{ik}.$$

f^{abc} are the structure constants of SU(3). The sum over all 6 flavors, d,u,s,c,b,t is implicit in the repeated index f. The color indices i, j run from 1 to 3 and a, b, c run from 1 to 8. The CP-violating θ term and gauge-fixing terms are omitted for simplicity.

Before embarking next into a discussion of a particular perturbative calculation, we should be clear about the region of validity of such a calculation. We need $\alpha_S(\mu) \equiv g^2/4\pi \ll 1$, where μ specifies the particular energy at which the *running coupling*, α_S is to be evaluated. To first order[2]

$$\alpha_S(Q^2) = \frac{4\pi}{\beta_0 \ln(Q^2/\Lambda^2)} \tag{2.4}$$

$$\beta_0 = 11 - \frac{2}{3}n_f \tag{2.5}$$

with n_f the effective number of quark flavors, 5 in this analysis. We see that for energies $Q \gg \Lambda \approx 200$ MeV perturbation theory will be valid. Deep inelastic scattering, to which we turn in the next section, is done in a "perturbatively safe" regime.

2.2 *Scaling Violations – The GLAP equations*

2.2.1 *Deep Inelastic Scattering*

It is instructive to look a little into the formalism and lessons of deep inelastic scattering (DIS) to understand a general feature that crops up in most perturbative QCD (pQCD) calculations: scaling violations.

The picture is a well-known one (figure 2.2): we bombard a proton with a photon that is radiated from the incident e^- and smash the proton into tiny bits, X. The matrix element squared, $|\overline{\mathcal{M}}|^2$ is calculated by observing that $\mathcal{M}$ consists of the product of the leptonic current j^μ_{lep}, the photon propagator $\xi_{\mu\nu}/(q^2 + i\epsilon)$ with its momentum q, and the hadronic current j^ν_{had} (up to the usual factors that are unimportant for this discussion) as

$$\mathcal{M} \sim j^\mu_{lep} \frac{\xi_{\mu\nu}}{q^2 + i\varepsilon} j^\nu_{had}.$$

$\mathcal{M}$ must be squared, summed over final state spins, and averaged over initial state spins. The leptonic part is handled straightforwardly using Dirac spinors,

$$j^\nu_{lep} j_{\sigma lep} = \overline{u}(p)\gamma^\nu u(p')\overline{u}(p)\gamma_\sigma u(p').$$

---

[2] For a look at the amount of work (there are 59 more diagrams to think about) that goes into calculating just the *second* order expression for α_S see [35].

However, since the quarks are not free we must use a more general form for the hadronic current. We write the most general tensor that is consistent with charge conservation, $q \cdot j_{had} = 0$, and parity conservation, so that after squaring and summing and averaging over spins

$$j^{\nu}_{had} j^{\sigma}_{had} = W_{\nu\sigma} = -W_1(g^{\nu\sigma} - q^{\nu}q^{\sigma}/q^2) + \frac{W_2}{M^2}(P^{\nu} - \frac{P \cdot qq^{\nu}}{q^2})(P^{\sigma} - \frac{P \cdot qq^{\sigma}}{q^2})$$

where $q = p'_e - p_e$ is the four momentum transfer and P^{μ} is the nucleon four momentum, which has only a time-component in the lab frame. $F_1 = MW_1$ and $F_2 = \frac{P \cdot q}{M} W_2$ are called structure functions and are functions of $q =$ and $\nu = E' - E = \frac{P \cdot q}{M}$, the momentum transfer and the energy loss of the electrons, respectively. Upon comparison to point-like scattering and going to the $Q^2 \to \infty$ limit with $x = \frac{Q^2}{2P \cdot q}$ fixed, we can identify x as the fractional momentum of the proton originally carried by the struck quark and write F_1 and F_2 as functions of x and the quark distribution functions (figure 2.3) q_i. Specifically,

$$2xF_1(x) = F_2(x) = \sum_i e_i^2 x q_i(x), \tag{2.6}$$

showing the sum over each quark flavor weighted by its charge e_i and its momentum fraction$x$. The quark distribution functions obey energy conservation

$$\sum_i \int_0^1 dx x q_i(x) = 1. \tag{2.7}$$

When we consider the effects of QCD, namely the diagrams in figure 2.4, plus all other order α_S^1 diagrams – which cancel the infrared singularities[3] that will arise upon doing the phase space integration – F_1 and F_2 become functions of not just x but also Q^2 and are modified according to

$$\frac{F_2(x, Q^2)}{x} = \sum_i e_i^2 \int_x^1 \frac{dy}{y} q_i(y)[\delta(1 - \frac{x}{y}) + \frac{\alpha_S}{2\pi} P_{q \to qg}(\frac{x}{y}) \ln(\frac{Q^2}{\mu^2}) + \ldots] \tag{2.8}$$

where the dots represent a similar term from the gluon "Compton" diagrams. μ is introduced to cutoff the lower limit of the p_T phase space integral, and $P_{q \to qg}$, $P_{q \to gq}$, $P_{g \to gq}$ and $P_{g \to gg}$ are called *splitting functions.*

[3] as they must by the Kinoshita-Lee-Nauenberg (KLN) theorem [36]

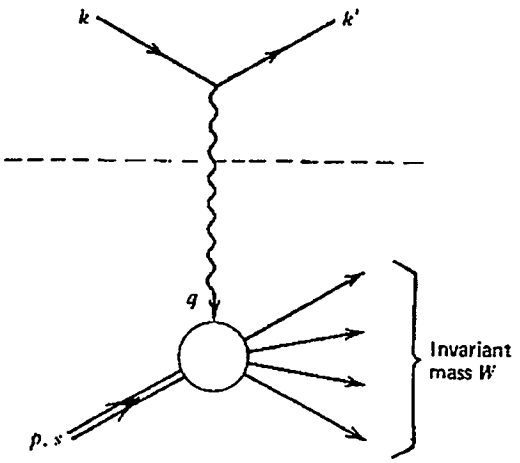

Figure 2.2: Deep Inelastic Scattering.

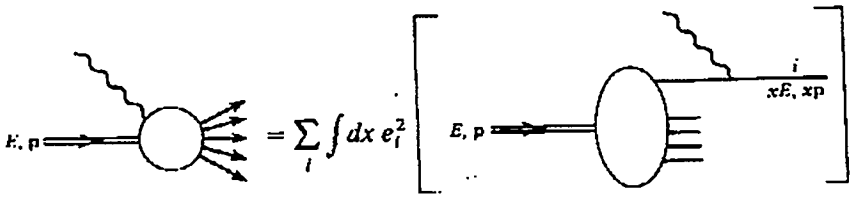

Figure 2.3: Deep Inelastic Scattering: the parton view.

Taking the derivative of the above equation to see the behavior with Q^2 of the unknown "bare" quark and gluon distribution functions, $q_i(x,Q^2)$ and $g(x,Q^2)$, the value of these functions at one energy gets related to the value at another by the so-called Altarelli-Parisi equations[4]

$$\frac{dq_i(x,Q^2)}{d\ln(Q^2/\Lambda^2)} = \frac{\alpha_S}{2\pi}\int_x^1 \frac{dy}{y}[q_i(y,Q^2)P_{q\to qg}(\frac{x}{y}) + g(y,Q^2)P_{g\to q\bar{q}}(\frac{x}{y})] \qquad (2.9)$$

and

$$\frac{dg(x,Q^2)}{d\ln(Q^2/\Lambda^2)} = \frac{\alpha_S}{2\pi}\int_x^1 \frac{dy}{y}[\sum_i^{n_f} q_i(y,Q^2)P_{q\to gq}(\frac{x}{y}) + g(y,Q^2)P_{g\to gg}(\frac{x}{y})]. \qquad (2.10)$$

[4] or Gribov, Lipatov, Altarelli, Parisi (GLAP) equations, as they're known in some circles.

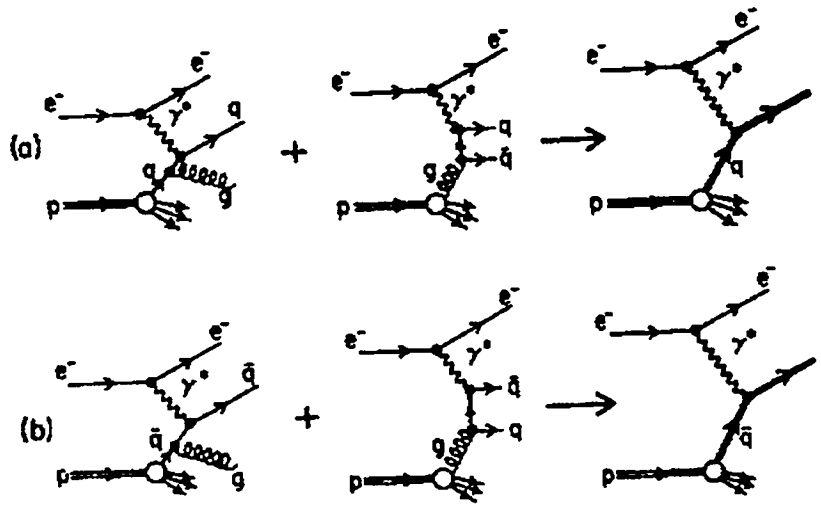

Figure 2.4: Deep Inelastic Scattering: QCD effects. The "Compton" gluon diagrams are the second in each of the lines (a) and (b) above.

The i runs over the energetically available quark flavors.

Figure 2.5 shows deviations from scaling according to equations 2.9 and 2.10, which are ingredients in 2.8. Last, we want to remark that in DIS the momentum transfer is space-like ($q^2 < 0$ in the Bjorken metric).

2.2.2 Fragmentation

Turning to fragmentation functions, here always in the context of e^+e^- →hadrons, with n_f the number of flavors, calling $x = E_h/Q$ the momentum fraction of any particular hadron with respect to the initial quark energy $E_{beam} = Q$, and $D^h_{q_i}(x)$ the probability that quark q_i will fragment into hadron h carrying fraction x of the initial quark energy $Q = \sqrt{s}/2$, then *in the naive parton model* the cross-section for production of a hadron with scaled energy x in e^+e^- annihilation is

$$\frac{d\sigma}{dx} = 3\sigma(\mu\mu)\sum_{i=1}^{n_f} e^2_{q_i}(D^h_{q_i}(x) + D^h_{\bar{q}_i}(x)) \qquad (2.11)$$

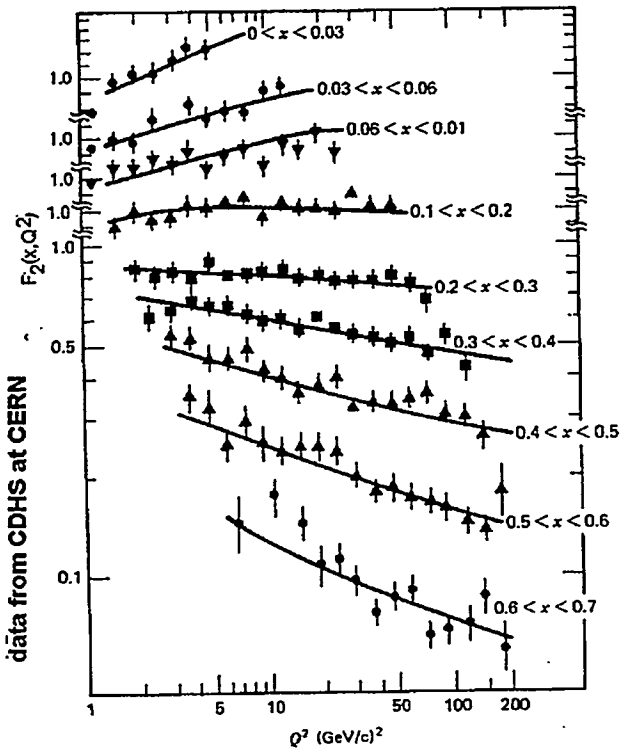

Figure 2.5: GLAP scaling violation in DIS, as reprinted from reference [33].

with energy conservation requiring

$$\sum_{\text{all h}} \int_0^1 dx x D_{q_i}^h(x). \tag{2.12}$$

In QCD (departing from the naive parton model) one allows for the processes shown in figure 2.6. Calculating these in pQCD in the same careful way as in DIS and similarly including virtual corrections in order to satisfy KLN[5] one arrives at an expression for $\frac{d\sigma(Q^2)}{dx}$ which, as we've indicated, is dependent on Q^2. The expression is lengthy and full of regularization[6] method-dependent terms along with the inherently non-perturbative, incalculable "bare" fragmentation functions. And so we do not

[5] See [35] for an excellent discussion of the KLN theorem both in general and in the context of e^+e^- annihilation.

[6] That is to say, in order to fix the infrared divergences which result from doing massless QCD (or even QCD in the presence of masses which are below the value of Λ_{QCD}) one must regularize

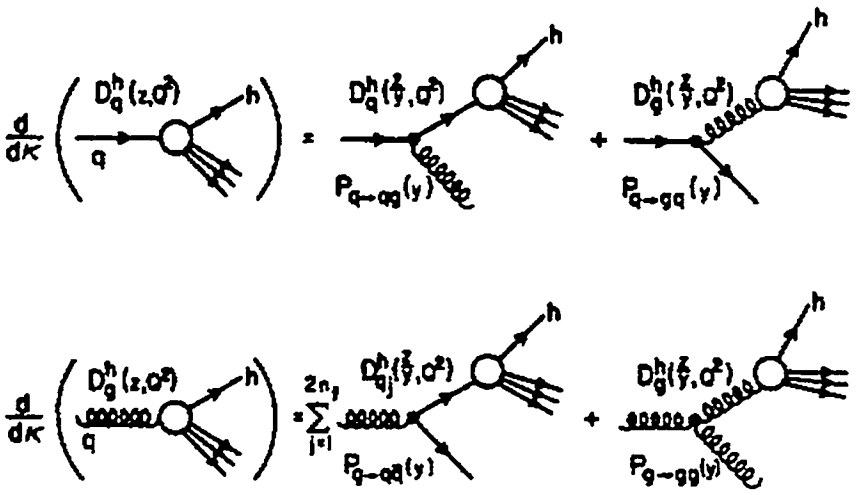

Figure 2.6: Fragmentation: QCD effects. This is a pictorial representation of equation 2.14.

write this expression here. What is germane are two things: (1) when gluon emission is considered equation 2.11 gains a term proportional to $D_g^h(x,Q^2)$, and (2) after shuffling the infrared infinities into bare quantities and taking the derivative with respect to $\ln \frac{Q^2}{\Lambda^2}$ we have for $D_q^h(x,Q^2)$ and $D_g^h(x,Q^2)$:

$$\begin{aligned} \tau &= \ln Q^2/\Lambda^2 && (2.13) \\ \frac{dD_q^h(x,Q^2)}{d\tau} &= \frac{\alpha_S}{2\pi}\int_x^1 \frac{dy}{y}[D_q^h(y,Q^2)P_{q\to qg}(\frac{x}{y}) + D_g^h(y,Q^2)P_{q\to gq}(\frac{x}{y})] && (2.14) \\ \frac{dD_g^h(x,Q^2)}{d\tau} &= \frac{\alpha_S}{2\pi}\int_x^1 \frac{dy}{y}[\sum_{j=1}^{2n_f} D_{qj}^h(y,Q^2)P_{g\to q\bar{q}}(\frac{x}{y}) + D_g^h(y,Q^2)P_{g\to gg}(\frac{x}{y})]. \end{aligned}$$

with

$$P_{q\to qg}(z) = P_{q\to gq}(1-z) = \frac{4}{3}\frac{1+z^2}{1-z^2}$$

---

one's integrals, *i.e.* quantify the size of the resulting infinities in terms of a parameter that is taken later to zero in a consistent way. Two popular choices are the massive gluon scheme and dimensional regularization, where m_g goes to zero at the end of the day and $\epsilon = 4-d$ similarly is taken to zero, with d the number of dimensions in which the integral is performed.

$$P_{g\to gg} = \frac{6(1-z+z^2)^2}{z(1-z)}$$
$$P_{g\to q\bar{q}} = \frac{1}{2}(z^2+(1-z)^2) \qquad (2.15)$$

the non-regularized splitting functions.

This is essentially GLAP scaling violation again (compare to equations 2.9 and 2.10), but now in a region of momentum transfer that is time-like ($q^2 > 0$) – opposite to that in DIS. Close inspection reveals that the Ps are multiplied by Ds that don't exactly correspond to the q_is and gs of equations 2.9 and 2.10.

The above discussion of scaling violations *à la* the GLAP equations was given to demonstrate the deep connection between QCD at e^+e^- machines and in DIS, where the subject was born. Even in principle, SLD can only place one point on the plot that demonstrates scaling violations in fragmentation, since the center of mass energy is fixed at $s = 4Q^2 = m^2_{Z^0}$. Thus, that is not done in this analysis. The ingredients required for this exercise are the individual quark fragmentation functions, which are only crudely known for the c quark, and are entirely modeled from a Monte Carlo study for the *uds* quarks. Reference [37] has done this exercise in reverse. They have taken the various quark fragmentation functions at a particular energy (Q^2) and evolved them with the GLAP equations to a lower energy and extracted $\alpha_S(m_Z)$, which is in accord with this parameter taken from other analyses. This success demonstrates the correctness of QCD in the second of two totally separate regions of q^2. Figure 2.7 displays the similarity between the observed scaling violations in each of several different experiments.

2.3 Motivation for Measurement Revisited

With an appreciation of GLAP scaling violations in hand, we are ready to review the QCD implications of the measurement of the b quark fragmentation function. One of the leading contributions to the error in the above-described procedure for extracting α_S is the uncertainty of the shape of $D_b^h(x, Q^2{=}m_Z^2/4)$, the b quark's fragmentation function [37]. It is found that small variations in the fragmentation function at $m_{Z^0}/2$, when evolved, leads to large variations in the extracted α_S. This provides motivation to better measure this quantity. Also, at a future, higher $\sqrt{s}$ e^+e^- machine where flavor separation is possible one will be able to examine the use of the GLAP

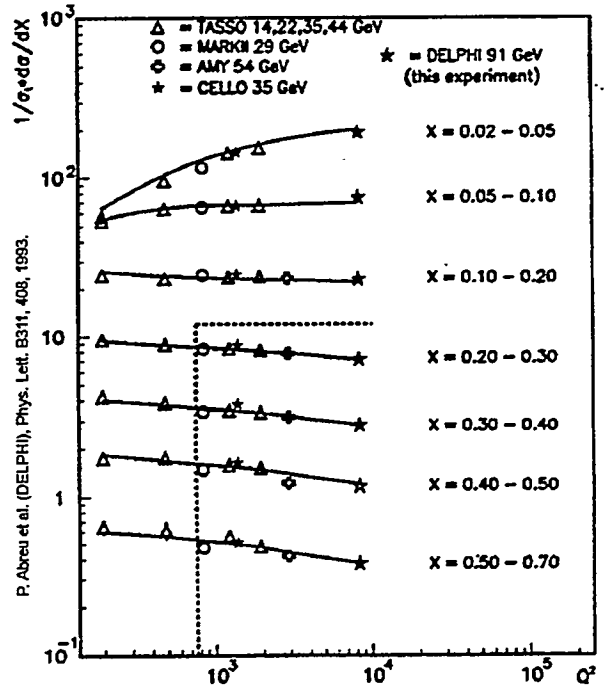

Figure 2.7: GLAP scaling violation in fragmentation. Compare to figure 2.5. $1/\sigma_t \cdot d\sigma/dX$ is the total, normalized, charged, hadronic cross-section. It contains all the quark fragmentation functions. See equation 2.11 for the lowest order in α_S expression for this quantity. The higher-order-in-α_S terms cause these curves to bend, in the way shown here, with Q^2.

equations to evolve just the b quark fragmentation function from $D_b^h(x, Q^2 = m_Z^2/4)$ to $D_b^h(x, Q^2 = s/4)$. This is in contrast to what can be done currently, namely evolve $\frac{d\sigma(Q^2)}{dx}$ which contains $D_b^h(x, Q^2)$ as just one of many ingredients. For this, one will desire a well-measured $D_b^h(x, Q^2 = m_Z^2/4)$.

2.4 *The Calculations of* $D_b^h(x, Q^2)$

Here we wish to discuss the calculations that will be compared to the final $D_b(x)$.

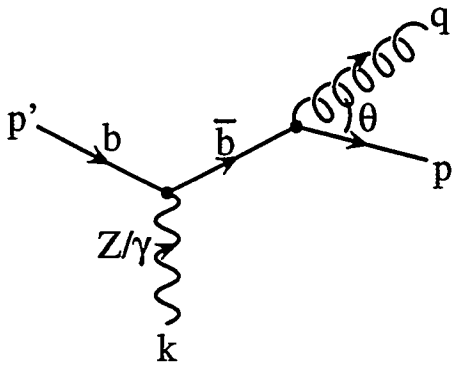

Figure 2.8: Gluon emission from a $\bar{b}$ quark for the calculation of the heavy quark "dead cone."

2.4.1 pQCD with Resummation

We made the claim on page 19 that the bare fragmentation functions are inherently non-perturbative. While this is reasonable for the light quarks, one might imagine that the unknown process by which a ≈ 4.7 GeV b quark picks up an antiquark out of the vacuum to form a B is unaffected by the non-perturbative regime – which corresponding to energies below ≈ 200 MeV. The idea that b quarks are immune to physics at such scales is justified by a quick check of the behavior of the propagator in the process in figure 2.8. The $b\bar{b}$ pair is created in the usual electroweak process, and then one of the (off-shell) quarks radiates a real gluon. The b propagator $\frac{i}{i(\not{p}+\not{q})+m_b} \sim \frac{1}{(p+q)^2-m_b^2}$, where the usual $\pm i\varepsilon$ in the denominator has been suppressed for simplification. Since $p^2 = m_b^2$ and $q^2 = 0$, this reduces to $\frac{1}{2p\cdot q}$, which, keeping terms of order $\mathcal{O}((m_b/E_b)^2)$ and of order $\mathcal{O}(\theta^2)$, becomes $\frac{1}{\theta^2+(\frac{m_b}{E_b})^2}$. It should be remembered that in the integral over the 3-body phase space there are other factors that will enter, but this behavior of the b quark propagator still will have the effect of "cutting off" the collinear singularity that plagues massless QCD [38]. This suppression of gluon radiation inside θ is the so-called "dead cone" effect. In other words, gluon emission from a b is not divergent for angles less than m_b/E_b and thus the calculation is perturbatively calculable.

With this idea in mind, one can calculate the probability for a b to radiate gluons, and the gluons themselves to radiate gluons *ad infinitum*. The formalism that makes

this possible is the method of generating functionals. One should see [39] for the details, on which many chapters are spent, but in short the method relies on a Bethe-Salpeter equation which describes *trees* whose branches are separated by angles that are the jet opening angles. One begins with the imposition of strong angular ordering, in which each quark or gluon splitting must make an angle much smaller than the one in the previous splitting, and, additionally, the emitted gluon must have a much smaller energy than the parton from which it split. The result of this is that one is able to sum up all terms of order $\frac{\alpha_s^n}{\pi}\ln^{2n}\frac{Q^2}{\Lambda^2}$, with n an integer, which are of order ≈ 1 (see equation 2.4) that arise at every splitting where the emitted gluon is both soft and collinear. This is the double logarithmic approximation (DLA) to resummation. A valuable reference on resummation may be found in [40]. An instructive use of DLA without the rather complicated formalism of generating functionals can be found in reference [41] where the probability is calculated that a quark is deflected by an angle less than a given θ from its original direction. The result is the derivation of the often-used Sudakov form factor. One of the useful things that may be shown with the DLA generating functional is the phenomenon of KNO scaling [39]: the multiplicity distribution at energy $y = \ln Q/\Lambda$, $P_n(y)$, looks like

$$P_n(y) = g(\frac{n}{\overline{n}(y)})\overline{n}(y).$$

This says if one is given g (which is calculable in the $y \to \infty$ limit) at one value of Q then goes to a new $Q = Q'$ (at a new collider) and measures merely the mean multiplicity there, that the entire multiplicity distribution $P_n(y')$ is determined.

Since we have argued that in heavy quark gluon emission collinear emission does not exist (the "dead cone"), it is necessary to go to the modified or next-to leading logarithmic approximation (MLLA or NLLA). It is shown in [39] that one can get the appropriate generating functional for the MLLA by replacing *strong* angular ordering with *strict* angular ordering, *i.e.* requiring that each splitting make an angle that is merely *less* than the previous splitting angle, and not necessarily *much* less. One of the useful things that may be shown in the MLLA approximation is the feature of the scaling of the "humped back plateau." Namely, $\ln x_p$ goes linearly with Q, where x_p is the maximum scaled particle energy out of all the particles in a jet. Data collected at e^+e^- machines [39] bear this out spectacularly.

Relevant to this analysis, the MLLA provides a mechanism to calculate $D_b^h(x, Q^2)$.

In fact, in references [42] and [43] the authors re-sum contributions to one order higher than MLLA in the large logarithms – known as, yes, Next-to-Next-to-Leading order (NNLO). It should be borne in mind that this is done with Local Parton Hadron Duality (LPHD) in mind. That is, the pQCD calculation is done under the assumption that the b radiates gluons, and so on, and the b that emerges is in fact the B hadron. In [44] hadronization is put in with an *ad hoc* smearing. The calculation is done in Mellin-transformed space, meaning that what's calculated are the D_b^Ns in

$$D_b^N(Q^2) =< x^{N-1} >= \int_0^1 dx x^{N-1} D_b(x, Q^2),$$

and the $D_b^h(x, Q^2)$ are recovered with an inverse-Mellin transformation. Figure 2.9 shows the result for a particular value of the parameters Λ, the usual QCD energy scale, and μ, which arises as a result of doing pQCD to finite order. We note that the sharp peak at large x results if one does not convolve with a non-pQCD factor. This factor is chosen by Nason in [44] to be of the form $D_{np} \propto (1-x)^\alpha x^\beta$, with α, β picked to reproduce the data. See figure 5.9 for the values used here for these parameters.

2.4.2 pQCD with *"Hadronization" built in*

We see from the appearance of the dashed peak in figure 2.9, which is unobserved in the data, that pQCD rather fails. One requires the use of *ad hoc* non-perturbative smearing to fix this. A possible alternative to the Mele-Nason-Colangelo procedure described above is one where, instead of resumming to all orders in the leading terms and just pretending that the b itself *is* the final state, one does the calculation to lowest order in α_s, but considers the actual final states. This is described in this subsection.

In reference [45] the probability is calculated for a $\overline{b}$ to fragment into a B_c and a c according to figure 2.10. Account is taken of the final state with the insertion of factors into the the decay amplitude $\mathcal{M} \propto R(0)$, where $R(0)$ is the nonrelativistic radial wave function at the origin for the B_c. Also, one distinguishes between the production of B_c mesons and B_c^* mesons in the following way: γ^5s appear in the pseudoscalar amplitude $\mathcal{M}_{B_c}$, but become γ^μs in the vector meson amplitude $\mathcal{M}_{B_c^*}$. The γ^μs will get contracted (after much moving of γ^0s from spinors through γ^μs) with ϵ_μs, where ϵ_μ is the B_c^* polarization vector which will be summed over. In this way, one may say hadronization is incorporated.

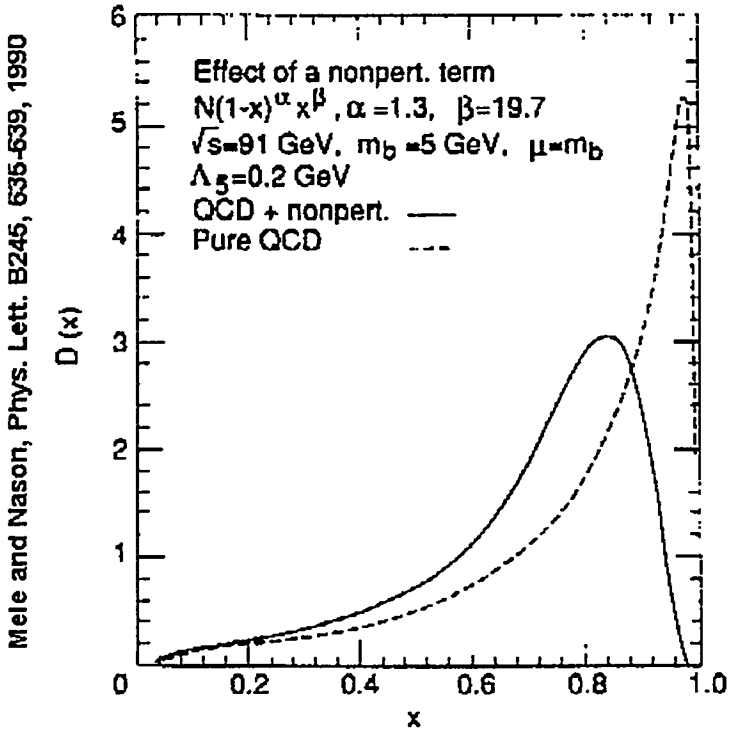

Figure 2.9: Pure pQCD calculation of the fragmentation function accurate to NNLO (dashed curve) and calculation with *ad-hoc* non-perturbative convolution (solid curve).

We know that $c\bar{c}$ production from the QCD vacuum (as depicted in figure 2.10) is rare, happening only about once for every 10^{11} light $q\bar{q}$ pair productions [46], an estimation verified recently in [47] – and is certainly out of reach of analysis at SLD. However, inspired by the agreement of their results with those predicted by heavy-quark effective theory, the authors of reference [48] propose to extend the use of this model to ordinary heavy-light meson production from its original use in heavy-heavy production (B_c production). In this thesis we will use explore this model. The expressions for pseudoscalar and vector production from bs are unwieldy and may be found in [45]. However, it is true that there are two terms – one describing vector production, and one describing pseudoscalar production. The overall normalization is fixed by demanding that the area under the curve is 1. The only free parameter to be fitted, r, is expected to be $\approx m_q/(m_q + m_Q)$, with $m_q(m_Q)$ the light(heavy)

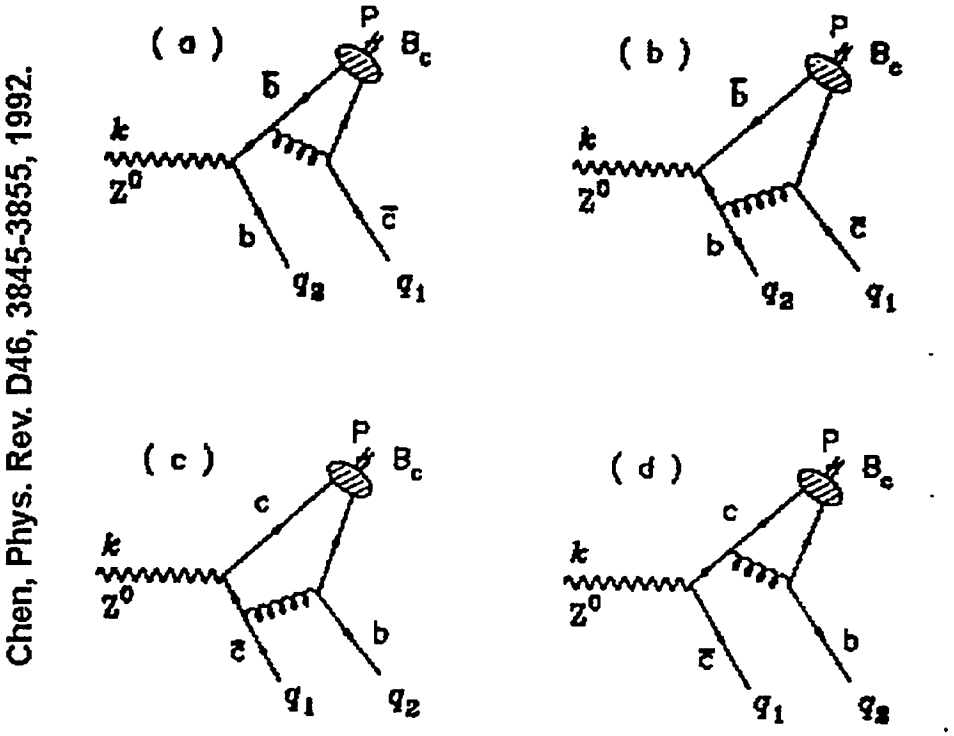

Figure 2.10: Braaten/Cheung/Yiu fragmentation model. Shown are the leading order-in-α_S diagrams to produce a heavy-heavy meson, here a B_c. This model is proposed to be used also in the production of light-heavy mesons – the type commonly created in e^+e^- annihilation.

quark mass. The functions are also functions of z, the longitudinal momentum of the B relative to the fragmenting quark. In the lab we measure the distribution in x, the energy of the B hadron with respect to the b's incident energy. The relationship of x to z is untangled with the aid of MC models[7] (z is a variable that arises naturally in $(1+1)$-dimensional models and in $(3+1)$ dimensions in so-called light-cone or Sudakov coordinates, where one considers soft and small angle emission of gluons.)

[7] We will use here JETSET7.4 [49], which is a particle physics modeling program that incorporates a "string" hadronization model to be described in this chapter.

2.5 The Models of $D_b^h(x, Q^2)$

So far we have dealt with predictions that have been inspired by QCD. However, there has been good success with models whose connection with the physics is seemingly tenuous. Two of those models are the Peterson Parametrization and the Lund string model.

2.5.1 Lund Parametrization

The development here follows closely the excellent review in reference [46]. In this subsection principles behind the calculation are only outlined; the details of the derivation are left to reference [50]. The Lund String model of hadronization results from an intuitive picture. A massless $q\overline{q}$ pair is initially created (as we have at e^+e^- annihilation) and begins to separate. The color flux lines remain constrained in a tube between them, and inside this tube new $q\overline{q}$ pairs are created. The original system thus breaks into smaller and smaller pieces until only hadrons of mass $m_\perp$ remain, where $m_\perp^2 = E^2 - p_\parallel^2 = m^2 + p_\perp^2$, which is recognizable as the mass-Energy relation in $(1+1)$ dimensions. The program is carried out in $(1+1)$ dimensional space-time, and in the end what is determined is the probability, $f(z)$ for a quark to fragment into a hadron carrying a fraction z of the original quark's longitudinal momentum. The transverse gaussian momentum distribution arises naturally on consideration of the tunneling of one quark out of its classically allowed region in the linearly confining potential $V = \kappa|x_q - x_{\overline{q}}|$, with κ the so-called string tension. Only the z distribution is considered in detail in this subsection.

Writing down the equations of motion for two massless particles $q_0\overline{q}_0$ in a linearly confining potential in $(1+1)$ dimensions, it is easily shown that in the CM frame the two particles are in a so-called "yo-yo mode," as in figure 2.11. In a boosted Lorenz frame the squares tilt and become rectangles. Now, if we allow $q_1\overline{q}_1$ production, with the particles under the influence of the usual linear potential and initially at rest, and disallow the "yo-yoing" of the original $q_0\overline{q}_0$, by giving them large initial energy, $p_{z_0} \gg \kappa = \Lambda_{QCD}$, then we can pair up $q_1\overline{q}_0$. If this pair production takes place at the right coordinate (x_1, t_1) such that $q_1\overline{q}_0$ has its mass, given by the usual mass-energy relation,

$$E^2 - p^2 = \kappa^2(x_1 - x_0)^2 - \kappa^2(t_1 - t_0)^2 = m^2, \tag{2.16}$$

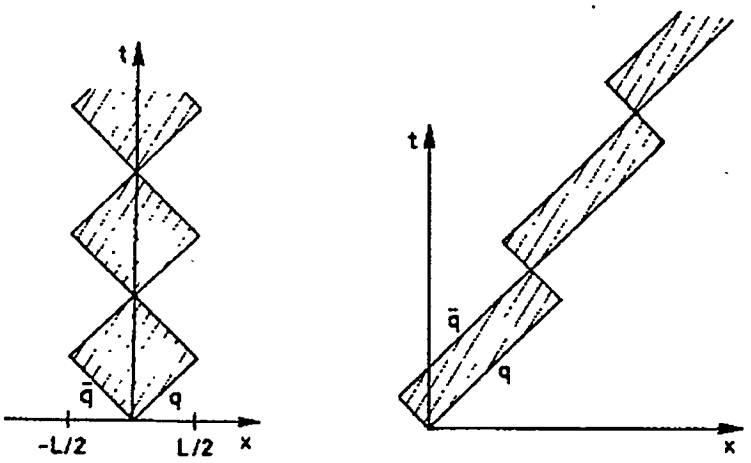

Figure 2.11: $q\overline{q}$ motion in the String model: the yo-yo mode in the center of mass and boosted frames, respectively.

equal to a known meson mass, say $m_{\pi+}$ then we call $q_1\overline{q}_0$ a π^+. Meanwhile, pair production continues, subject to the usual rules. And if our meson $q_1\overline{q}_0$ has an unrecognizable m_H, then it splits and the q_1 will find an antiquark and the $\overline{q}_0$ will find a quark and so on, until on-mass-shell mesons are all that are left. See figure 2.12. Color lines of force are thus respected, though SU(3) color singlets are not generally formed.

Imposing the condition that the production of hadrons must be symmetric from the point of view of the q and q_0 leads to [50] the desired probability, $f(z)$ for a quark to fragment into a hadron carrying a fraction z of the original quark's longitudinal momentum

$$f(z) = N\frac{1}{z}z^{a_\alpha}(\frac{1-z}{z})^{a_\beta}\exp(-bm_\perp^2/z). \tag{2.17}$$

This is the Lund symmetric scheme used by default in JETSET for fragmenting all light flavors. For simplicity, the phenomenological parameter a_α is taken equal to parameter a_β. A consideration of heavy flavors modifies this expression slightly to what's known as the Bowler model [51], though good fits can be obtained for heavy quarks using the Lund model with different $a_{\alpha,\beta}$s for different flavors.

So far we have spoken only of mesons. Baryons are formed with the allowance of

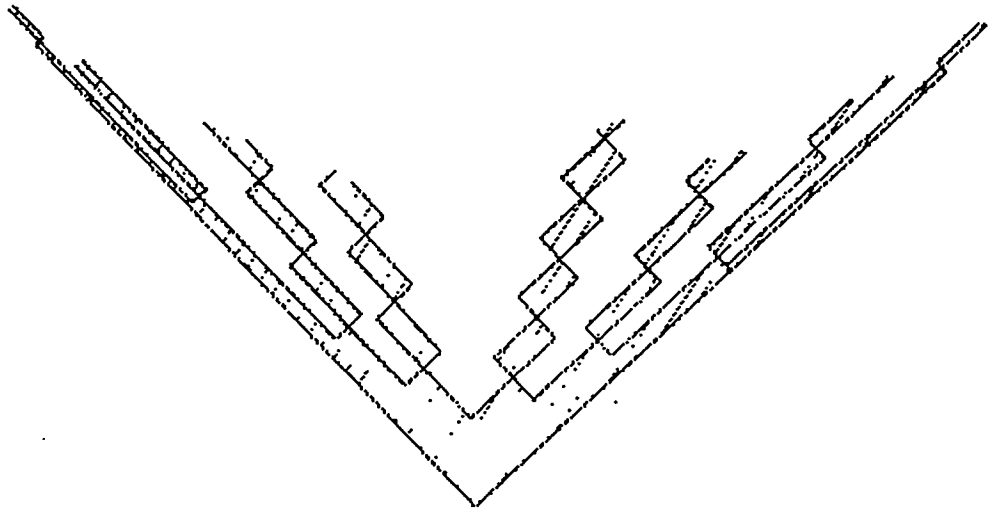

Figure 2.12: String model fragmentation showing production of $q\overline{q}$ pairs. Shaded areas are regions of non-zero color force.

diquark-antidiquark production and the subsequent formation of the invariant mass, as before. Quark flavors are produced in proportion to $e^{-\pi m_f^2/\kappa}$, with m_f the mass of the quark of flavor f. This also follows from the tunneling argument referred to earlier in this subsection, and it means quarks are produced in amounts given by

$$u : d : s : c : b \approx 1 : 1 : \frac{1}{3} : 10^{-11} : 10^{-30}. \tag{2.18}$$

2.5.2 Peterson Parametrization

The derivation of the Peterson parametrization proceeds as follows [52]. The illustration is found in figure 2.13. In the figure Q is the heavy quark – the b in our case. From first order, ordinary quantum mechanical perturbation theory the amplitude for the transition goes like

$$Amplitude \propto \frac{1}{\Delta E}$$

with

$$\Delta E = (m_Q^2 + z^2\vec{P}^2)^{1/2} + (m_q^2 + (1-z)^2\vec{P}^2)^{1/2} - (m_Q^2 + \vec{P}^2)^{1/2}$$

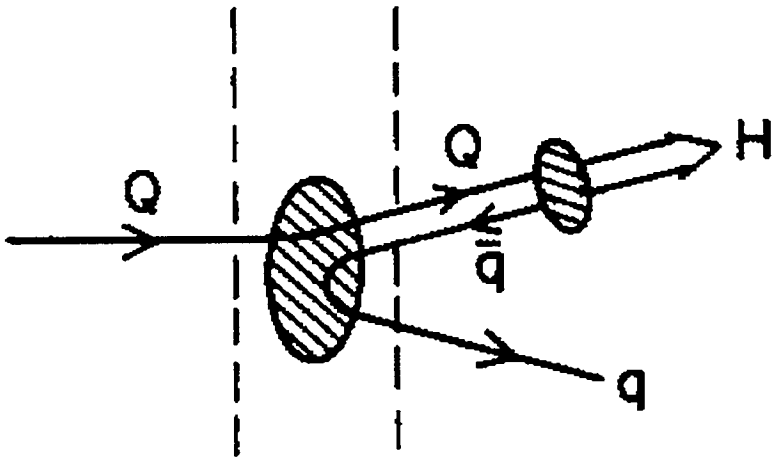

Figure 2.13: Peterson fragmentation.

$$z = \frac{(E+p_{\|})_{hadron}}{(E+p)_{quark}}.$$

The transverse contributions to the H and q momentum will be generated, as explained in the Lund Paremtrization subsection above, from a distribution that arises from a tunneling probability argument.

Since we work in (1+1) dimensions, our masses here are really $m_{\perp} = m^2 + p_{\perp}^2$. We take the hadron ($H$) mass to be $m_H \approx m_Q$, and $|\vec{P}|$ the momentum of the initial Q to be large compared to both m_Q and m_q. Expanding the three terms in $(m_Q/z|\vec{P}|)^2$, $(m_q/(1-z)|\vec{P}|)^2$ and $(m_Q/|\vec{P}|)^2$, respectively, which is consistent with the assertions in the last sentence, one arrives at

$$\Delta E \propto 1 - \frac{1}{z} - \frac{m_q^2/m_Q^2}{1-z}. \tag{2.19}$$

Throw in a $\frac{1}{z}$ for (one-dimensional) phase space, and the result is the Peterson parametrization [52]

$$f(z) = \frac{N}{z[1 - \frac{1}{z} - \frac{m_q^2/m_Q^2}{1-z}]^2}. \tag{2.20}$$

The N is for overall normalization, and in practice $\frac{m_q^2}{m_Q^2}$ is replaced by ϵ_Q, a tunable MC parameter which need only be approximately the ratio of the squares of the masses[8]. It is surprising that this simple model works as well as it does, given the potential severity of the approximations made.

2.6 B *Production and Decay*

2.6.1 *Production*

The process of quark production in e^+e^- annihilation is clear. It is governed by the electroweak processes mentioned in chapter 1. However, the next question 'Once we have the quarks how do we actually end up with a B hadron?' is far from known. The models described above should be considered to be physically motivated, but necessarily incomplete. As opposed to some model of the type sketched in section 2.1.1, here we will discuss hadronization along more general lines, specifically as it relates to B production.

In an environment such as the one at an e^+e^- machine where the number of quarks is small one can not really speak of phase transitions, as a thermodynamic ensemble of particles is necessary for this language to have meaning. Nevertheless, it is true that initially (before the quarks are separated by more than 1 fm) the quarks and radiated gluons behave as if they are in an unconfined phase, and beyond this length scale they are in a confining phase. Instead of speaking of the formation of quark-antiquark condensates, as one would at a collider like the Relativistic Heavy Ion Collider (RHIC) [53] where one does have a thermodynamic ensemble and actual chiral symmetry breaking may take place, one envisions a string (linear potential) between two quarks which breaks as the quarks try to separate by more than 1 fm when it becomes energetically more favorable to create $q\bar{q}$ pairs. (See section 2.5.1 above.) It's also true that quark and gluon production may arise earlier, perturbatively, with the radiation of gluons and their subsequent splitting into $q\bar{q}$ pairs. It is important to this analysis that the production of bs is not significant in either of these mechanisms. From phase space arguments [46] and from LEP results [47, 54] one expects $b\bar{b}$ pairs to be produced at the level of only $\approx 10^{-30}$ compared to $u\bar{u}$, $d\bar{d}$ production. Now the quarks and gluons must combine into color singlets, as argued

[8] $\epsilon_b = 0.006$, $\epsilon_c = 0.06$ are the default parameters in the official SLD MC.

above. In particular, this implies that the outgoing q and $\overline{q}$, each of which is colored, must exchange gluons (at least two, by group theory) with each other. One result is that jets are necessarily blurred together, especially if they're not very energetic (compared to $\Lambda_{QCD} \approx 200$ MeV). However, we argue that due to the scale at which non-pQCD sets in, this blurring is small due to the fact that the q and $\overline{q}$ set out from the interaction point with 45.6 GeV which is much bigger than Λ_{QCD}. Such an argument is effectively the principle behind LPHD, explained earlier.

The main point of this section must be that however hadronization works, the mechanism is unknown in detail. In this analysis we make no attempt to shed light on this mechanism – only to study the resulting energy spectrum of the B hadron, the probability with which a quark starting with 45.6 GeV will wind up in a hadron carrying some fraction x of this initial energy. The picture is shown in figure 4.1. The details of the analysis are deferred to chapter 5 where an explanation of the labels in the figure can be found. The event selection procedure may be found in chapter 4.

2.6.2 B *Decay*

In chapter 4 we discuss the means by which one may tag B hadrons. Here we will try to describe the dynamics of B decay. Particular emphasis will be placed here on semileptonic decay which is most important in our analysis.

Hadrons containing b quarks decay weakly, by the rules of $\mathcal{L}_{Weak_b}$ as outlined in chapter 1. In particular $b \rightarrow cW^-$, with an immediate decay $W^- \rightarrow l^-\overline{\nu}_l$,$\overline{u}d$,$\overline{c}s$ since the W^- is very far off-shell. The last of these options for the W^- is unlikely, by phase space, as mentioned above. The second leads to hadronic B decays, and are ignored as this is a study of s.l. B hadrons. $b \rightarrow uW^-$, where the W^- decays as listed above, is possible too but is suppressed by the ratios of the relevant Cabibbo-Kobayashi-Maskawa matrix elements, $|\frac{V_{ub}}{V_{cb}}|^2 \approx 0.01$ [55].

We focus on $b \rightarrow cl^-\nu_l$ in the rest of this section. The $W^{\pm}$s couple only to the left-handed Weyl fermions from equation 1.1, and thus the interaction is of the $V-A$ form,

$$\mathcal{L}_{Wbc} = g[\overline{c}\gamma^\mu(1-\gamma^5)bW^+_\mu + \overline{b}\gamma^\mu(1-\gamma^5)cW^-_\mu]$$

This looks much like[9] equation 1.2 with $g_v = g_a = g$. In analogy to $\mu \rightarrow e\overline{\nu}_e\nu_\mu$, one

[9] where here we need two terms here to make the lagrangian hermitian

can write down immediately the decay width in the limit that the light quark in the B just sits idly by (the *spectator* approximation):

$$\Gamma(b \to c l^- \nu_l) = \frac{G_F^2}{192\pi^3}|V_{cb}|^2 m_b^5 g'(m_c/m_b) \tag{2.21}$$

where $g'(m_c/m_b)$ fixes the assumption that the c is massless. This assumption is made here to make use of the analogous calculation for $\Gamma(\mu \to \nu_\mu e^- \bar{\nu}_e)$, where to a very good approximation $m_e = 0$. $g'(m_c/m_b)$ incorporates QCD corrections too.

A calculation of the energy spectra $\frac{d\Gamma}{dE_l}$ of the l is more involved [56]. One begins again with the analogous expression from μ decay, but has to consider non-perturbative QCD corrections to the spectator model or appeal to Heavy quark effective theory (HQET), which has been of some help in this area [57]. Figure 3.26 demonstrates the success of the Isgur-Wise HQET in semileptonic B decay.

A quantity defined as a_{fb} (not to be confused with the forward-backward b production asymmetry, A_{FB}, measured at SLD or LEP) given by

$$a_{fb} = \frac{d\Gamma(\theta) - d\Gamma(\pi - \theta)}{d\Gamma(\theta) + d\Gamma(\pi - \theta)},$$

where $0 < \theta < \pi/2$ is the angle between the l and ν in the l-ν rest frame, gives convincing evidence that the $V - A$ form of $b \to c$ is the right one [58]. In the Standard Model $a_{fb} = 0.13 - 0.15$. At CLEO II for leptons with $p_l > 1$ GeV $a_{fb} = 0.14 \pm 0.06 \pm 0.03$.

2.7 Practical Matters: Event Shape Variables

A variety of variables exist that characterize the underlying partonic nature of real physics events. These include spherocity, oblateness, energy-energy correlation (EEC), etc. A good reference is [59], where it is made clear that infrared and collinear safe quantities are desired – quantities which do not change abruptly if one adds a soft particle to the final state or splits one particle in the final state into two particles sharing proportionately its momentum. Sphericity and event multiplicity fail these criteria, for example. Those that do pass the criteria may be calculated in perturbative QCD, allowing for an extraction of α_S [60]. Here we want only to consider thrust

$$t = \max \frac{\sum_a |\vec{p}_a \cdot \vec{n}_{thrust}|}{\sum_a |\vec{p}_a|}, \tag{2.22}$$

where the sum runs over all final state particles. We care about thrust only for the purpose of dividing our event into hemispheres, not for the extraction of α_S. t takes the values $1 \geq t \geq \frac{1}{2}$, with events in which $t \approx 1$ being "back-to-back" or 2-jet like. Note that $\vec{n}_{thrust}$ or $\vec{t}$ provides an axis which divides the event into hemispheres, but whose sense[10] is arbitrary.

While thrust is of interest in all hadronic events ($Z \rightarrow q\overline{q}$), to find the original $q\overline{q}$ axis in events where a hard gluon is radiated from the initial q or $\overline{q}$ or where there is even higher order emission, we would like to find "jets." Jet-finding is an attempt to produce the underlying parton directions. Here one ignores the believed-to-be low momentum partonic exchanges required for color singlet formation, and pretends that outgoing particles can be clumped together in a reasonable way to reproduce the underlying 4-momenta of the responsible parton. Various jet algorithms proceed in the same ways [61], but differ in how the grouping of clusters or tracks is done.

Here we describe the JADE algorithm. In this prescription one forms from all possible combinations of two tracks (or clusters, as in this and most analyses) their scaled invariant mass, $\hat{s}_k = \frac{2E_iE_j(1-\cos\theta_{ij})}{s_{ij}}$. The pairs with the smallest values of y_{ij} are combined, and one calls the new combinations "pseudo-particles." One assigns the pseudo-particles the 4-momenta $p_k^\mu = p_i^\mu + p_j^\mu$, and repeats the process. The clumping together continues until all clumps have invariant mass $\hat{s}$ greater than a pre-chosen y_c. In the end, one is left with a list of N jets with momenta $\vec{p}_i$. The choice of y_c depends on one's application. For doing B physics we choose $y_c = 0.005$ to give the best reproduction of the underlying b direction [62]. Four jets is the most common number at this y_c. The high four-jet rate actually aids in finding the B direction, even though such a high rate of four-jets does not reflect well the underlying parton activity.

[10] $\vec{t} = (\theta, \phi)$ is not to be distinguished from $\vec{t} = (\pi - \theta, \pi + \phi)$.

Chapter 3

SLC AND SLD

3.1 The Experimental Apparatus

The data analyzed here were taken during the 1993 and 1994/95 runs at the SLD – the detector sitting at the only interaction point (IP) of the Stanford Linear Collider (SLC [63]) at the Stanford Linear Accelerator Center (SLAC). At the IP 45.6 GeV e^+s annihilate with 45.6 GeV e^-s. These energies are chosen in order that the center of mass energy is at the Z^0 resonance.

The SLD is a full-coverage particle detector, built to take advantage of the SLC's novel features: stable and small beams at the IP, with the e^- beam polarized to a high-degree along or anti-along the beam axis[1].

The SLD collaboration consists of approximately 150 active physicists from 34 institutions. The names and institutions of the collaborators on SLD can be found in Appendix A.

A description of the SLC and the hardware that was used to collect the data is described in this chapter.

3.2 The Linear Collider

The SLC at SLAC consists mainly of a two mile long accelerator and a set of arcs that meet at one interaction point. The SLC runs below the klystron gallery – a two mile long building containing the necessary power supplies, and RF equipment. It is the first-ever linear collider [64]. A schematic illustration is seen in figure 3.1. Since the beams are not continuously circulating and colliding, as in the case of traditional e^+e^- machines, a whole new set of challenges had to be understood and overcome at the SLC. The performance parameters are seen in table 3.1. Numbers in this table

[1] Whether the e^- beam is polarized along or anti-along the beam direction depends on whether the polarization of the laser, which causes the photo-emission of the e^-s, is set to be circular-right-handed or left-handed.

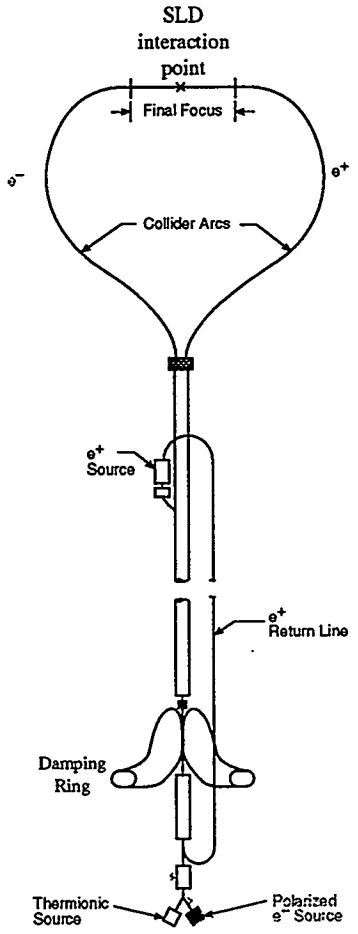

Figure 3.1: The Stanford Linear Collider

make reference to equation 3.1 on page 42 – the expression for the luminosity at an e^+e^- machine. The data used in this analysis is from the 1993 run, during which the average electron beam polarization was 63% and from the 1994/1995 run, during which the average electron beam polarization was 78%. The time history of the beam polarization and luminosity over the course of the two runs may be found in figure 3.3 and figure 3.2, respectively. This second plot shows that in 1993 roughly 50,000 Z^0s were produced, and in 1994/1995 roughly 100,000 Z^0s were produced.

A description of the creation and transport of the polarized electron beam from the e^- gun to the IP follows.

Table 3.1: See equation 3.1 for the meaning of the parameters of the 1993 and 1994/95 runs, shown here.

	1993	1994-95
σ_x	2.6 μm	2.5 μm
σ_y	0.8 μm	0.6 μm
$n_{e^\pm}$	2.9 $\times 10^{10}$	3.5 $\times 10^{10}$
f_c	120 Hz	120 Hz
Π_d	70%	65%
η	1.05	1.20

3.2.1 The Polarized Electron Source

When GaAs absorbs circularly polarized light of an energy just larger than that of the band gap in the GaAs, polarized electrons are emitted [65].

The photo-emitted electrons are accumulated into a bunch with a 178 MHz RF field. The bunch is then accelerated to 50 MeV, and enters the straight, linear portion of the accelerator (the LINAC). The e^- bunch remains in the LINAC only until it reaches the entry point to its damping ring, at which time the electrons have an energy of 1.19 GeV. Two such bunches are created with each 120 Hz machine cycle. One bunch eventually reaches the IP, while the other is used to create the positrons which collide at the IP with the electron bunch.

3.2.2 Damping Rings

The purpose of the damping rings is to shrink the phase space volume that the e^-s and e^+s occupy. A small spread in momentum and physical space allows for smaller backgrounds in the detector and fewer losses during acceleration. The beams are thus stored at 1.19 GeV in the rings. The positrons, which have a larger energy spread when they come from their source, are damped for two machine cycles ($\approx$ 16.6 ms), in contrast to the electrons which are damped for just one cycle ($\approx$ 8.3 ms).

In order to preserve the e^- polarization in the Damping Rings it is necessary to have the e^- spin direction pointing out of the plane of the damping rings. This is because the precession frequency of the spin vector goes like $\vec{\mu} \times \vec{B}$, with $\vec{\mu}$ the electron's magnetic moment and $\vec{B}$ the damping ring's magnetic field – which of

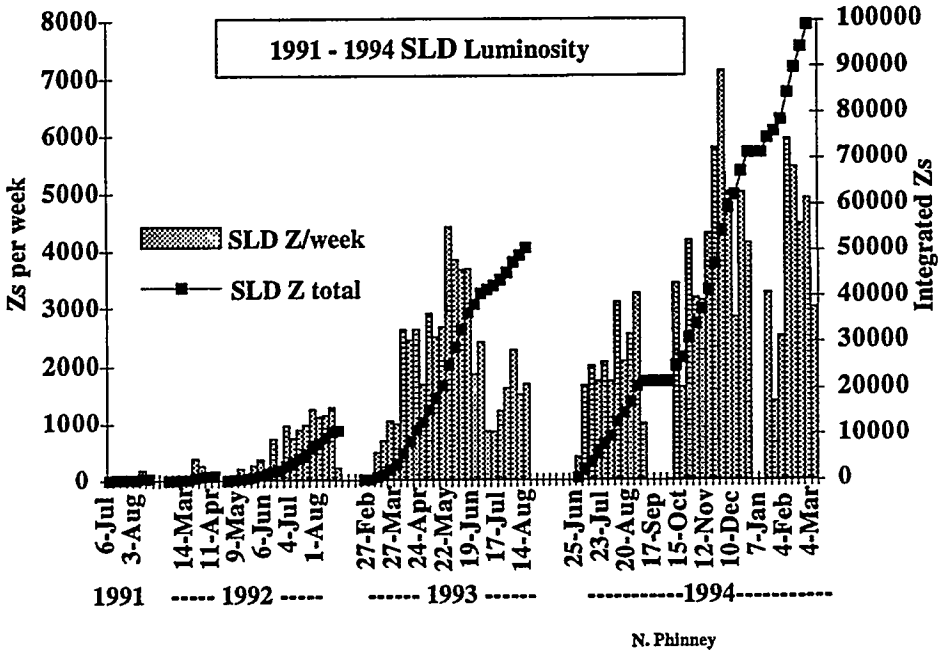

Figure 3.2: The 1993-1995 Z^0s per hour and integrated Luminosity

course is perpendicular to the plane of the ring in order to keep the e^-s orbiting within them. This is achieved by passing the e^-s through a solenoidal field just as they enter the ring. In the 1993 and 1994/1995 runs flat beams were used ($\varepsilon_x \sim 10\varepsilon_y$), which prohibited the use of the ring-to-LINAC solenoid to return the spins to longitudinal at the exit of the damping ring. This is because the emittances[2] become coupled. Therefore the electrons are accelerated with their spins pointing up through the LINAC, and their spins are brought to longitudinal through a series of "spin bumps" in the arcs (Section 3.2.5). Flat beams with their lower emittance in the vertical plane allowed for lower backgrounds in the SLD [66].

[2] The emittances in x and y are the position-velocity phase-spaces of the beam.

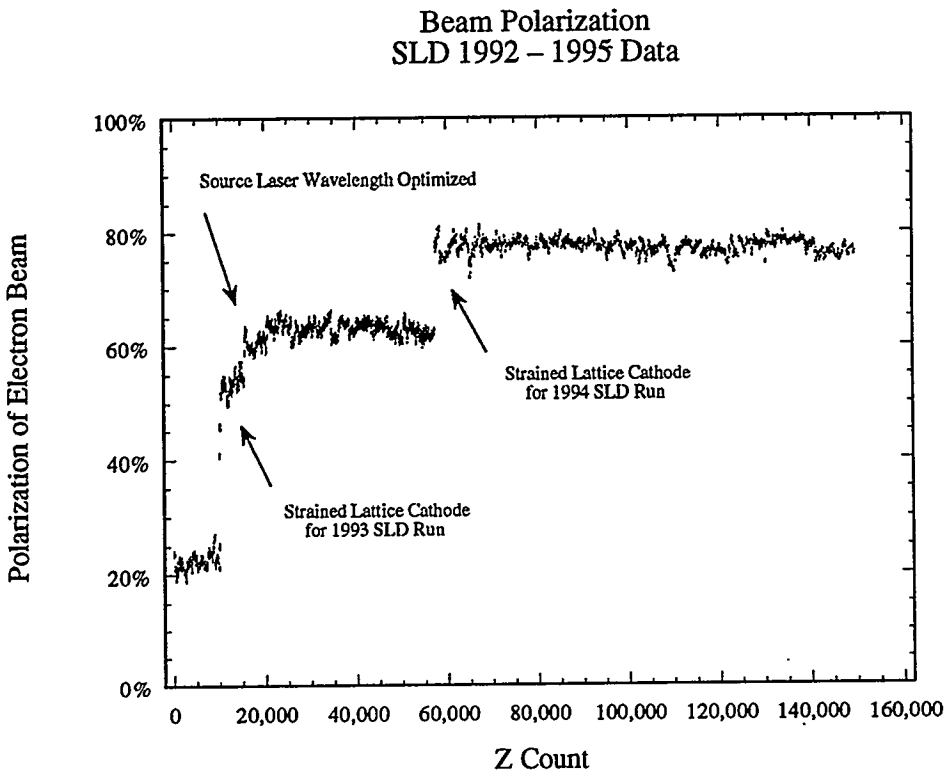

Figure 3.3: The time history of the e^- polarization from 1992 through 1995.

3.2.3 Positrons

The second bunch of electrons that is produced with each machine cycle follows the first bunch into and then out of the damping rings and down the LINAC (see next section). However, approximately two-thirds of the way down the LINAC this bunch is directed out of the LINAC and brought into collision with a tungsten target. As in any non-vacuum medium through which relativistic electrons pass, an electromagnetic shower results, brought on initially by the process of *Bremsstrahlung* and then pair-production, *i.e.* $e^- \rightarrow e^-\gamma$ followed by $\gamma \rightarrow e^-e^+$. The resulting e^-s and e^+s repeat the process, and a shower results. The positrons emerge in a large energy range, and those between 2 and 20 MeV are diverted into the return path to the front end of the LINAC where they go through the short, first section of the LINAC as did the e^- bunch that created them, and then are diverted into their own damping ring (SDR).

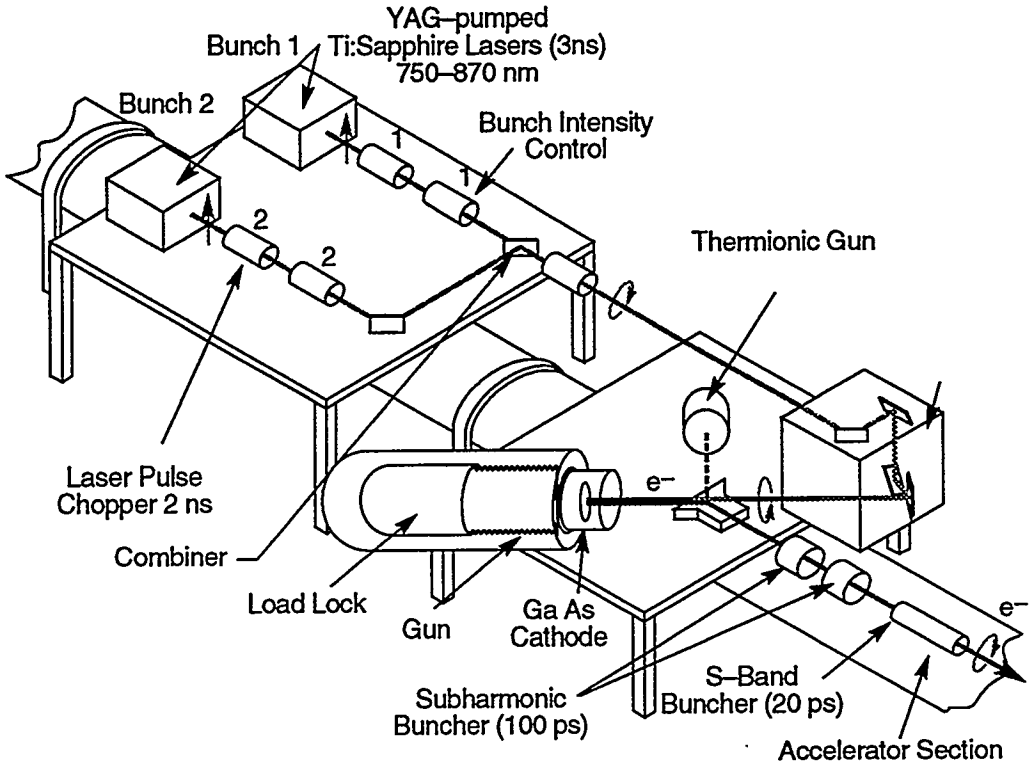

Figure 3.4: The SLC electron source.

3.2.4 The Linear Accelerator

Radio frequency cavities controlled by klystrons above ground provide an accelerating field of 17 MeV/m. The RF is timed to be in the opposite phase in order to provide the opposite sign $\vec{E}$ field for e^- bunches, as compared with e^+ bunches. The cavities span approximately 3 kilometers and form the linear accelerator. Typically $\approx 3 \times 10^{10}$ particles per bunch travel down the LINAC, and arrive at the arcs with ≈ 0.9 GeV more energy than their necessary collision energy.

3.2.5 The Arcs and The Final Focus

As the e^-s and e^+s "coast" (there are no more RF cavities to push them along, only bending and focusing magnets) along in their respective arcs for their 1km lengths, they lose energy by synchrotron radiation until their energies are each 45.6 GeV, putting their collision energy at m_{Z^0}. The arcs do not lie in the horizontal plane, but

rather a plane that follows the terrain, and so the beam transport is slightly more complicated than if it were in the horizontal plane. In flat beam mode the e^- arc is used to flip the e^- spin from pointing up (out of the plane of the damping rings/arcs) to longitudinal by the time the e^- bunch arrives at the final focus.

The purpose of the final focus (FF) is to bring the bunches down to very small sizes in order to compensate for the SLC's relatively low machine cycle and increase the luminosity in this way. This follows from

$$\mathcal{L} = \frac{n_{e+} n_{e-} f_c}{4\pi\sigma_x\sigma_y}\Pi_d\eta, \tag{3.1}$$

where n_{e+} and n_{e-} are the positron and electron mean populations per bunch, respectively, f_c is the machine cycle frequency of 120 Hz, σ_x and σ_y are the x and y beam transverse overlaps, η is the beam-focusing enhancement factor, and Π_d is the machine efficiency [67]. Typically $\mathcal{L} \approx 3 \times 10^{29}$. A direct measurement of $\mathcal{L}$ will be discussed in section 3.3.2. Thus, in the FF there are three superconducting quadrupole magnets, the first of which is 1.5 meters from the IP. At the IP beam spot the dimensions are $\approx 3\ \mu$m in the x-direction and $\approx 0.8\ \mu$m in the y-direction and ≈ 1 mm in the z-direction. The size and location of the IP is very stable over time [63].

3.2.6 Energy Measurement

After the electron bunch passes the IP, the e^- polarization is measured using a Compton polarimeter [68] in the opposite (South) arc (see section 3.3.1 below), and finally, before dumping the beams, the energy of each beam is measured in a spectrometer called the Wire Imaging Synchrotron Radiation Detector (WISRD) [69]. The WISRD works essentially by bending the beam and observing the angle of the subsequent stripe of synchrotron radiation with respect to the incident beam direction. See figure 3.5 for an illustration.

3.3 The SLD

One multi-purpose detector measures the properties of collisions at the IP [70]. The SLD, shown in figure 3.6, combines excellent tracking, calorimetry and particle identification into a state-of-the-art high energy physics detector. It is a cylindrical device

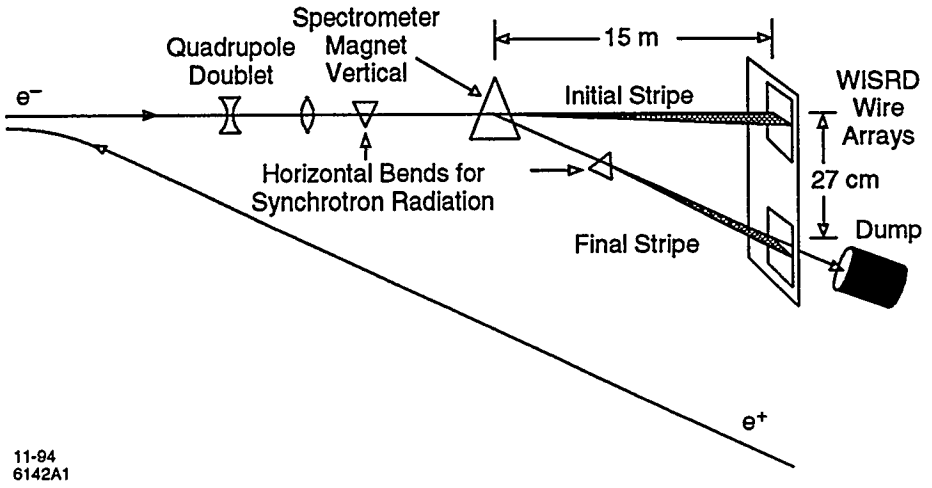

Figure 3.5: The WISRD.

with a 0.6 Tesla axial magnetic field, in which charged particles bend. The curvature of the resulting tracks reveals the particles' three-momenta. A "barrel" and two "endcaps," which may be moved during downtimes for access to the interior of the detector, surround the IP. The coordinate system used is a normal right-handed spherical polar system: the z-axis points North in the direction of the e^+ beam; ϕ, the azimuthal angle runs from 0 to 2π, with $\phi = 0$ pointing West; and the polar angle θ runs from 0 (North) to π (South).

This thesis uses the SLD Liquid Argon Calorimetry (LAC) subsystem, the Central Drift Chamber (CDC) subsystem and the Vertex Detector (VXD2). Additionally, the Warm Iron Calorimeter (WIC) is used to tag muons. A description of the various subsystems of the SLD follows, with an emphasis on the LAC. A slice of the SLD can be seen in figure 3.7.

It is worth noting that the Čerenkov Ring Imaging Detector (CRID) is not used here, nor is the Luminosity Monitor (LUM) or the Medium Angle Silicon Calorimeter (MASIC), the latter two of which in combination with the LAC and WIC comprise the whole calorimeter system (KAL). The endcap CRID (ECRD) and endcap drift chambers (EDC) are not used either, and a cut on the event thrust keeps the use of the

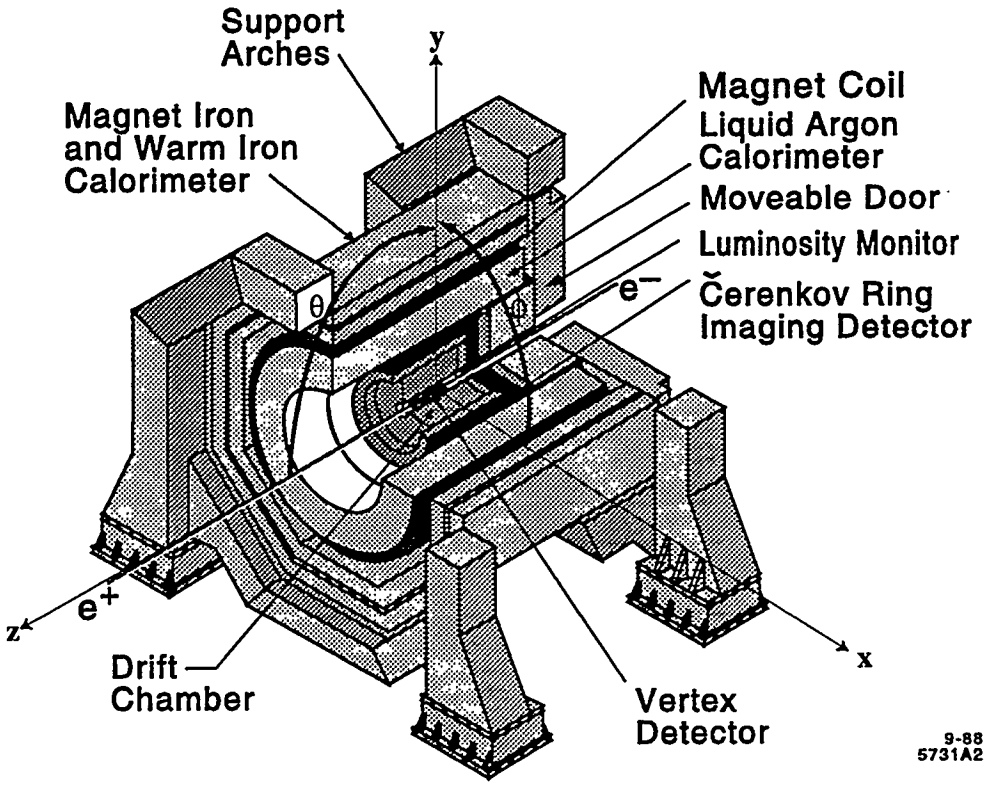

Figure 3.6: The Stanford Linear Collider Large Detector – Cut-away view.

endcap WIC and endcap LAC to a minimum. Continued problems with EDC tracking and the fact that the VXD2 polar angle coverage extends only to $|\cos\theta| < 0.71$ dictate that this event thrust cut be used in the first place. However, short of the EDC, one could in fact use the entire detector for this analysis. Since no attempt is made here to fully reconstruct various decay modes of the semileptonic B decay, the use of the CRID is unnecessary.

3.3.1 e^- Polarization Measurement

The process of Compton scattering is used to measure the electron beam polarization. A circularly polarized laser is directed onto the remnants of the e^- beam after it passes through the IP. The electrons that scatter from the laser photons are bent away from the bunch and spread according to their momenta in a dipole analyzing magnet. A 7-channel Čerenkov detector is positioned in the plane of the spread so as

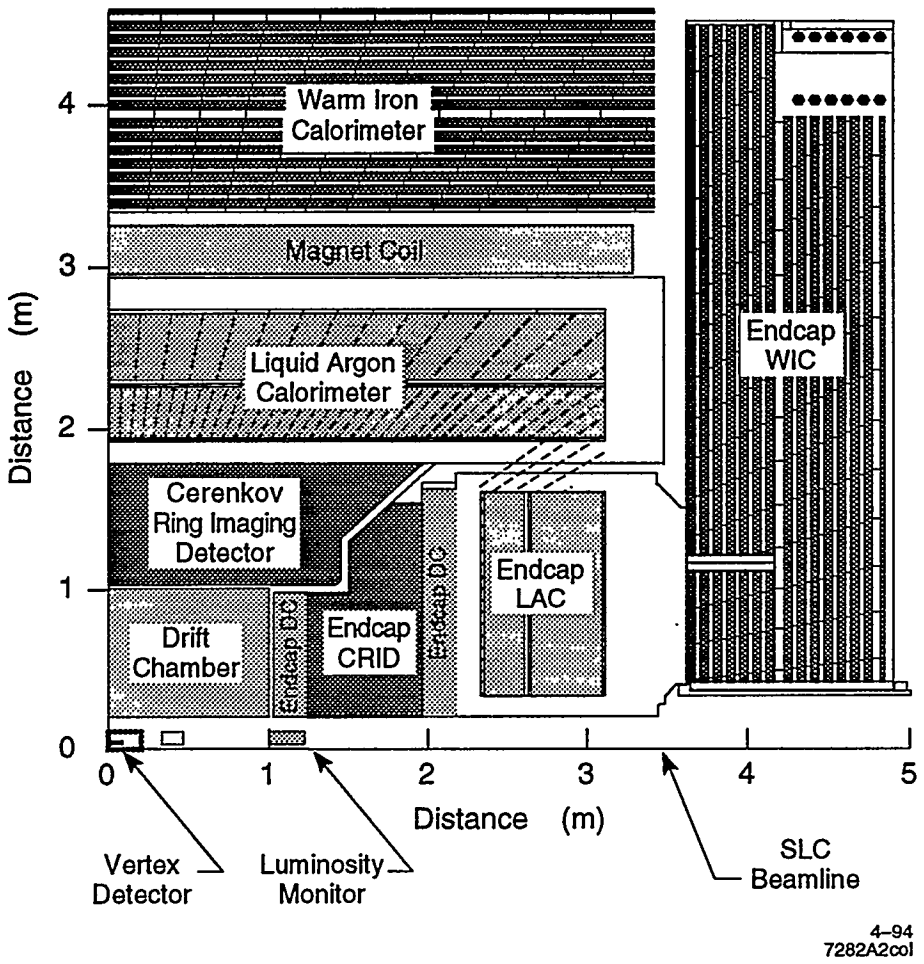

Figure 3.7: The Stanford Linear Collider Large Detector – Slice showing all major subsystems.

to measure the energy of the scattered electron by detecting it in one of its channels (see figure 3.8).

The polarization of the electrons is taken from this cross-section measurement, via

$$\frac{d\sigma}{dE} = \frac{d\sigma_0}{dE}(1 + P_\gamma P_e A_c(E))$$

with σ_0 the unpolarized Compton scattering cross-section, P_γ, P_e the known photon and unknown electron polarizations, respectively, and A_c the energy-dependent asymmetry [71]. A plot of a calculation of this last quantity compared to its measurement is seen in figure 3.9.

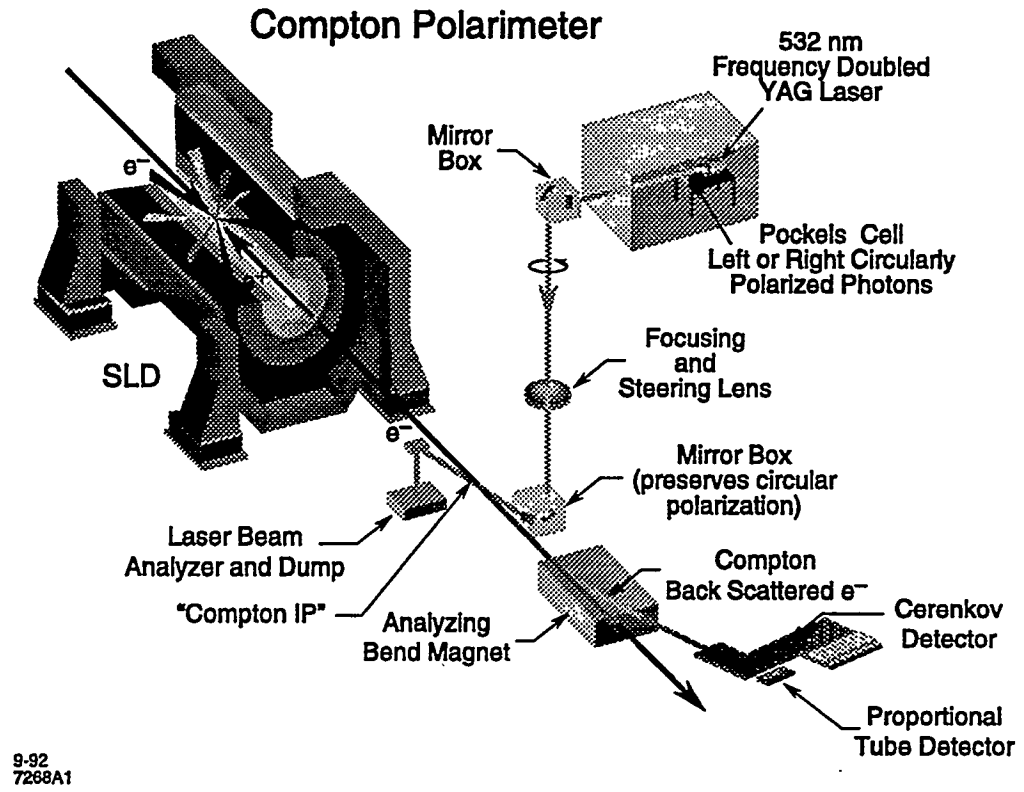

Figure 3.8: The Compton Polarimeter.

3.3.2 Luminosity Monitor

In order to accurately measure various electro-weak cross-sections, one needs to know the luminosity delivered by the SLC. One way this may be done is by seeking out a particular process whose rate is well-known and is experimentally easy to identify. Such a process is $e^+e^- \rightarrow e^+e^-$, known as Bhabha scattering. The four Feynman diagrams in figure 3.10 are the tree level contributions near $\sqrt{s} = m_{Z^0}$. Since the cross-section is the square of the sum of the amplitudes there are 10 terms that contribute from these four diagrams. Figure 3.11 shows that at small scattering angles ($\cos\theta$ above ≈ 0.85) term 3, which is the square of the diagram in the lower left of figure 3.10 constitutes essentially the entire cross-section. This is the so-called "t-channel photon exchange" diagram. The expression for this term when higher order diagrams are included allows for an extraction of the absolute luminosity.

For the reason that low angle scattering is needed, the Luminosity Monitor shown

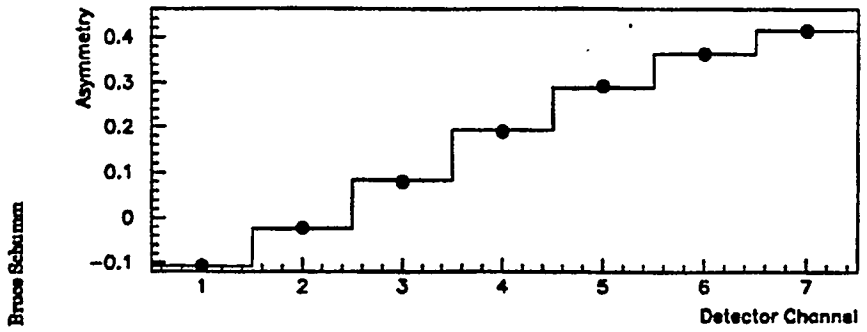

Figure 3.9: The measured energy-dependent Compton asymmetry function (see text) vs. the predicted shape.

in figure 3.12 (LUM) sits right on the Final Focus triplet assembly, spanning the polar angle between 28 and 68 mrad. The LUM consists of 23 layers of alternating silicon detectors and tungsten radiator plates, where electromagnetic showers develop. The electron/hole pairs that are created in the fully depleted silicon are collected by charge sensitive preamplifiers. The total depth of the LUM is $21X_0$, and the design energy resolution is 3% at 50 GeV [72].

3.3.3 Particle Identification

The Čerenkov Ring Imaging Device

In a medium in which a particle travels at a speed exceeding the speed of light in that medium, a cone of Čerenkov light is produced whose opening angle θ follows

$$\cos\theta = \frac{1}{\beta n},$$

where β is the speed of the particle relative to the speed of light in vacuum and n is the index of refraction in that medium. The angle θ of the cone can be inferred by reflecting the photons of Čerenkov radiation with a parabolic mirror onto a plane and measuring the radius of the resulting circle. The CRID (figure 3.13) exploits this effect. Particles traveling into the CRID Čerenkov-radiate in either the gas or the liquid, and the cones of light are reflected onto a plane inside a *time proportional chamber* which, due to the addition of a small amount of gas called

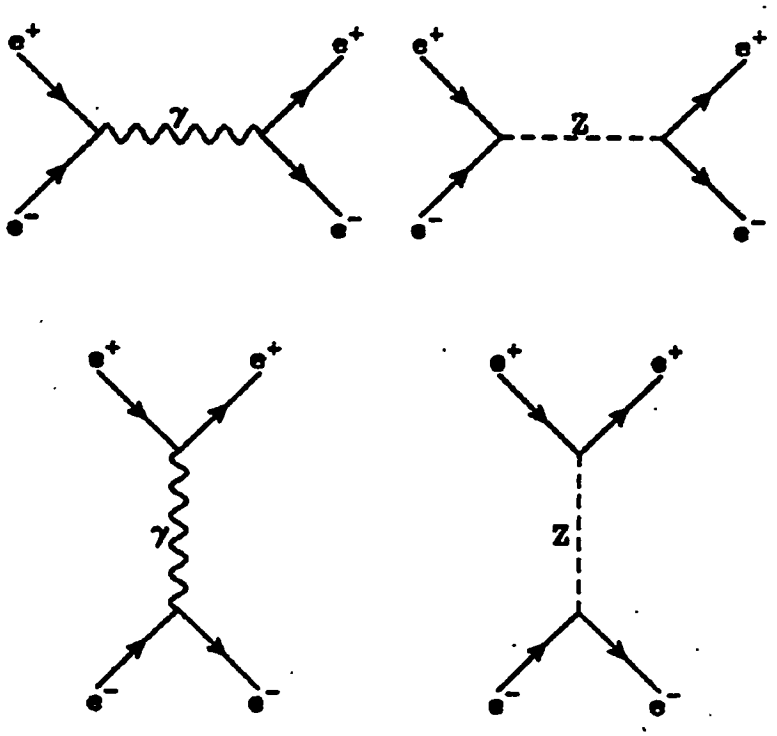

Figure 3.10: The four tree-level Feynman diagrams that contribute to $e^+e^- \rightarrow e^+e^-$ scattering near $\sqrt{s} = m_{Z^0}$.

tetrakis(dimethylamino)ethylene (TMAE), yields about one electron for each incident photon. The electrons, then, drift in the chamber to *sense wires* that receive the charge – similarly to the way things work in the SLD drift chamber. The drift time along with a knowledge of which wire at the end of the chamber collects the charge allows for a measurement of the cone opening angle θ – thus v is known, and from it, γ, the Lorenz factor – and combined with $\vec{p} = \gamma m \vec{v}$, where $\vec{p}$ is known from the particle's track in the CDC (see section 3.3.4), the mass, and thus the identity of the particle is known. A plot of the efficiency of the CRID to distinguish πs, Ks and ps is seen in figure 3.14. Note that the maximum value on the y-axes for the mis-ID plots are an order of magnitude smaller than the correct-ID plots. One also notes that the presence of both liquid and gas radiating media is necessary to cover the desired range of particle momenta.

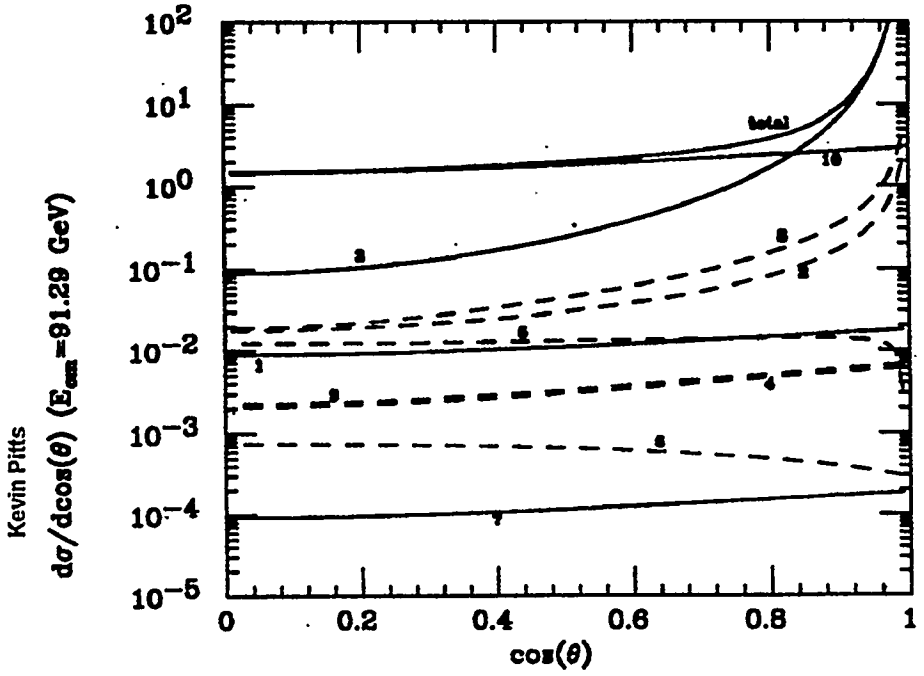

Figure 3.11: The tree-level $e^+e^- \rightarrow e^+e^-$ scattering cross-section near $\sqrt{s} = m_{Z^0}$. Shown are the contributions of the 10 terms resulting from squaring the summed amplitudes of the diagrams in figure 3.10. The curve labeled "3" – the t-channel photon exchange diagram squared – dominates at large $|\cos\theta|$. (This is the one whose value at $\cos(\theta) = 0$ is $\approx 10^{-1}$.)

3.3.4 Tracking Devices

Within the SLD there exist three main tracking devices: the Central Drift Chamber (CDC), the Vertex Detector (VXD2) and the Warm Iron Calorimeter (WIC) Strips.

Vertex Detector

The VXD2 is shown in figure 3.15. It is SLD's closest component to the IP with an inner radius of 3.0 cm, and an outer radius of 4.2 cm. It is made up of 480 *charge coupled devices* (CCDs) which surround the IP in four concentric barrels. Each CCD contains approximately 400 × 600 pixels, each of size 22 × 22 microns. A minimum ionizing particle that traverses a CCD deposits $\approx 650e^-s$ [73] in the depletion region of the Silicon in the CCD. The data from the 120 Mpixels is read out and condensed to

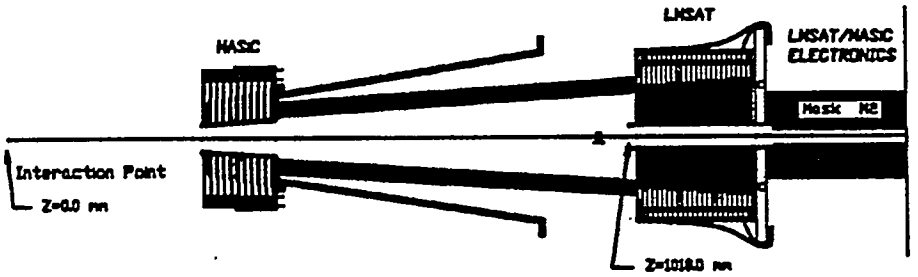

Figure 3.12: The luminosity Monitor (LUM).

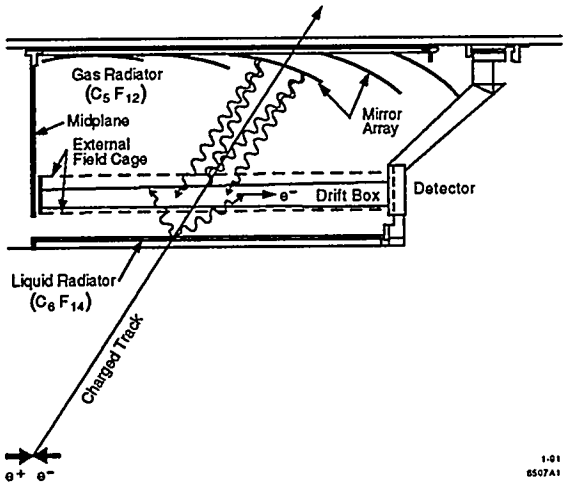

Figure 3.13: The CRID.

approximately 50-80 kbytes per event [74]. The CCD technology is allowable because of SLD's relatively low machine cycle: 90 milliseconds are required to read out the entire VXD2 compared to the ≈ 8 millisecond bunch separation time. Clearly, several beam-crossing's worth of information is collected with every read-out, but the fine granularity of the VXD2 combined with the infrequency of noise hits (≈ 5 per CCD event) make it unlikely that a VXD2 hit is put on the wrong track when it comes time to combine CDC tracks with VXD2 hits. The VXD2 has a polar angle coverage of $|\cos\theta| < 0.71$. It is perhaps worth noting that VXD3, to be installed for the 1996

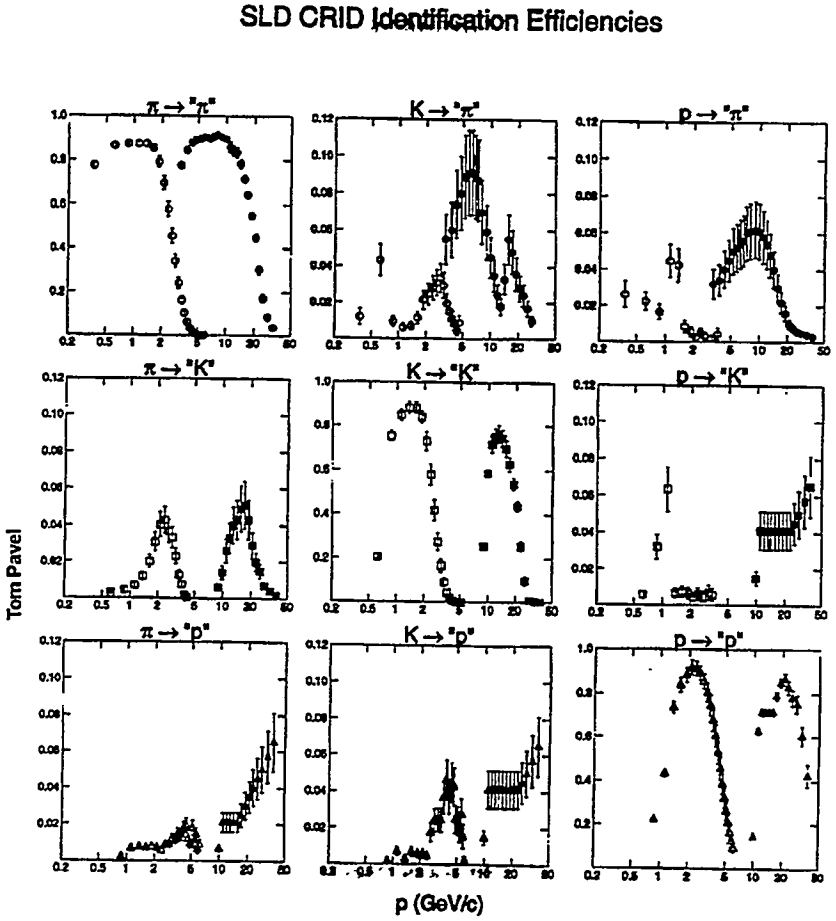

Figure 3.14: π^+, p, K^+ (and their anti-particles) Monte Carlo (mis-)identification efficiency. Note that the plots on the diagonal are the correctly ID'd particles, and the maximum value on their y-axes (1.0) is an order of magnitude larger than that on the off-diagonal plots – the *in*correctly identified particles. Also note the interruption in each plot in the two curves: in the lower (higher) momentum range the liquid (gas) radiator is used.

run and beyond, will have a polar angle coverage of $|\cos\theta| < 0.90$ [3].

The Drift Chambers

The primary task of reconstructing the tracks from charged particles that traverse the SLD falls to the Central Drift Chamber and the Endcap Drift Chambers. The CDC is a cylinder that measures roughly 1 meter in outer radius and two meters in length. Its inner radius is 20 cm, sitting just outside the Vertex Detector. Its

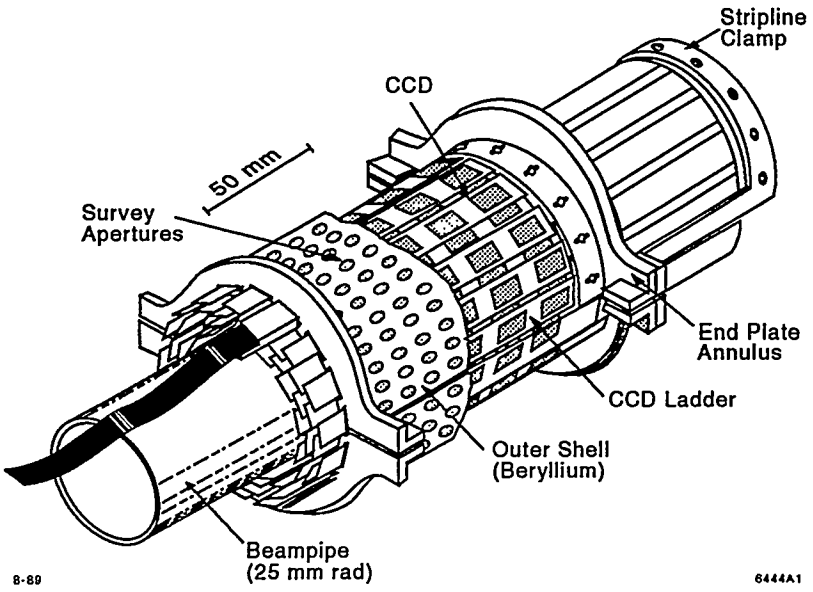

Figure 3.15: The VXD2.

gas mixture is 75% CO_2, 21% Ar, 4% isobutane and 0.3% H_2O. Relatively constant drift velocity and proportional gain are obtainable with this mixture. The CDC consists of ten cylindrical sections, called *super layers.* Moving azimuthally within one super layer one passes from cell to cell, each full of 8 sense wires. Depending on exactly which super layer one examines, the electric field-forming wires, the sense wires, and other wires run axially from one end of the CDC to the other, or at just a slight tilt with respect to the z-axis. Moving radially from super layer to super layer from the inner radius of the CDC to the outer radius one encounters wires strung first at a small tilt with respect to the z-axis, then wires strung exactly along the z-axis (axial super layer), and then wires strung at minus a small tilt. The purpose of this tilt is to determine the z coordinate of a given hit. This is called *small angle stereo* layering. The tilt in going from super layer to super layer provides better information to determine the z-coordinate of a hit than merely relying on the information from comparing the amount of charge collected at each end of a given wire (charge-division). The points at the end of the CDC where the wires attach are seen in figure 3.16.

The measurement of actual tracks begins with collecting the ionization from the

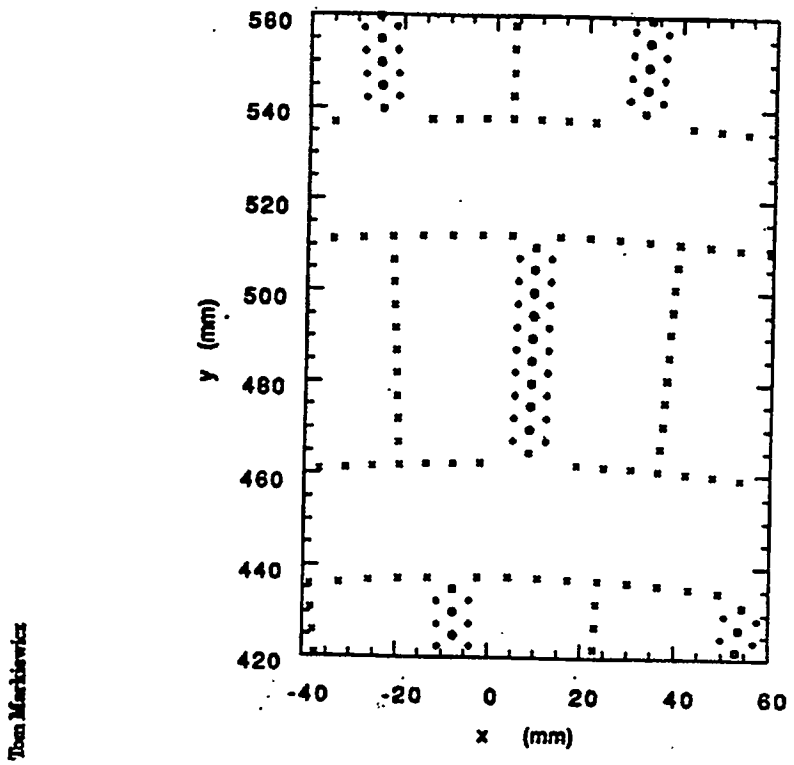

Figure 3.16: The points where the CDC wires attach to the ends of the CDC. One can see the structure of the super-layers and cells within them. The wires are of four types: high voltage field-shaping wires (crosses), guard wires (diamonds), signal, or *sense* wires (open circles) and dummy sense wires (squares).

charged particle's passing through the drift chamber gas. Liberated charge drifts in a constant electric field toward a charge-collecting wire called the *sense* wire. Just before the drifted charge reaches the sense wire it feels a much stronger electric field due to the smallness of the wire, and in this field an avalanche of electrons is created. This is what the sense wire collects. The CDC is comprised of 640 *cells*, distributed among 10 super layers. From the information within a cell, one *vector hit* is created. Vector hits, then, become the fundamental objects that go into the CDC pattern recognition algorithm, out of which, after much gnashing of teeth, finally come the helical particle tracks. For an excellent reference on pattern recognition see the thesis of David Williams [62].

Taken together, the CDC and VXD2 provide a momentum resolution of

$$\sigma^2[(\text{ GeV}/c)^{-2}] = (\delta p/p^2)^2 = (0.0026)^2 + (0.0095/p)^2 \tag{3.2}$$

and, including the uncertainty on the primary interaction point (IP), they give a combined impact parameter resolution of

$$\delta r_{IP} = 11 \oplus 76/(p_\perp \sqrt{\sin\theta})\ \mu\text{m}$$

where $p_\perp$ is the track momentum transverse to the beam axis in GeV/c. The result is a typical 2-prong vertex-finding accuracy of $\delta r_{V_{\parallel(\perp)}} = 240.0(24.)\ \mu$m for the direction along (perpendicular to) the resultant momentum.

The EDC works in the same way. Only the geometry of the super layers is different. In the EDC, however, there is the problem of large SLC background: mostly muons in a halo about the beam that pass through the inner regions of the end cap.

WIC Strips

Because of the fact that muons are too heavy to Bremsstrahlung and start electromagnetic showers like electrons, taken together with their relatively long Weak-scale lifetime, they are able to penetrate the entire SLD, including the steel in the WIC. This is untrue of hadrons up to very small penetration probabilities of order 10^{-4}, because they range out or decay or strongly interact. And it's absolutely[3] untrue of electrons because they *will* shower somewhere along their $\approx$ 26 radiation-length journey to the WIC. Muons of even modest energy ($\gtrsim 3$ GeV) merely lose energy by dE/dx (minimum ionization) before passing through the Iarocci tubes in the WIC. The strips (see figure 3.17) perform the usual business of reading out the deposited charge that drifts to the center wire in the Iarocci tubes. Hits on the strips are combined to form tracks in the WIC and are matched to hits in the CDC. The tracks which are well-matched to hits are checked to see if they are consistent with being fully-penetrating tracks. Satisfactory tracks are considered to be muons.

3.3.5 Calorimetry

Calorimeters measure the energy of incident particles by making them interact. The energy of the incident particle as well as the energy of the daughter particles is released

[3] Thus, absolutely here means with probability .999... (10 more 9s).

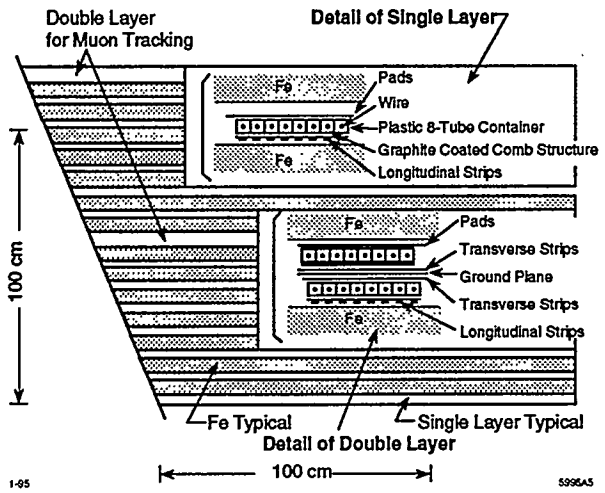

Figure 3.17: An $r\phi(xz)$ view of the barrel(endcap) WIC. Inlaid are the two types of WIC layers.

into the ionization of a low-Z material and the liberated charge induces signals that are measurable.

WIC Pads

The WIC Pads are also shown in figure 3.17. The WIC Pads gather charge in exactly the same manner as the LAC (section 3.3.5) and are similarly intended to help measure a particle's energy deposition. The WIC's contribution to the energy deposited in the whole calorimeter is typically $\lesssim 10\%$. Further, the WIC energy measurement is fluctuations-dominated [75]. That is to say, the error on the measurement is on the order of the value of the energy itself. Thus, the WIC pads have not been calibrated for general use and are turned off in the standard SLD event reconstruction. The WIC pads are ignored in this analysis. It is important to point out that the WIC serves as the support structure for much of the SLD and as the return flux path for the 0.6 Tesla magnetic field.

The Liquid Argon Calorimeter

The idea to use liquid argon was conceived in 1974 [76] and has been extensively studied and used. Liquid argon provides a stable and uniform energy response [77]. It is radiation hard in high energy environments. The LAC design and construction are described in great detail in [77]. Here we will give a description of its gross features and physics specifications.

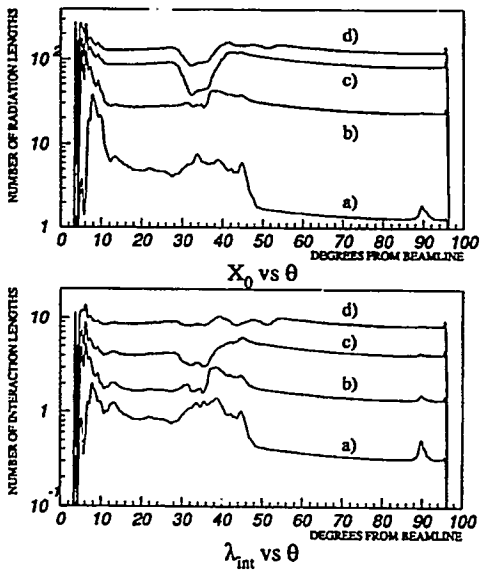

Figure 3.18: Material thicknesses (measured in units of radiation lengths, X_0, and strong interaction lengths, λ) in front of various sections of the Calorimeter. a),b),c),d) is just inside EM1,EM2,HAD1,HAD2, respectively.]

The LAC is made up of a barrel section (or more exactly, three barrel sections separated by two washers), and two endcaps. It sits not just inside the WIC but also inside the SLD solenoid (see figure 3.7) in order to minimize the number of interaction lengths particles must pass through before arriving at the LAC. (The solenoid alone is $\approx 0.7\lambda_{int}$ thick radially. Figure 3.18 shows the amount of material between the IP and various sections of the calorimeter.) The barrel inner wall, located at a radius of 1.77 meters, forms the CRID outer wall. The barrel LAC extends to 2.99 meters in radius. It is supported on the arches of the detector which also help hold up the WIC and the solenoid. The endcap is supported by the flux-return steel doors.

The barrel LAC covers the full azimuthal range and $|\cos\theta| < 0.98$, where θ, again, is the polar angle. This amounts to 98% of the full 4π solid angle coverage. By itself the barrel covers $\theta > 33°$, while the endcap covers $35° > \theta > 8°$, for $\theta < 90°$. The same expressions hold for $\theta > 90°$ with θ replaced by $180° - \theta$. There is thus overlap on each end between the endcap and the barrel[4].

[4] Both endcap and barrel sections are comprised of both "electromagnetic" (EM) and "hadronic" modules (HAD). Examination of figure 3.7 reveals that in this region of overlap there are only EM

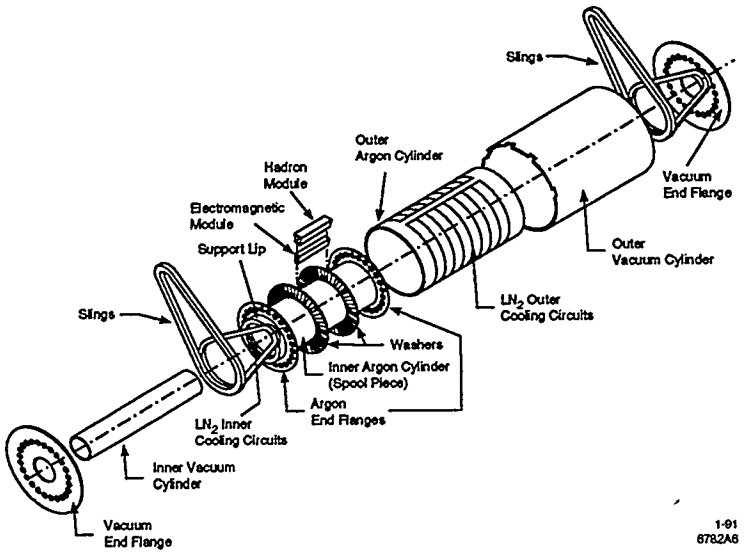

Figure 3.19: LAC barrel, showing the placement of one barrel module.

The construction is as follows. The three sections that comprise the barrel are made up of 48 EM modules around the azimuth and 48 more HAD modules stacked radially on the EM modules. Thus, in the barrel there are $(48 + 48) \times 3 = 288$ modules. See figure 3.19 for an illustration of how the modules fit within the overall barrel assembly, including the cryostat. Each of the two endcaps are composed of 16 wedge-shaped modules, with each module containing both EM and HAD sections (see figure 3.20). The modules – both barrel and endcap – may be seen in figures 3.21 and 3.22, respectively. The modules are constructed as parallel plate liquid argon ionization chambers, with alternate planes of large, grounded, lead sheets and segmented lead tiles and liquid argon filling the gaps (see figure 3.23). The segmented tiles conform to a pointing geometry – *i.e.,* they are lined up with one another along lines running radially outward from the IP. A *cell* is defined as lead sheet/Ar/lead tile/Ar. A further feature of the LAC is that within both the EM and HAD modules there is a division at half the radial depth of the module, forming effectively 4 layers

---

modules. Studies that are sensitive to the measurement of energy as a function of polar angle, therefore, such as certain 3-jet analyses, must be careful about the appropriate energy scale in this region [78]. A discussion of the use of the appropriate energy scale can be found in section 4.3.2.

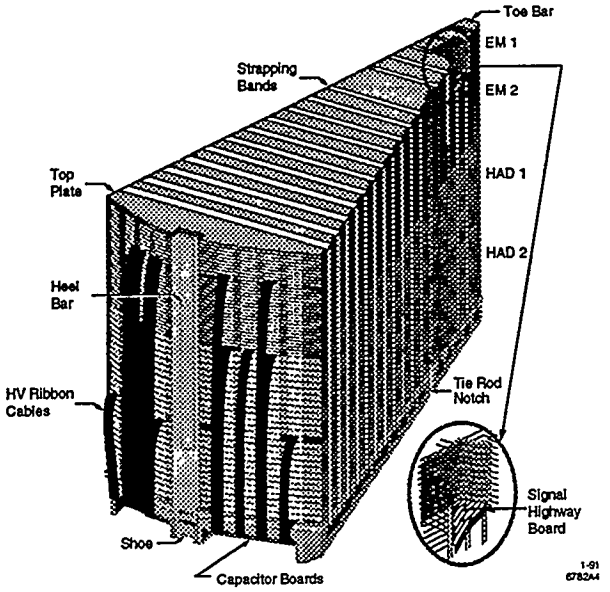

Figure 3.20: A LAC endcap module.

as one moves out radially, EM1, EM2, HAD1 and HAD2. (This will be an important feature that is exploited in the method by which we measure the neutral energy with the calorimeter and will be explained in section 4.2.) The cells are grouped together as indicated in table 3.3. Note that the HAD cells are made of thicker lead sheets and tiles. Further, they are twice the size of the EM tiles in both transverse dimensions, providing a coarser measure of the position of a shower – appropriate for the larger size of hadronic showers compared with electromagnetic showers. The radial ganging together of these cells in numbers given by table 3.3 forms the fundamental energy-measuring unit of the LAC: *towers*. It is towers that are eventually grouped together by the software to be described in section 4.2 as *clusters*, which are claimed to give a particle's total energy and direction. The total number of these towers in each section of the LAC is seen in table 3.2. To give a typical tower size, and thus to get an idea of the spatial resolution of the LAC – that is, the minimum discernible separation of two particles traversing the LAC – it is worth noting that in the barrel at $\theta = \pi/2$ an EM tower has a width of $\delta\theta = 36$ mrad and $\delta\phi = 33$ mrad[5]. The

[5] In the EM modules $\delta\phi = 33$ mrad for all ϕ, but because of the axial geometry of the modules $\delta\theta$ falls to 21 mrad at the end of the barrel. Tower $\delta\theta$s fall like $1/\cos\theta$ as one moves out to the

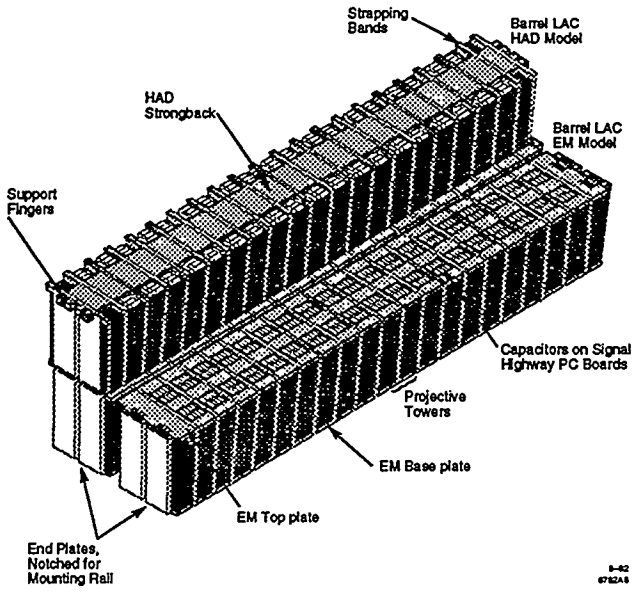

Figure 3.21: A LAC barrel module.

LAC energy resolution $\frac{\sigma_E}{E}$ is estimated to be $\approx 0.65/\sqrt{E}$ for hadronic showers and $\approx 0.15/\sqrt{E}$ for electromagnetic showers, with E in GeV [79].

The LAC in this analysis is used to make a measurement of the neutral energy in each event. It acts here, as well, in its usual function as a hadronic event trigger. This trigger will be described in section 4.1.1.

Getting the LAC data to tape

To give a rough idea how the process of gathering the data at the SLD and getting it on to tape really goes, it is worth tracing the relevant steps for the LAC. This requires a discussion of the LAC electronics.

Essentially the story is this: one millisecond before each beam-crossing – which occur every 8 milliseconds – a FASTBUS[6] [80] timing and control module (TCM) switches on the power to the electronics on every LAC "Tophat" Motherboard. After the beam crossing the analog signal from each tower is fed to a pre-amplifier, shaper and a sampler on a daughterboard from which it is finally fed to a multiplexed Analog-

endcaps. This is done to keep the solid angle $d\phi d\cos\theta$ constant for each tower.

[6] *The* acquisition hub that, finally, takes the detector's readout upstairs to the acquisition computer, where event filters are applied.

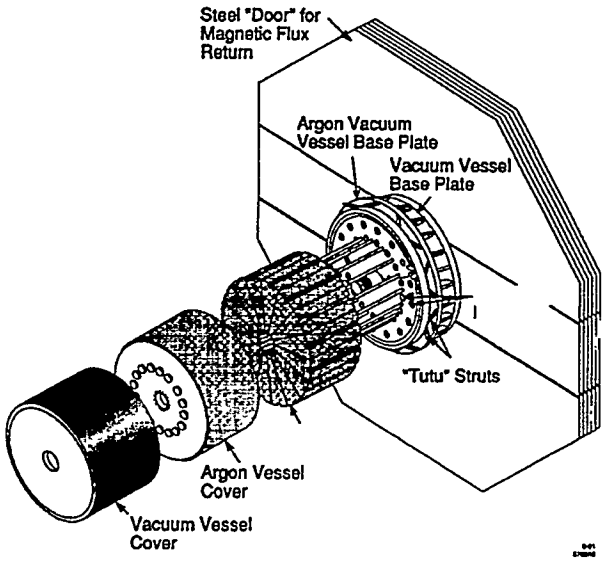

Figure 3.22: LAC endcap, showing the placement of one endcap module.

to-Digital Converter (ADC). In the barrel there are 720 channels (one per tower) on 15 daughterboards on each Tophat (see figure 3.24).

The preamplifier is responsible for taking a given tower's input signal (a charge), amplifying it, creating an appropriate sized voltage ($V = Q/C$, if the response were perfectly linear), and shaping it. The calculation of the appropriate sized voltage is done by the preamps in concert with the Calorimetry Data Module (CDM). After the execution of the LAC calibration process[7] the calibration constants reside in the CDM memory until the next successful calibration, at which point they're over-written in favor of the new constants. The CDM then does the sampling of the signals by: (1) Selecting the high or low gain depending on pulseheights, (2) applying calibration constants, (3) performing a signal−baseline subtraction, (3) checking for tower signals over threshold. The 32 CDMs, which read and process data from two tophats each, finally, report the size of these signals and their corresponding Tower ID to the AEB

[7] Calibration is performed from a data acquisition workstation in the SLD control room, typically once a day by the Shiftees. A single command from such a workstation with the FASTBUS in Calibration Mode puts a $2.5V$ signal on $8.4pF$ capacitors through a digital-to-analog converter (DAC), for each LAC tower.

Table 3.2: Number of LAC modules and towers

LAC module and tower counts		
Module type	Modules	Towers
Central barrel EM	48	48(112+112)
Central barrel HAD	48	48(24+24)
End barrel EM	2(48)	96(84+80)
End barrel HAD	2(48)	96(20+18)
Endcap (EM+HAD)	2(16)	32(117+105+27+21)
Total barrel	288	32448
Total endcap	32	8640

Table 3.3: LAC cell count in units of radiation length and (strong) interaction length.

LAC radial segmentation					
LAC Section	Cell Count	Cell X_0	Section X_0	Cell λ	Section λ
EM1[a]	8	0.75	6.0	0.030	0.24
EM2	20	0.75	15.0	0.030	0.60
HAD1[b]	13			0.077	1.00
HAD2	13			0.077	1.00

[a] EM cell: 2.0 mm Pb, 2.75 mm Ar, 2.0 mm Pb, 2.75 mm Ar

[b] HAD cell: 6.0 mm Pb, 2.75 mm Ar, 6.0 mm Pb, 2.75 mm Ar

(ALEPH event builder) in the LAC FASTBUS. The AEB ensures that only data in the CDMs from the same event is read and ships it to the shared event pool. A process running on the data acquisition VAX pulls events out of the shared event pool and writes them to tape. Meanwhile, under the guidance of the TCM (though not as often here as every beam crossing) low voltage, high voltage, and cryogenic information is monitored through separate CAMAC systems.

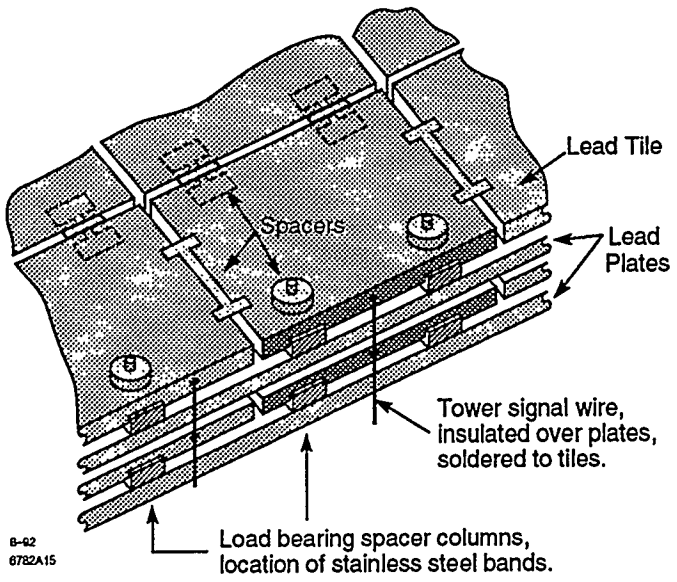

Figure 3.23: A LAC cell.

3.3.6 Monte Carlo Simulation

In order to extract the desired physics, most analyses at high energy experiments rely on a good understanding of their apparatus via its Monte Carlo simulation. This is because the physics processes of interest in these experiments, *i.e.* particle production, scattering, decay, etc. are quantum mechanical and quantum field theoretical in nature. Additionally, particle interactions with the detector are non-trivial. One needs to know how the detector will respond to a variety of processes. The Monte Carlo generator simulates the e^-e^+ collision, including initial state radiation, and is responsible for creating the partons, leptons and bosons with 4-momenta appropriate to the underlying process, and the scattering amplitude $\mathcal{M}$. The generator, further, decays short-lived (here $\tau \lesssim 10^{-16}$ particles and "assembles" partons into hadrons[8]. Control is then handed over to the Detector Simulation. The detector simulation "swims" particles through the detector, decaying them as appropriate, and simulating the interactions with matter – Bremsstrahlung, strong interactions (*i.e.* $\pi^+ n \rightarrow p\pi^0$), and the ordinary dE/dx scattering off electrons. As one might expect,

[8] more on this in chapter 2

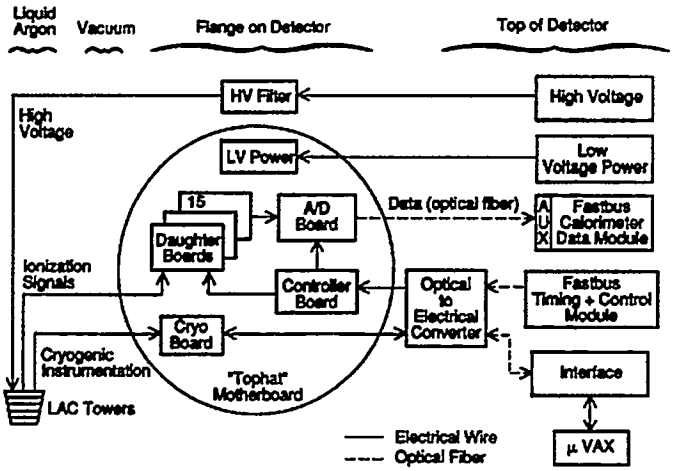

Figure 3.24: LAC electronics showing one tower, one "Tophat" and scheme for getting the signal to the FASTBUS.

there is largely *swimming* out from the IP through the mainly-vacuum VXD2 and CDC out to the CRID – which is heavy and full of stuff – at which point there is mainly material-dominated scattering all the way through the LAC to the WIC – if a particle gets that far, which it usually doesn't unless it's a muon.

3.3.6.1 Physics Simulation

If we are going to be relying on the MC to give a good description of the B decay and of the detector (which we are) it is worthwhile to ask if the data and the MC bear any resemblance to each other. Thus, we embark on a description of the gross features of the MC, as it regards

$$Z^0 \rightarrow q\bar{q} \rightarrow hadrons. \tag{3.3}$$

There are many MCs on the market, but we will discuss here only two: the JETSET and HERWIG Monte Carlos. For a review of these and many others see reference [75].

Parton Generation

The first half of equation 3.3 *plus* the further step of perturbative creation of partons is discussed here.

The SLD experiment uses JETSET7.4 to simulate its 1993 and 1994/1995 runs, respectively. The default parameters are listed in table 3.4.

Table 3.4: JETSET7.4 MC parameter values

Parameter purpose	Symbol	Value
pQCD phase space cutoff	Q_0	1.0 GeV
$\overline{\text{MS}}$-scheme QCD parameter	Λ	0.26 GeV
controls p_T of Hadron	σ_q	0.39 GeV
Lund *uds* Frag. Parameter 1	a	0.18
Lund *uds* Frag. Parameter 2	b	0.34
Peterson c Fragmentation	ϵ_c	0.06
Peterson b Fragmentation	ϵ_b	0.006

Within the JETSET MC one has two options for the perturbative generation of partons: matrix element (ME) or parton shower (PS). In the ME option gluon radiation occurs according to the $\mathcal{O}(\alpha_S^2)$ matrix element describing the underlying process. This means that at most there will be four partons in the final state. By KLN (section 2.2.1) we know that such a process is finite, if all appropriate diagrams are considered, but in order to avoid the difficulties of numerical cancellation of opposite-signed huge numbers, one introduces a cutoff Q_0 that prevents the generation of "too" soft or "too" collinear partons. Alternatively, one may use the PS approach, which is the one used in the official SLD MC and in this analysis, in which partons are split off the outgoing quarks and antiquarks according to the splitting functions in equations 2.15, and the splitting continues on down until the final partons each have an invariant mass greater than or equal to Q_0. This is done in order that we are left with a finite number of partons. The PS method, arguably the more physical of the two, is known to do a better job with the 4-jet rate [75]. The PS method is the only one used in the HERWIG MC. The rest of the parameters in table 3.4 are Λ_{QCD} – the usual QCD scale[9]; σ_q – the parameter for the gaussian selection of hadron p_T; a and b – the Lund fragmentation function parameters used for light flavors; and finally ϵ_b and ϵ_c – the Peterson fragmentation function parameters used for the b and c. There, of course, are many other parameters which control the operation of the JETSET MC. One other one which we mention here because of its relevance to the calculation of

[9] which has meaning in a particular regularization scheme, consistent with the one chosen ($\overline{\text{MS}}$) in which to do the 4-parton ME calculation.

the systematic error in the final chapter of this thesis is the one that controls s quark production, PARJ(3), whose default value is 0.28.

Hadronization

Here we discuss the second half of equation 3.3.

In the Lund MC the mechanism of hadronization proceeds as described earlier in section 2.5.1, where it (the description) arose naturally as an extension of the Lund parametrization of the fragmentation function. There we discussed how partons were produced and subsequent $q\overline{q}$ production allowed for the formation of mesons (and baryons upon consideration of $qq\overline{qq}$ production). One can imagine that instead of starting with just one q and one $\overline{q}$, one starts with the collection of qs, $\overline{q}$s and gs that one is left with after application of one of the parton-generation procedures described above. The hadron's p_T is generated as described there as well. If this is done, we have Lund hadronization.

HERWIG hadronization is an interesting story. As mentioned above, we generate multiple partons via the PS procedure, but in so doing color indices are assigned, and further, the Next-to-Leading-Log approximation for soft or collinear gluon emission is used – to be compared to merely the LLA in JETSET. This is accomplished by enforcing Strict Angular Ordering, described in section 2.4.1. Any final state gluons are split into a $q\overline{q}$ pairs. Color indices are connected by lines and any given line can be followed from quark to antiquark or quark to diquark to form a color singlet "cluster". These clusters have a mass distribution that peaks at a low value and is asymptotically independent of the hard subprocess scale [81]. This is exactly the property we know LPHD predicts, and it permits the factorization of the hard, perturbative processes from the hadronization process. If such a cluster is too light to decay into two hadrons, it is taken to be the lightest hadron of its flavor by exchanging the appropriate amount of momentum with a nearby cluster. Other clusters decay into hadron pairs. Quark and diquark flavors are chosen at random (not according to their mass!), and the subsequently formed hadron is chosen at random from a table of hadrons of those flavors and of all physical angular momentum values. See figure 3.25 for the color structure of a $p\overline{p}$ event. HERWIG is not used in this analysis because the B decay is not tuned in the SLD implementation. The x spectrum peaks at the unacceptably low value of ≈ 0.5.

An Example: MC B Decay

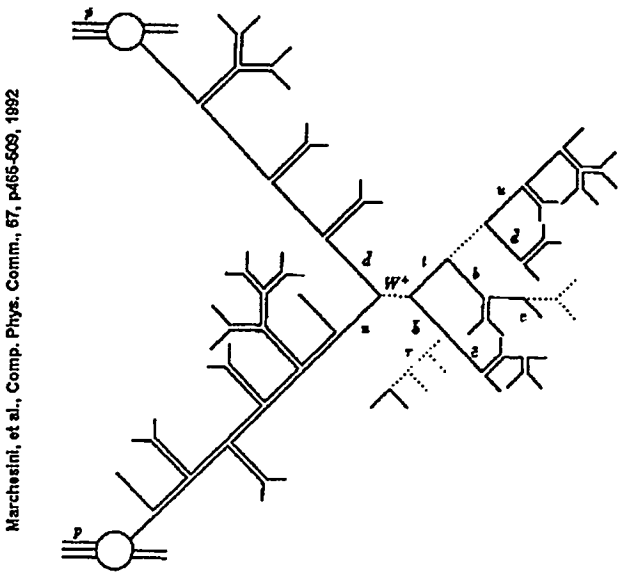

Figure 3.25: HERWIG color connection in a $p\bar{p}$ event.

In particular, the correct description of B decay needs to be incorporated into the simulation. Figures 3.26 and 3.27 provide compelling evidence that the various B decay modes (measured largely at CLEO) are well-modeled by the tuned B decay in the Monte Carlo.

3.3.6.2 Detector Simulation

We need to demonstrate that the detector, as well as the physics, is well-modeled by the MC. The upper left plot in Figure 3.28, interestingly, shows an infamous SLD MC/data disagreement: a 3% difference in the mean number of tracks found in MC and data events. As of this writing, there remains no definitive answer to this problem. For the purposes of this analysis the tracks are used to find (hopefully "Real") vertices[10] and to reconstruct the B tracks and charged energy. These quantities are in good agreement, and so the 3% disagreement is harmless here.

Turning to the LAC, figures 3.29 and 3.30 show agreement between MC and data for various event quantities. Most of the (slight) disagreements are due to the endcap

[10] "Real" vertices to be defined in section 4.1.3

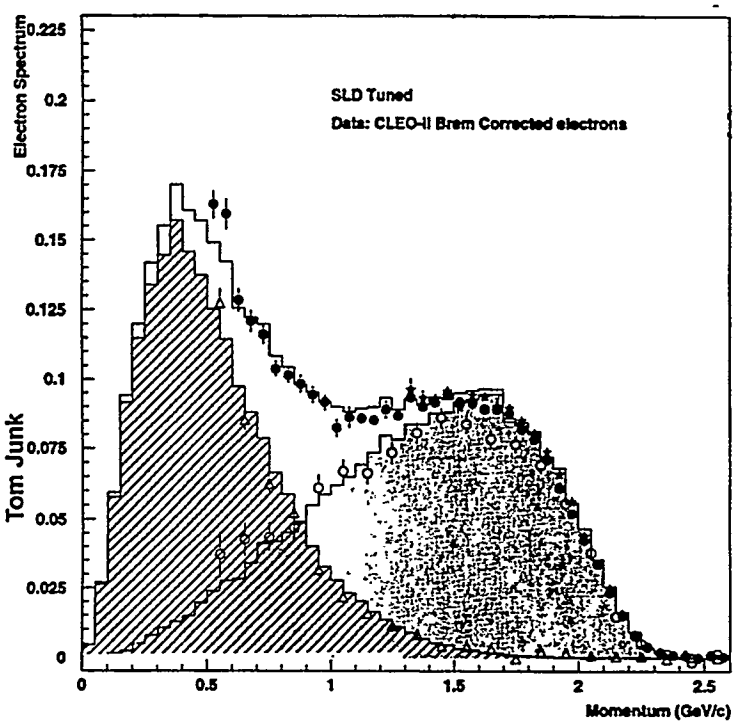

Figure 3.26: Shown [82] is the SLD e^- spectrum (stars and filled-in circles – not to be differentiated) compared to the SLD-tuned, CLEO B-decay MC model. The data and MC consist of two contributions: e^-s from semi-leptonic B and D decay (the high momentum peak, which is based on an Isgur-Wise HQET calculation) and all other e^-s (the low momentum peak). The agreement is impressive.

simulation, where the MC response is better than the data response. This analysis avoids this problem by requiring $\cos\theta_{thrust} < 0.71$. We take confidence from the energy plots in particular that we understand the calorimeter, and our corrections back to the neutral B energy in chapter 4 will be reasonable (if the B decay model is reasonable, which figures 3.27 and 3.26 show it to be). Figure 3.31 shows various cluster quantities compared between MC and data. The energy in each cluster as a function of its position in the LAC agrees well. It's also clear the EM and HAD sections of each cluster are well-described.

Of particular concern is a quantity we will call G_c,

$$G_c = \frac{E_{EM_1} E_{EM_2}}{(E_{EM_1} + E_{EM_2})^2} \tag{3.4}$$

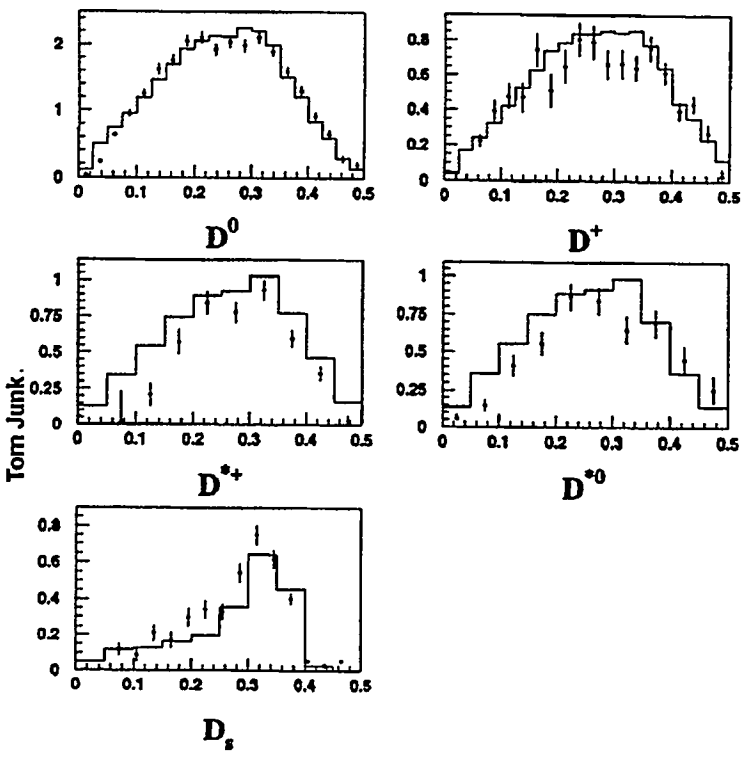

Figure 3.27: Shown [82] are the SLD D spectra from B decay (points) compared to the SLD-tuned, CLEO B-decay MC model (histogram). The variable histogrammed here is the scaled D energy, E_D/E_{beam}. The relative normalizations indicate the relative production fractions of the different D types.

which characterizes the shower energy deposition into layers 1 and 2 of the electromagnetic part of the LAC. It is shown in Figure 3.32. In the cluster selection for this analysis only clusters for which $G_c > .15$ will be considered when formulating the energy flow, due to poor MC-Data agreement for $G_c < .15$. It is also true that e^-/π^- distinction is performed largely with the aid of G_c, and so it must be accurately modeled in the MC.

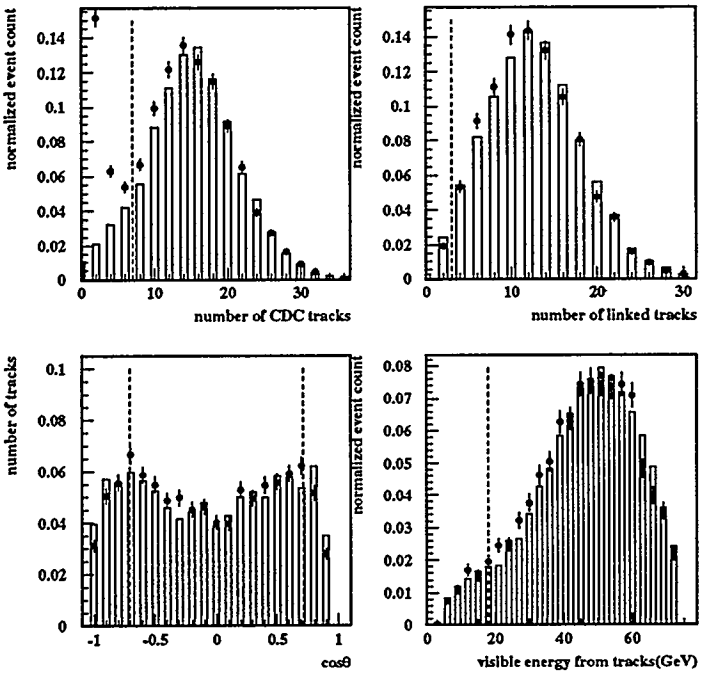

Figure 3.28: MC/data: Track multiplicity [83]. There is a 3% difference between data and MC in the mean in the upper left plot. "Linked tracks" means number of tracks in the CDC that are linked to tracks in VXD2. MC is the histogram; data are the points.

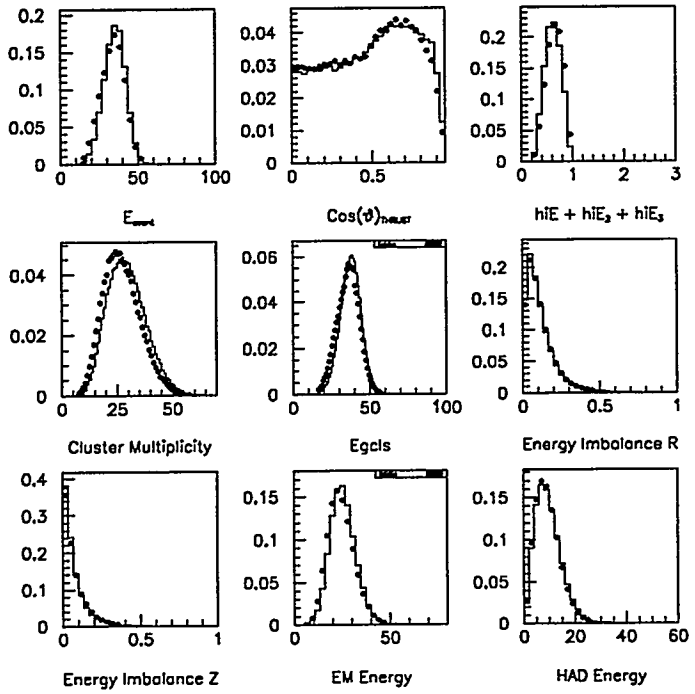

Figure 3.29: MC/data: Calorimeter event quantities I. Shown are E_{event}, $|\cos\theta_{thrust}|$, $hiE + hiE_2 + hiE_3$ (the sum of the 3 highest scaled cluster energies in each event), n_{clus}, E_{gcls} (energy sum in "good" clusters in an event), Energy Imbalance (the scaled missing momentum vector for both R and Z components) and the event energy in the EM and HAD sections. MC is the histogram; data are the points. All plots normalized to 1 entry.

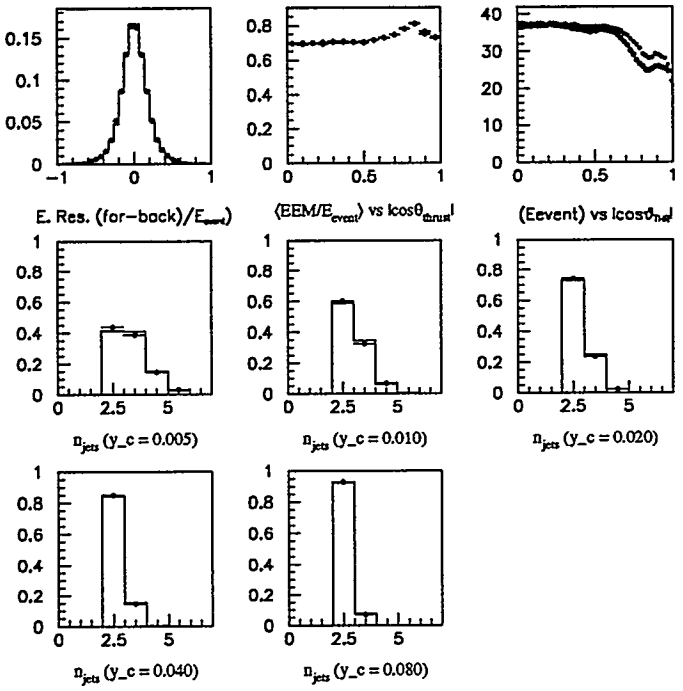

Figure 3.30: MC/data: Calorimeter event quantities II. Shown are the event Forward-Backward energy asymmetry, EM energy fraction vs. $\cos\theta_{thrust}$ (note the peak where the hadron calorimeter is largely absent), E_{event} vs. $\cos\theta_{thrust}$, and the number of jets in the event for the Durham algorithm and y_c as labeled. All plots normalized to 1 entry, except $\langle EEM/E_{Event}\rangle$ vs. $\cos\theta_{thrust}$ and E_{event} vs. $\cos\theta_{thrust}$.

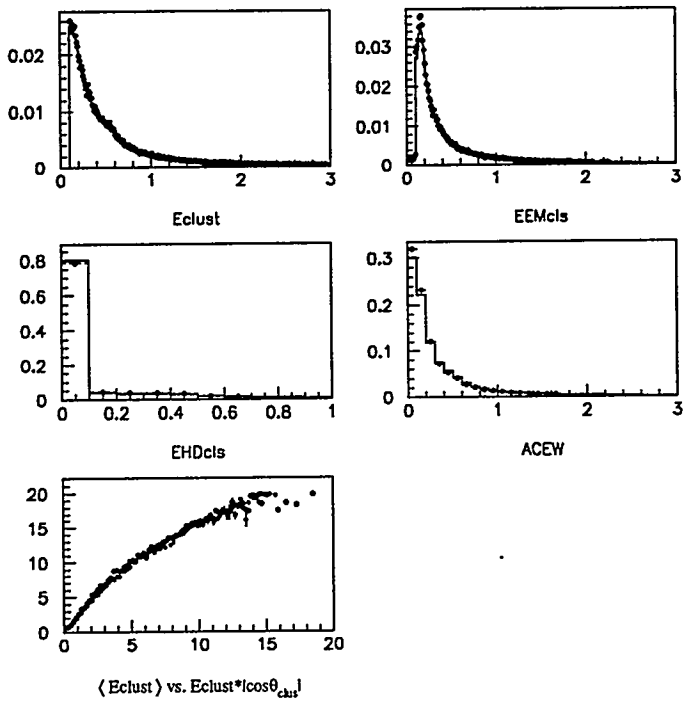

Figure 3.31: MC/data: Calorimeter clusters. Shown are E_{clus}, $E_{clus_{EM}}$, $E_{clus_{HAD}}$, $E_{clus} \cdot |\cos\theta_{\mathbf{clus}}|$, and E_{clus} vs. $E_{clus} \cdot |\cos\theta_{\mathbf{clus}}|$. MC is the histogram; data are the points. Top four plots normalized to 1 entry.

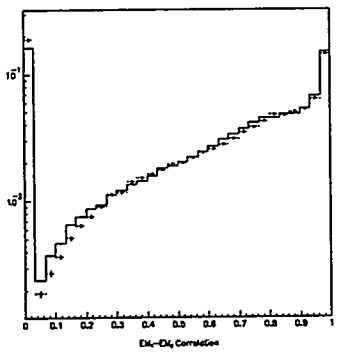

Figure 3.32: MC/data: Kal cluster quantity G_c.

Chapter 4

EVENT SELECTION, RECONSTRUCTION, AND THE LAC ENERGY SCALE

4.1 Trigger, On-line Filter and Event Selection

In this section we will examine the means by which we select events appropriate to the analysis. This is done in three steps, with a preliminary tag designed to find events in which $e^+e^- \rightarrow Z^0 \rightarrow f^+f^-$, where $f^\pm$ are fermions and antifermions — *i.e.* the generic category of events for which the SLD was built.

The agent which is responsible for finding this broad class of events is the *trigger*. There is more than one trigger intended to find such events, and there are triggers which are intended to find other events than this. Aside from these latter triggers it is true that beam-crossings in which the process $e^+e^- \rightarrow Z^0 \rightarrow f^+f^-$ is determined *not* to have occurred are not even written to tape and no one at SLD cares about them for purposes of doing physics — though one can imagine one other physics process of note that might be studied: $e^+e^- \rightarrow Z^0 \rightarrow e^+e^- hadrons$. In order not to process lots of background that remains after this trigger has been fired, a filter (called the `PASS1` filter) is applied, and it will be next to be discussed.

The second step in the event selection is to find events in which the Z^0 decays hadronically, namely $Z^0 \rightarrow q\bar{q}$.

Third, we want to select our particular topology, $B \rightarrow l\nu_l D$ as pictured in the "Feynman diagram" of figure 4.1, from this remaining collection of events.

A few words on assorted necessary topics to cover when doing an analysis with SLD follow. There will be an emphasis on understanding the LAC throughout.

4.1.1 The Trigger(s)

With each beam crossing, the hardware in the subsystems of the SLD report their signals. In the CDC waveforms are read out by collecting the ADC signals corresponding to liberated charge as a function of time. In the LAC the ADC counts

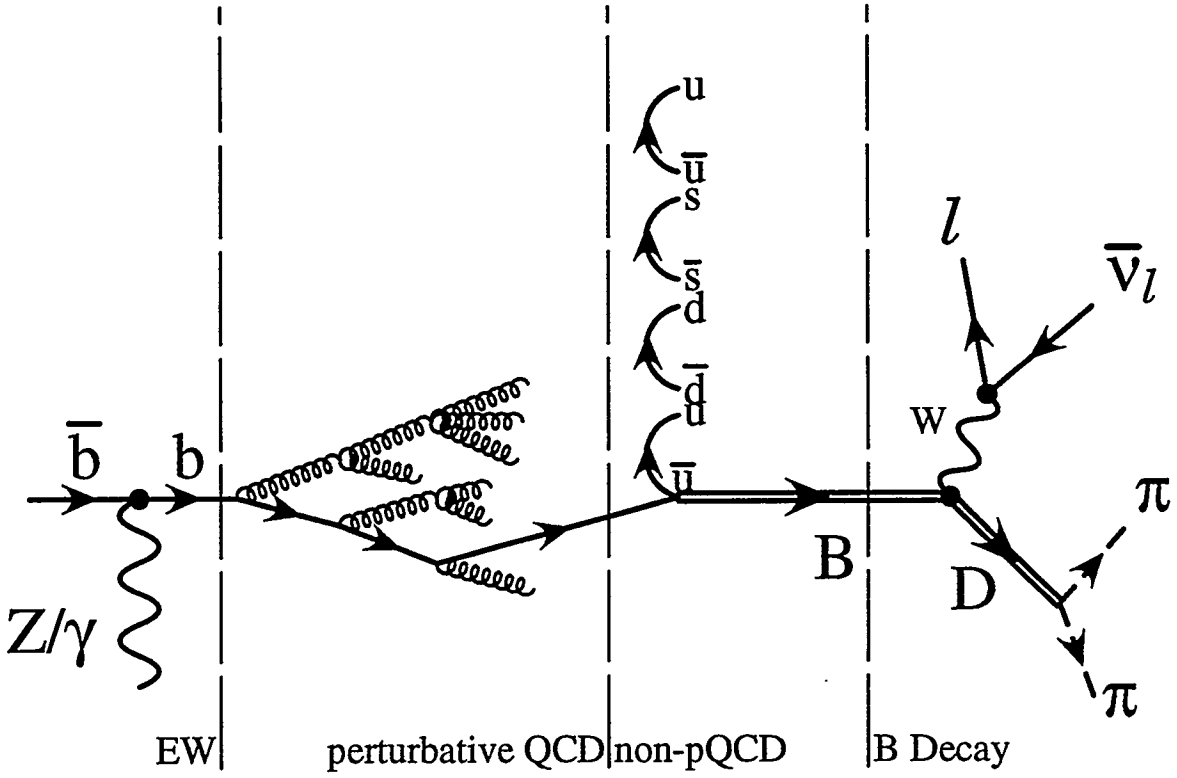

Figure 4.1: The topology under study, showing the various stages of the process. The D$\rightarrow \pi\pi$ is symbolic of any 2–prong seed vertex. Extra tracks may be added to the vertex in the way described in the text. The π may in fact be a K; for the energies of the tracks which form a vertex ($\gtrsim 1.5$ GeV) the error made by assuming $m_{\pi^\pm}$ is negligible.

corresponding to total deposited charge in each of the towers are read out. Certain combinations of particular signals are formed each beam crossing into *triggers*.

Different triggers are designed to find different categories of events. For example, in order to measure the SLC luminosity one wants to find so-called "t-channel" $e^+e^- \rightarrow e^+e^-$ events. (The motivation for this was discussed in section 3.3.2.) To do this, the LUM is employed. There exists a trigger which is evaluated every beam crossing and is satisfied (and thus the event is written to tape) if there exists a hit in a bin in $\theta - \phi$ in the North LUM detector simultaneously with one in the South LUM detector in the 180°-opposite $\theta - \phi$ bin. It is possible that an event causes more than one such trigger to fire, so each triggered event comes with an event record in which

the bits of a particular word are set that correspond to all the fired triggers for that event.

In our case we want events that have either the Hadronic[1] event bit set or the Track bit or the Energy bit set. These are the names of the three triggers that are designed to catch hadronic events. We will focus on the Hadronic trigger, and mention only briefly the following information about the Track and Energy triggers, which are also intended to find hadronic events. The Track trigger requires merely two well-separated CDC tracks, and the Energy trigger requires at least 4 GeV in the LAC and one track in the CDC.

The Hadronic trigger is satisfied in the following way. The barrel and endcap LAC towers each contribute to one or both of the following sums after each ADC tower hit value is converted to GeV, using the number in the third column in table 4.1[2].

We define

$$E_{HI} = \sum_{all\ towers} E_{tower} \text{ if } E_{tower} > E_{HI}^{min},$$

where E_{HI}^{min} is chosen to be significantly above the energy of a typical muon's *mip* energy deposition. The sum over *"all towers"* excludes those in the "ring of fire" – the two θ bins (for all ϕ) closest to the beam pipe on each endcap module. We require that $E_{HI} > 8$ GeV in order for the Hadronic trigger to be satisfied.

The purpose of choosing this one E_{HI} requirement and for requiring[3] that $E_{LO} \leq$ 140 GeV, where

$$E_{LO} = \sum_{all\ towers} E_{tower} \text{ if } E_{tower} > E_{LO}^{min},$$

is to avoid writing events to tape which contain nothing but the SLD's biggest background source: SLC muons that go flying through the SLD largely parallel to the beam line, caused when the tail of the e^- or e^+ bunch hits an upstream collimator. E_{LO}^{min} is chosen to be right at the *mip* threshold. E_{HI}^{min} and E_{LO}^{min} for the EM and HAD sections of the LAC are listed in table 4.1.

---

[1] Notice the capitalization of the word "Hadronic," as this is the name of one particular trigger that we will discuss here.

[2] This ADC→ GeV conversion involves a sampling fraction correction, where the sampling fraction is given by $\frac{dE/dx|_{Ar}}{dE/dx|_{Ar}+dE/dx|_{Pb}}$ and is different for each layer in the LAC, and a choice of energy scale in the LAC, which we take for simplicity to be the minimum ionizing particle *mip* scale.

[3] applied in the `PASS1` filter, to be discussed next

Table 4.1: E_{HI}^{min} and E_{LO}^{min} and *mip*-scale

Tower type	E_{LO}^{min}(ADC)	E_{HI}^{min}(ADC)	*mip*-scale (ADC/ MeV)
EM	8	60	2.8
HAD	12	120	7.5

E_{LO} is given to the SLC operators as a real-time noise signal and will be used later in further event processing decisions. The number of EM towers that contribute to E_{HI}, N_{EMHI} is also recorded for use in the next stage.

4.1.2 The Filter

The E_{LO} requirement is utilized in the next stage, the application of the PASS1 filter. It requires that E_{LO} must be less than 140 GeV. Again, like the E_{HI} requirement designed to prevent triggering on events where there are not enough robust, hadronic energy towers lit-up, the E_{LO} requirement is made to ensure that there are not lots of low energy towers lit-up – the complementary indication of the passage of an SLC muon. The other PASS1 requirements are that $N_{EMHI} \gtrsim 10$ towers, $E_{HI} > 15$ GeV, and $E_{LO} < \frac{2}{3}E_{HI} + 70$ GeV. After the application of PASS1, we have only roughly 2% of the events left that satisfied the trigger. These 2% now go on to be "reconstructed" (see section 4.2). An invaluable amount of tape and later, processing time, is saved by eliminating these background-dominated events. The $E_{HI} - E_{LO}$ plot for the 1993 data is seen in figure 4.2. MC studies show that the central oval is full of hadronic Z^0s and some $Z^0 \rightarrow \tau^+\tau^-$ events, while the stripe along the line of slope 1 is mainly $Z^0 \rightarrow e^+e^-$ events, and the band along the bottom are background muon and $Z^0 \rightarrow \tau^+\tau^-$ events.

All events which now remain go to be Reconstructed. Reconstruction is the name for the process that takes all the raw data and converts it into the analyzable data, writing it to the Data Summary Tapes (DST). To achieve this, each subsystem has quite-involved processes that run at this stage. Reconstruction, for example, in the CDC means taking the waveform information and doing the whole business of taking vector hits and feeding them to the pattern recognition machinery, etc. , and finally coming up with tracks whose properties are stored in a bank called PHCHRG. In order to gain a better understanding of what sorts of things need to be done, in a subsequent

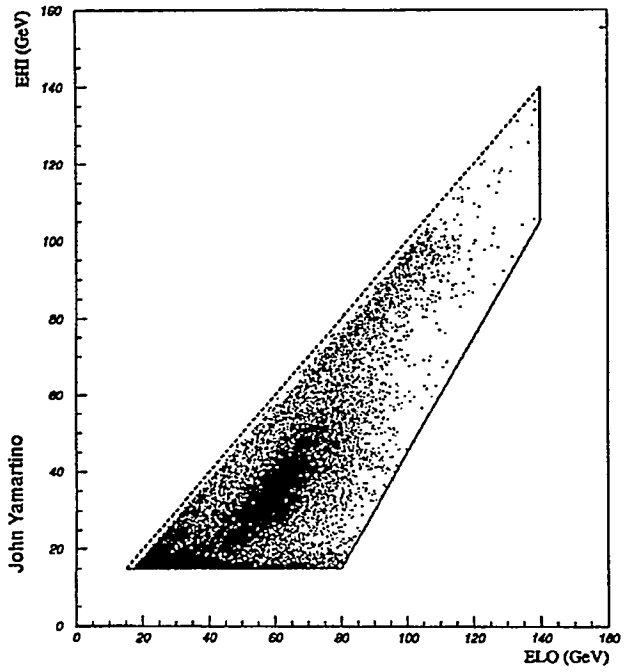

Figure 4.2: The scatter plot of $E_{HI} - E_{LO}$ [84]. These events all go on to be reconstructed. See text for definition of E_{HI} and E_{LO} and the physics events contained in the various clumps of points.

section (section 4.2) we will examine in more detail what reconstruction in the LAC entails.

4.1.3 Event Selection

Here we want to winnow our current collection of Z^0s to those events containing semi-leptonically decaying B hadrons.

$Z^0 \longrightarrow q\bar{q}$

We begin by further purifying our $Z^0 \rightarrow q\bar{q}$ events. In this analysis, all the reconstructed events out of the PASS1 filter are subject to the following requirements. There must be seven good tracks whose total energy $E = \sqrt{\vec{p}^{\,2} + m_\pi^2}$ is 20 GeV. A "Good track" is one whose r and z distances of closest approach are less than 5 and 10 cm, respectively, has its component of momentum perpendicular to the

Table 4.2: s.l. B decay modes [85] $l = e, \mu$.

Decay	B.R.
$B \to Dl\nu_l$	2.5%
$B \to D^* l\nu_l$	5.9
$B \to D^{**} l\nu_l$	2.5

beam axis, $p_\perp$, greater than 150 MeV, and, finally, is well-contained in the CDC: $|\cos\theta_{track,beam}| \lesssim 0.8$. For the purposes of this analysis, where we want to use the vertex detector, we want to exclude events whose underlying $q\bar{q}$ pair axis is in a direction that sends the resulting hadrons and decay products into the endcaps of the detector. One approximates the direction of this axis by the thrust axis (see section 2.7), and requires that the cosine of the angle made by the thrust axis and the beam axis, $\cos\theta_t$, satisfy $|\cos\theta_t| \leq 0.71$. These cuts in combination with the trigger and PASS1 cuts are shown [84] to have an efficiency of $\approx 95\%$[4], with an estimated $\approx 0.20\%$ background, dominated by $Z^0 \to \tau^+\tau^-$ events.

B hadrons: General Tagging Strategies

Our next aim is to find B hadrons. The B hadrons are the B mesons – comprised of a b quark and an anti-quark – and the Λ_b baryons – comprised of a b quark and two of the uds quarks. They can be charged or neutral and can exist in all allowed angular momentum states. Each type may decay in many possible ways. This analysis is deliberately inclusive, and thus we have not concerned ourselves with all the possible final states. Table 4.2 lists the three broadly categorized s.l. B modes. We assume Λ_b and B_s decay may be treated in the same manner as the other B hadrons, and we will study errors caused by variations from its expected production and decays in section 5.4.1. There are way too many D decays to list them all, so we merely note here that the D^{**} and D^* particles decay to D particles by emission, often, of π^0s and γs. This will result in a fluctuation of the total neutral energy attributable to the B. The uncertainty on the resulting degradation of the B energy resolution is taken into account by varying both $D^{(*)*}$ production ratios and the fit on the reconstructed neutral energy, as explained in section 5.4.1.

The feature to be exploited in most searches for B hadrons is the long lifetime of

[4] meaning 95% of the $Z^0 \to q\bar{q}$ events that are contained in the CDC are found

these particles. The mass of any B is at least as large as the (constituent) mass of the b quark, taken here to be ≈ 5 GeV. When a b leaves the e^+e^- IP and becomes a B hadron, its boost and lifetime are such that B decay lengths are typically about 3 mm. VXD2's ability to measure the impact parameter (with respect to the IP[5]) of tracks with a resolution of better than 150 μm, combined with the small and stable SLD beam spot size, makes for a high efficiency of secondary vertex finding. Thus, in order to tag B hadrons one may look for 2- or higher-prong vertices that are displaced by about 3 mm.

In fact, it turns out to be enough [86] to simply require that there are N tracks whose two- or three-dimensional impact parameters, normalized by their respective errors, $\frac{\sigma}{\delta_\sigma}$ are greater than d, where typical values for N and d are 3 and 3.5, respectively. One can define such a tag for the whole event or for the individual hemispheres. Hemispheres in this thesis are defined by the event thrust axis, from KAL information. Using CDC tracks to define the thrust axis will be biasing due to the limited acceptance of the CDC. The expected $\propto (1+\cos^2\theta)$ behavior of the thrust angle will not follow from the CDC-derived thrust. Increasing N and d increases the B tag's purity, Π, while lowering the tag's efficiency, ε. Generally, one sees a family of $\Pi - \varepsilon$ curves plotted, with one curve for each value of $N = 2, 3, \ldots, 6$, with d running, along each curve, from 2.0 to 5.0 in increments of 0.5. This is a significant impact parameter tag. See figure 4.5. One sometimes sees significant impact parameter tagging performed in a little bit more sophisticated manner in the method called the Impact Parameter Probability Tag [87, 83]. This tag can give a B efficiency and purity of $\varepsilon \gtrsim 0.31$, $\Pi \gtrsim 0.94$ [88].

Semi-leptonically Decaying B hadrons: Our Cuts

In order to measure the B energy spectrum we have chosen to work with s.l. B hadrons for the reason that we are able to get a handle, in this topology, on which particles in the event are the B daughters. In a hadronic B decay one has $\approx$ twice as many hadrons from the B, and the selection of B daughters is more difficult [6]. Here we are working with s.l. B hadrons and will want to isolate the Weak B decay,

---

[5] At the SLD the IP in a given event is determined by finding the location of the best fit to the origin of tracks in hadronic events. This is done in batches of ≈ 30 Z^0s. Thus the IP in a particular event is the same over those 30 events.

Table 4.3: Criteria for tracks to be vertexed.

Comment	variable	cut
$p_\perp$ w.r.t. beam	p_T	> 0.150 GeV
Track $\vec{p}$	$\vec{p}$	$0.150 < \vec{p} < 55.0$ GeV
r Imp. Param.	R_{imp}	< 1.0 cm
z Imp. Param.	z_{imp}	< 1.0 cm
Norm'd. 3D Imp. Param.	B_{NORM}	> 1.0
Direction w.r.t. beam	$\lvert\cos\theta_{track,beam}\rvert$	< 0.70
# of CDC hits	N_{HITS}	≥ 40
CDC drift time χ^2/dof	χ^2_R	< 5
CDC fit χ^2/dof	χ^2_{LINK}	< 10

$b \rightarrow \nu lc$, from the D[6] decay. For us, this means it is necessary to find a 2-prong vertex, form the resultant momentum, and attach this to the already-found lepton. We need first to impose track cuts for all the candidate tracks from which we wish to find a two-prong vertex. See table 4.3.

The second step in the vertex finding is to put all candidate track pairs into the vertex finding algorithm, and then require the properties of that vertex in table 4.4. As usual we assume all particles have the mass of a π.

Figure 4.3 shows the histograms of a few of these quantities for "Real" and "Fake" vertices in the MC and where the above cuts sit on them. "Real" means the two candidate tracks really do come from a D – perhaps via a $D^{*(*)}$ and/or a wide resonance like a ρ or K^* – while "Fake" means one or both of the two tracks are not from the D. The MC tells us that 90% of the vertices are in fact "Real." Since we are using all possible B hadrons, such things as $\Lambda_b \rightarrow \Lambda_c l\bar{\nu}_l$ and $B^\circ_s \rightarrow D^\circ_s l\bar{\nu}_l$ are "Real."

Figure 4.4 shows four of the MC vertex quality variables, described in table 4.4, histogrammed and normalized to the total number of entries in the plot, and overlayed with the same variable from the data. At the bottom of the plot is the histogram of the number of prongs in the vertices for MC and data. It is possible to produce three-prong vertices by finding two separate two-prong vertices which share a common

[6] By which we mean, generically, the hadron formed by the c and the spectator light quark(s) of the B. See figure 4.1.

Table 4.4: Criteria for D vertices to be kept: vertex quality variables.

Comment	variable	cut
Vertex χ^2	χ^2	< 5
Vertex mass	m_D	$0.3 < m_D < 1.9$ GeV
B mass	m_B	$0 < m_B < 4.5$ GeV
D-IP Dist. · jet	$\vec{r}_{D-IP} \cdot \vec{j}$	> 0.05 cm
Norm'd. by its error	$\vec{r}_{D-IP} \cdot \vec{j}/\delta$	> 1.0
D vtx-l doca	$d_{(D,l)_{doca}}$	< 0.012 cm
$\pi\pi$ doca	$d_{(\pi,\pi)_{doca}}$	< 0.012 cm
D-B sep. · D direc'n.	$\vec{r}_{D-B} \cdot \hat{P}^D$	> 0.025 cm
Norm'd. by its error	$\vec{r}_{D-B} \cdot \hat{P}^D/\delta$	> 1.0

track. In this instance the decision is made to place the final vertex at the site of the found-vertex whose smallest normalized impact parameter track is bigger than that in the other vertex. Four- and higher-prong vertices are found similarly. Hemispheres with multiple two-prong vertices have all the vertex tracks considered to be from one effective spot – the site of the vertex as chosen above. However, figure 4.4 shows that four-prong and higher vertices are very seldom found.

Before stampeding into a discussion of the purity and efficiency of the vertexing in combination with the lepton tag it might be worth a few sentences to explain the method of lepton ($l = e, \mu$) identification. Muon identification proceeds by looking for hits in the WIC strips that are consistent with a fully penetrating track in the CDC. Electrons are identified during the reconstruction process (section 4.2) by extrapolating CDC tracks out to the LAC and examining properties of the LAC hits around the extrapolated track. The ratio of the energies in the EM1 layer to the EM2 layer in the LAC must be consistent with an e^- having the momentum of this CDC track. There must be no HAD2 energy and HAD1 must be small, where HAD1(2) is the front(back) layer of the hadronic section of the LAC. Electrons and muons are identified with greater or lesser certainty depending on how well they satisfy the above requirements.

Now we make use of the lepton. It may be demonstrated that simply requiring

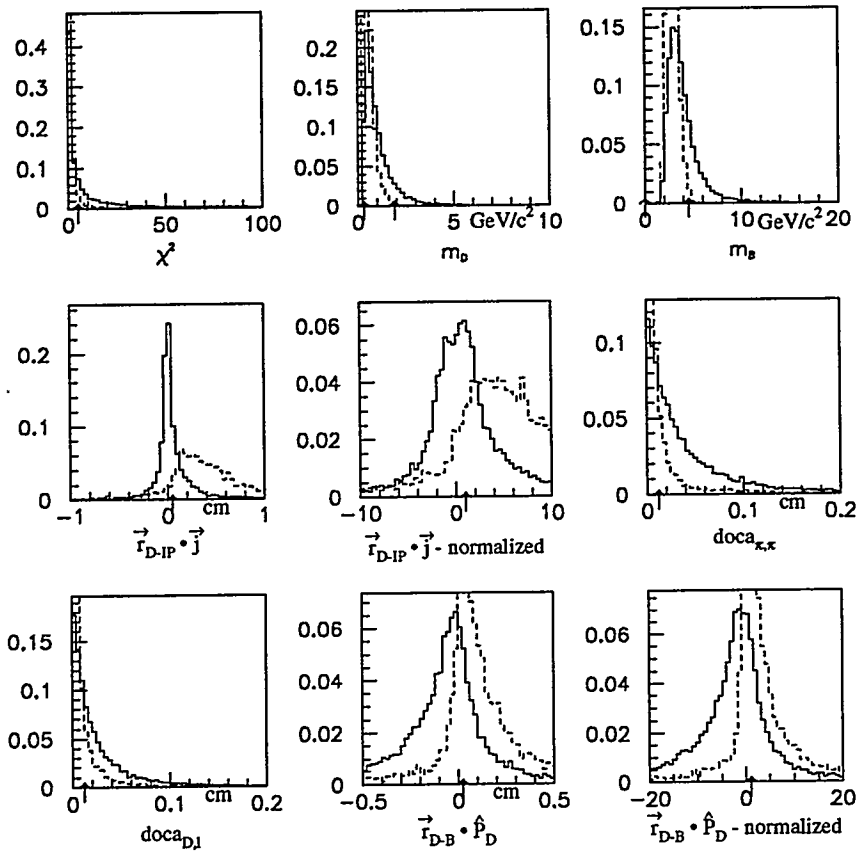

Figure 4.3: Shown are the nine variables that characterize the quality of vertices formed by all pairs of candidate tracks. Cuts shown by the arrows are described in the text. The solid lines represent "Fake" vertices, while the dashed lines represent "Real" vertices.

that there exists a lepton which has a large value of $|\vec{p}|$ and $p_\perp$ with respect to the jet[7] to which it's associated serves well as a s.l. B tag. Figure 4.6 shows the underlying event flavor (before the effect of vertexing) as a function of $|\vec{p}|$ and $p_\perp$ cut values, separately, in events where a lepton (in particular, an electron here) has been found, demonstrating the usefulness of these cuts in tagging B hadrons. Figure 4.7 shows

[7] See section 2.7 for a definition of jets and a discussion of the choice of jet-finding algorithm and y_c.

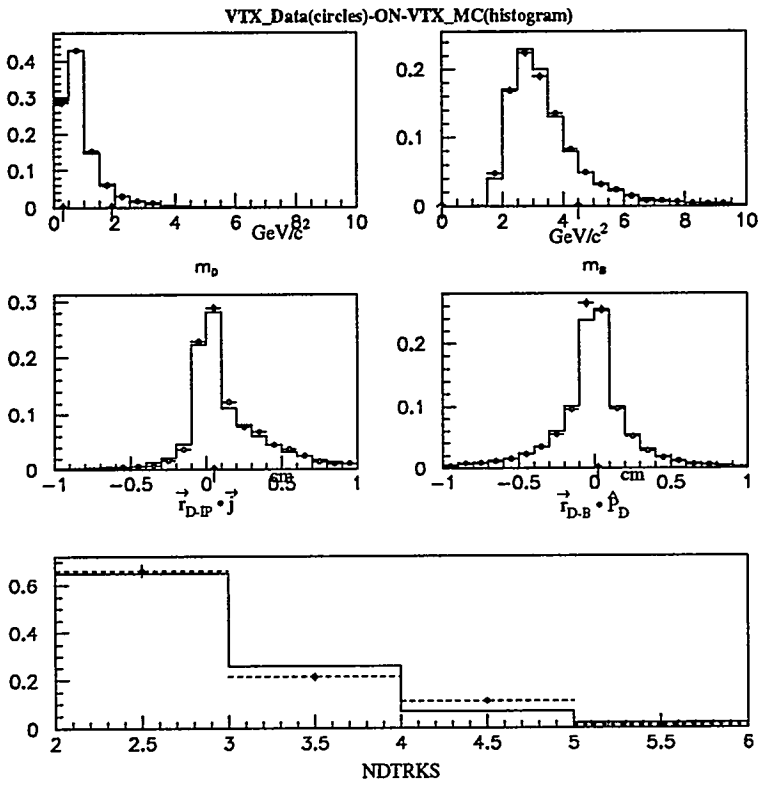

Figure 4.4: Data-MC comparison of four of the vertexing quantities – before cuts – in figure 4.3. At the bottom is the post-cuts number of prongs, NDTRKS.

the s.l. B efficiency-purity graph that results from cutting on the $p_\perp$ of the lepton with respect to the jet to which it's associated. We require in this analysis that the lepton have $p_\perp \geq 1.0$ GeV.

4.1.4 Final Event Counts

To summarize, the final cuts made on the hadronic Z^0 sample require a μ or e with at least 1.0 GeV perpendicular to the closest jet, and a vertex found in that same hemisphere for events in which $N_{jet} = 2, 4, 5 \ldots$, and in that same jet for events in which $N_{jet} = 3$. The number of events remaining in the MC (data) after this selection is 1918 (504), from the original $\approx$ 450,000 (150,000) Z^0s :

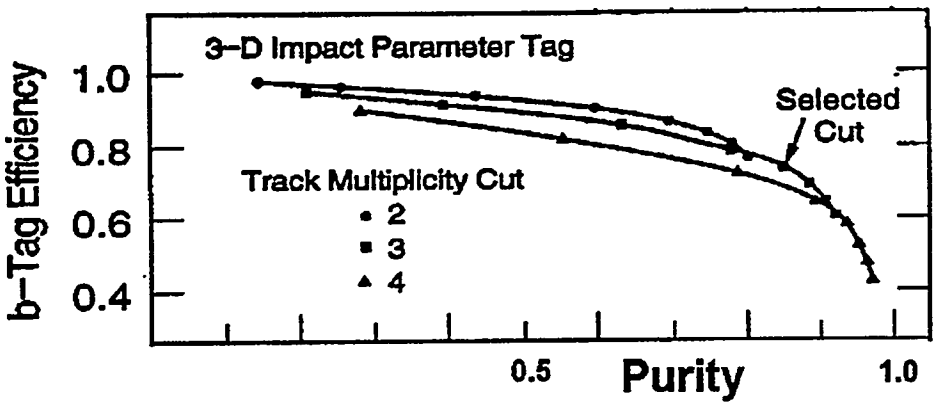

Figure 4.5: The generically-used 3-d impact parameter significance cut for tagging B hadrons [83]. The arrrow shows typical required values of the minimum number of tracks and the minimum displacement from the IP of those tracks (in units of the error on that displacement,$\frac{\sigma}{\delta_\sigma} > d$).

The overall hemisphere event efficiency and purity are 1.5% and 84.5%, respectively. From MC the background and signal composition are shown in table 4.5, showing that this means that 84.5% of the time the lepton traces back to the B, in the way desired. In algorithms in which higher purities and efficiencies are quoted, one should take care to note whether the denominators are both with reference to *semi-leptonic* B hadrons, or just any old B hadrons, and if the purity and efficiency are with respect to all s.l. B hadrons in the hemisphere and not necessarily just those in the acceptance of the detector. Also notice that there may in fact exist s.l. B hadrons in the hemispheres not labeled pure in this analysis due to the fact that the tagged lepton does not trace back to a B (we did not find or mis-ID'ed the lepton). These can be points of discrepancy when comparing tag performances. After requiring the D vertex it is necessary to explore the biasing effect of the tag. Figure 4.8 shows that the vertexing cuts are, in fact, biasing. One can check that stiffening the lepton $p_\perp$ cut does not make this matter worse. The bias will be corrected in the overall efficiency correction.

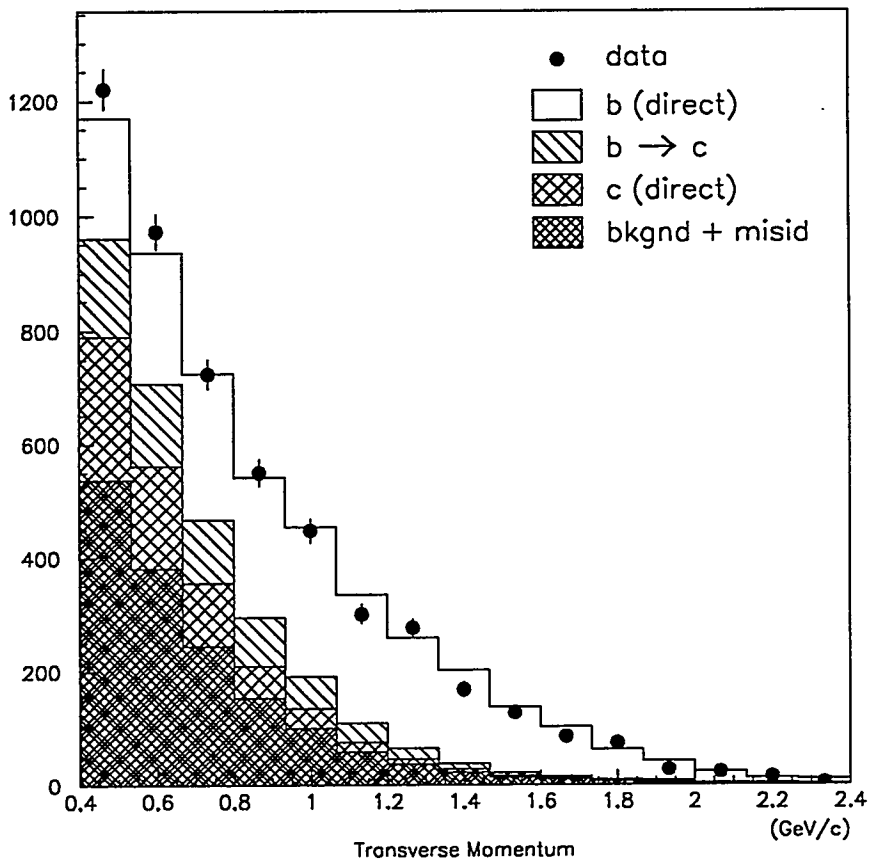

Figure 4.6: Plot [89] of underlying event flavor as a function of a lepton's $p_\perp$ with respect to the closest jet – for $|\vec{p}| > 4.0$ GeV/c. One sees from this that at large $p_\perp$ the leptons are mainly "direct," *i.e.* $b \to c l \nu_l$.

4.1.5 Unused, Alternative Tags

We explore in this section the efficacy of other B and s.l. B tags which have been used in similar analyses. This analysis in the end will not use the tags mentioned in this section.

Impact Parameter Tags and Mixed Tags

One begins by examining the ability of the significant impact parameter tag to find s.l. B hadrons in a particular hemisphere. It is worthwhile (for reasons of bias reduction) to examine the hemispheres in every event only if there exists a lepton

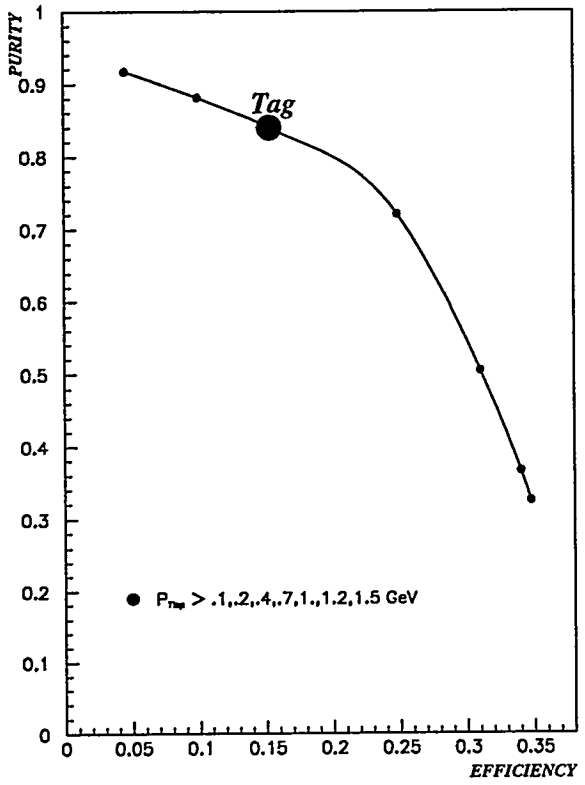

Figure 4.7: Shown are the purity and efficiency of the lepton $p_\perp$ tag we employ to tag semi-leptonically decaying B hadrons. The point labeled "Tag" $(\varepsilon, \Pi = .153, .84)$ is the one used here. The tag severity increases from lower right to upper left.

in the opposite hemisphere. We will want to use the lepton later, and this requirement comes only at a cost in efficiency, with no effect on the purity (in principle). Figure 4.9 will illustrate the reasons for which all the tags in this subsection are not used. The bottom "family" of two $\Pi - \varepsilon$ curves is similar to the families of curves described above in the discussion of significant impact parameter tagging, but for a sample of s.l. B hadrons. Compared to figure 4.5 one sees that the purities are unacceptable. It should be stated clearly here that the purity in figure 4.7 means fraction of all the events found in the tag of B hadrons that decayed *semi-leptonically.* In figure 4.5 only the numerator is different. The numerator in figure 4.5 is with respect to *all* B hadrons. We see that the low purity of the tag shown in figure 4.9

Table 4.5: Leptons in tagged events ($P_{T_l} > 1.0$ GeV) with 2+ prong Vertexing.

l origin	% of events	Evt. flavor	% Bgd.
$b \to \overline{\nu} l c$	84.5		
$c \to \overline{\nu} l X$	0.8		
$b \to \overline{\nu} l c \to \overline{\nu} l X$	4.5		
Other ls	2.0	uds	9.7
		$c\bar{c}$	9.7
		$b\bar{b}$	80.6
misID ls	8.1	uds	16.4
		$c\bar{c}$	14.5
		$b\bar{b}$	69.

to find s.l. B hadrons is consistent with the branching ratio of B hadrons to decay semi-leptonically, which is $\approx 11\%$. In other words, the significant impact parameter tag leaves us with a relatively pure B sample, but only 11% of those are what we really want here.

Two other tags were explored but not used. In the first, the goal is to apply the $\frac{\sigma}{\delta_\sigma} > d$ tag in the hemisphere opposite to the hemisphere in which a lepton has been identified, and slowly turn up the required value of the lepton's $p_\perp$. We call this the mixed tag. Figure 4.9 shows the results of this mixed-tag effort. One gets a better purity for a given efficiency by merely requiring larger and larger values of $p_\perp$, as compared to stiffening the $\frac{\sigma}{\delta_\sigma} > d$ requirement. Hence, the mixed tag is abandoned.

Another s.l. B tag that is commonly used is one which makes an "elliptical cut" using a lepton, *i.e.*

$$(\mathrm{p}/18.0)^2 + (p_\perp/1.1)^2 > 1.0. \tag{4.1}$$

From figure 4.9 this tag has a lower purity for a given efficiency. We do not use it here.

Alternative Vertexing

Certainly, the 2-prong vertexing scheme used here is not the only one in existence. There are other ideas, which we explore here, but do not use in the end. The most note-worthy alternative vertexing scheme at SLD is Dave Jackson's topological vertexing algorithm [90], known as ZVTOP, which defines vertices as regions in space

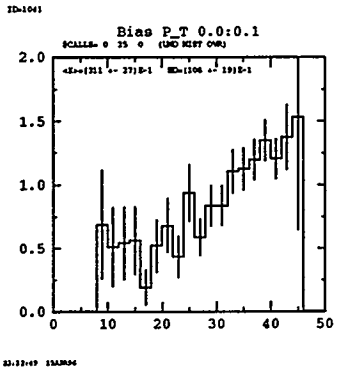

Figure 4.8: This is the normalized, binned MC E_B before vertex cuts divided by the same quantity bin-by-bin post-vertex cuts. There is no minimum lepton $p_\perp$ cut. (The ratty statistics here are due to the fact that this plot comes from an analysis of only about $\frac{1}{5}$ of the MC. The trend remains when the plot includes all the MC.) This shows the vertexing by itself selects preferentially high energy B hadrons. This will be accounted for with an acceptance correction.

where track probability "tubes," whose radii are related to the transverse errors on the track measurement, have significant overlap. In this way one can seek out displaced vertices and tag B hadrons in some applications with 25% efficiency and upwards of 95% purity.

This analysis sought to implement ZVTOP in a not-necessarily-optimized fashion, wherein all good tracks identified by the requirements in table 4.3, not including the lepton (as before), were input to the algorithm. Secondary vertices were found and two track candidates only – even though ZVTOP often finds higher-prong vertex candidates – were analyzed. This was done for the reason of categorizing "Fakes" and "Reals," in the same way as was done above for the 2+prong vertexing technique. Higher-prong vertices are kept, however, if they pass the criteria laid down for the 2−prong vertices, as before.

Cuts were placed on only four of the vertex quality variables listed in table 4.4, but were chosen so as to give an 88% "Real" vertex rate, which is to be compared to 90%, the "Real" rate from the 2+prong technique. The number of MC events that survive the cuts in this technique is $\approx$ 1580 compared to about 30% more than

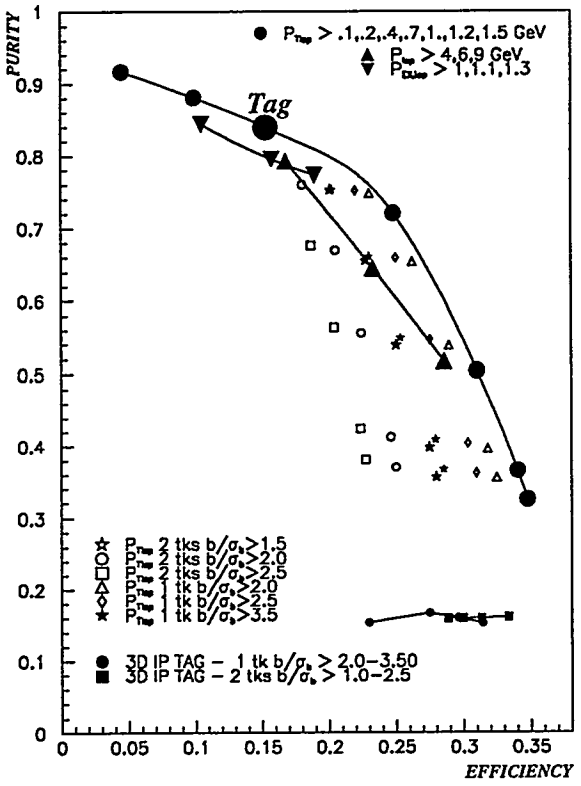

Figure 4.9: Shown are alternative tags to the lepton $p_\perp$ tag compared to the lepton $p_\perp$ tag. The bottom two curves use the significant impact parameter tag. The points unconnected by any lines are the mixed-tags, for a given lepton $p_\perp$, as described in the text. The upper three curves use cuts on the lepton momentum and transverse momentum with respect to the jet to which we associate it, and a combination (the "elliptical cut"). All of these efforts are seen to produce lower purities for a given efficiency in comparison to the lepton $p_\perp$ tag. They are thus abandoned and we stick with the lepton $p_\perp$ cut in this analysis indicated here by the point marked "Tag." In all cases the tag severity increases from lower right to upper left.

this in the 2+prong method. In an effort to get the efficiency up, the strategy was broadened to include the lepton in the vertexing if excluding it failed to produce a vertex. This had the effect of producing 180 more events.

One may make a ε–p curve similar to that for the 2+prong tag and demonstrate the lower purity at a given efficiency for the topological vertexing approach. That figure is not shown here. This approach, with or without using the lepton in the

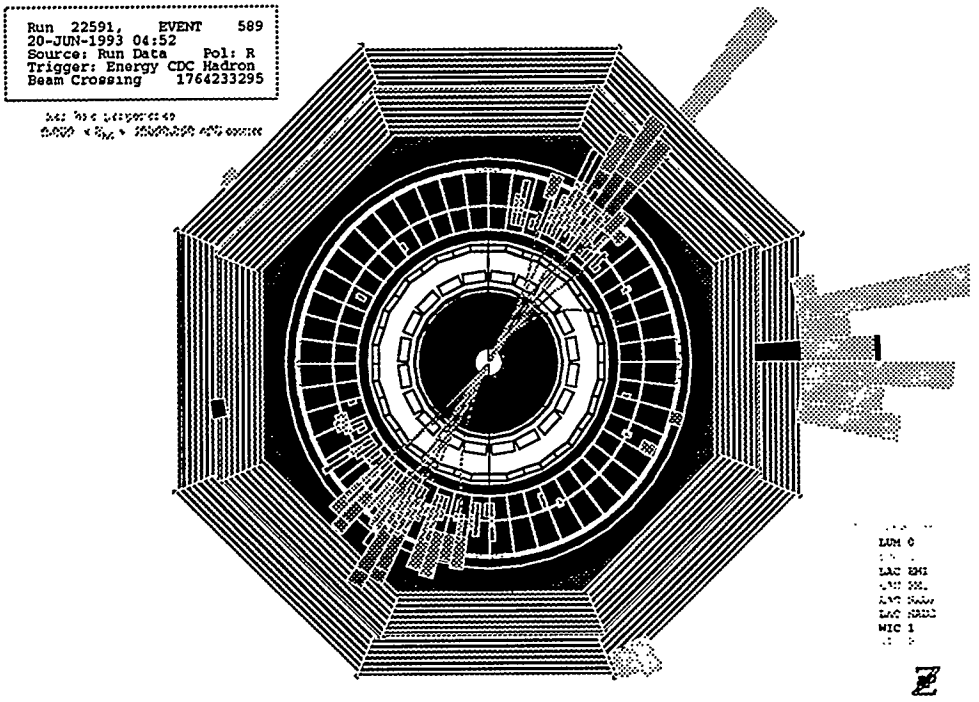

Figure 4.10: A typical 2-jet event, showing tracks and clusters and all detector subsystems. Cluster sizes are in logarithmic proportion to the energy in them.

vertexing, was abandoned and not applied to the data.

4.1.6 Event Pictures

After the lepton and vertex cuts the event selection is complete. An ordinary "2-jet" Z^0 data event picture is shown in figure 4.10. A rather typical s.l. B data event from the final sample, which passes all lepton and vertex cuts, is shown (on the last page of this chapter) in figure 4.21.

4.2 Reconstruction – Specifically, in the LAC

As mentioned already, all events which make it through the PASS1 filter are reconstructed. It is the output of this process from which the physics-analyzable data comes. This is also true of events simulated in the SLD Monte Carlo *farm*. There, after the particles are generated, decayed and swum through the detector one is left

with a "lit-up" detector, on which trigger decisions are made – just as one has in the data. By now, at the reconstruction stage, the MC is as close as it is ever going to get to representing the data, because, additionally, the Random trigger readouts – largely, background SLC muons – from real data have been overlayed on the MC-generated events. The reconstruction process treats data and MC identically.

In the LAC at the raw data or "pre-Recon" stage, one has a catalogue of tower ADC values that have signals above noise thresholds. Those hit towers determined to be "hot" or "dead" are not listed. Additionally here, one has the very early stage of clusters, made by collapsing these hits radially upon each other, layer by layer. All hits that are contiguous in this effective one-layer LAC form one cluster.

It is instructive to list the things that happen here that take the crude clusters and make them into usable ones. For this analysis, it is also worth understanding the procedure that is followed to get tracks in the CDC associated to clusters in the LAC – a procedure that completes one particle's journey through the SLD.

Clustering

Initially, in the data, there are hits – towers in which charge is collected and ADC counts are recorded. Initially in the MC there are not hits, only particles, from which hits must be made. At SLD, MC electromagnetic particles generate their first secondaries as they begin to shower electromagnetically, and the process is quickly halted and the secondaries are "stacked" with the primary to form a net 4-vector. This 4-vector is fed to the fast-shower parametrizer, based on the GFLASH shower parameterization [91] developed by the H1 collaboration, which generates shower radial and longitudinal shapes. MC hit towers are made when the energy density given by the shower shape is integrated over the detector volume which the parametrized shower now spans. Hadronic particles in the MC shower similarly, but they are not stacked first, in contrast to electromagnetic shower-making particles. This treatment of hadronic and electromagnetic showers in the SLD MC is referred to as the Hybrid showering scheme.

In the clustering process, the first thing that is done is to convert ADC counts in hit towers that are over the noise threshold into energy in the *mip* scale. (See section 4.3.2 for a discussion of scales.) These crude clusters are separated by the part of the KAL system they are in: LUM, Endcap LAC and Barrel LAC. And then it quickly gets ugly. The quite-complicated UCLUS [92] algorithm is used to

define clusters around cluster "cores" in such a way that, *e.g.* it is possible to share hits among clusters. Hits which are topologically connected to each core are either shared between the two clusters or thrown into one or the other cluster, *or* the clusters are merged into one cluster, according to the energy "dip" between the two cores. See reference [92] for details. Next, all the tiny clusters ($\lesssim$300 MeV) that have hits adjacent to hits in larger clusters in all layers in which both have hits, are gathered up and merged. Then, the all-important muon cluster-finding routine looks for clusters consistent with being background muon clusters, namely clusters with multiple adjacent towers running parallel to the beam. These clusters are marked, and in fact are not written out in the list of final, refined clusters. And, last, the cluster cleanup is applied, where each cluster satisfying the requirements that it (1) contains at least two hits, (2) has an energy of at least 100 MeV, and (3) has non-zero energy in the EM section is written to the family of banks of final, refined clusters. The energy, location and angular widths of the cluster are recorded, where the widths are RMS energy-weighted widths.

Track-Cluster Association

We care about this topic because, as will become clear in chapter 5, we want to know the B's neutral energy contribution to its total energy[8]. Obviously because neutral particles don't leave tracks in the CDC, this can only be done with the calorimeter. The first thing to do then, is to come up with a procedure to measure the correct amount of neutral energy in a hemisphere (or jet), depending on whether the event is a two-jet event (or a three-jet event).

The second thing to do will be to decide how to apportion some of it to the B. That's the tougher part and will be addressed in chapter 5. What is done is the following. We divide all clusters in a hemisphere (or jet) into the following four categories, with E_{clus} the energy of the cluster in the *mip* scale and E_{clus_H} the energy in the LAC's Hadronic section:

- Unassociated Hadronic: unassociated and $\frac{E_{clus_H}}{E_{clus}} > 0.25$ OR $E_{clus_H} > 250$ MeV
- Unassociated Electromagnetic: unassociated and not hadronic, as defined above
- Associated Hadronic: associated and $\frac{E_{clus_H}}{E_{clus}} > 0.25$ OR $E_{clus_H} > 250$ MeV
- Associated Electromagnetic: associated and is not hadronic, as defined above

[8] As will be true everywhere, unless explicitly mentioned, νs are not considered in neutral energy, as they are invisible to any detector.

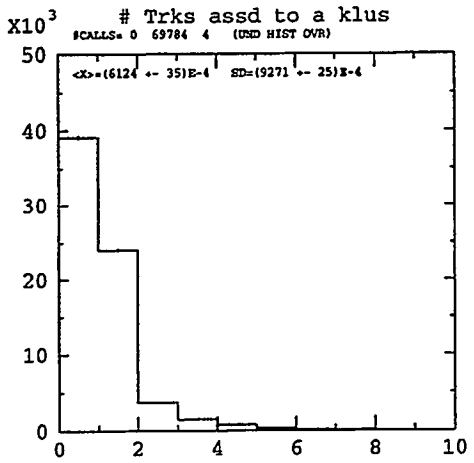

Figure 4.11: MC: Number of clusters associated to a given track, for all track $|\vec{p}|$.

"Association" means a cluster has a track pointing to it. Tracks get associated to clusters and vice-versa when clusters sit within 4σ of a track, where σ is defined to be the error on the track pointing (which is negligible, generally) summed in quadrature with the two angular widths of the cluster. The rules for the official SLD track-cluster association, which is employed here, are that one track may point to only one cluster, but one cluster may be associated with multiple tracks. However, figure 4.11 shows that generally a cluster has, at most, one track associated to it. It should be true that all tracks in the CDC are associated to a cluster in the LAC, and figure 4.12 shows this is the case for almost the whole momentum range of tracks. Since the first two bins ($0 - 2$ GeV, see figure 4.14(a)) in fact, contain most of the tracks in the hemisphere, and we see that that's where the tracks are most poorly associated, this point must be investigated. There can be a few reasons why these tracks don't get matched to clusters: (1) they range out before hitting the LAC, (2) they make it to the LAC, but don't shower, or (3) the MC showering is producing clusters for these low momentum particles, but the cluster cleanup (mentioned above in section 4.2) is wiping these clusters out.

The reality (at least in the MC, which is the only place to test any of these hypotheses) is some combination of the first two of these effects. One can show that point (3) above is not a big effect.

Figure 4.13 is identical to figure 4.12, except that it is for particles which shower.

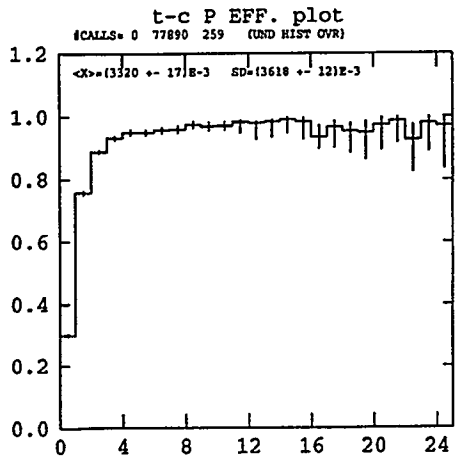

Figure 4.12: MC: Efficiency plot for association of a track to a cluster, binned in track $|\vec{p}|$ (GeV/c), showing the problem of tracks not getting matched to clusters at low $|\vec{p}|$.

This means they reach the LAC *and* they shower. Notice figure 4.13 shows an improvement in the low momenta bins. Figure 4.14 shows the tracks' momenta spectra both before and after the requirement that they showered in the LAC. These plots demonstrate that about a little more than half the first bin's problem in figure 4.12 is explained by tracks that simply don't make it to the LAC with enough energy to shower (if they make it at all). The MC reveals that the other half of the first bin's problem is explained by particles which make it to the LAC without enough energy left to shower, even though the MC sent the cluster on to the cluster parametrizer and claimed it showered. Thus categories (1) and (2) above are the explanations for the lack of association at low track momentum. This is reasonable for 1 GeV particles. Figure 4.15 shows an $r - |z|$ plot of the coordinate of the termination point of the particles that don't shower. We're left with an "X-ray" of the SLD (compare to figure 3.7).

Unassociated Electromagnetic clusters go immediately into the neutral energy sum with the EM scale. Unassociated Hadronic clusters are discarded for reasons to be discussed in a few sentences. Associated clusters first have their charged energy (formed as if they were $\pi^{\pm}$s) subtracted from them and – if the remainder is more than 1σ greater (on the calorimeter's electromagnetic resolution scale) than what one would

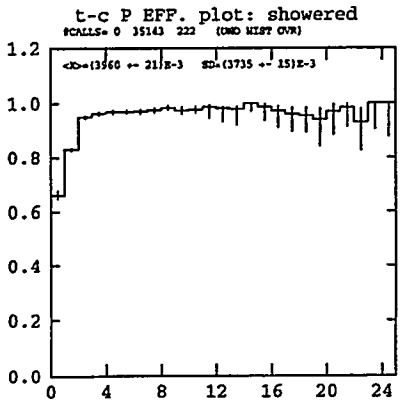

Figure 4.13: MC: Efficiency plot for association of a track to a cluster for tracks that make it to the LAC *and* shower – again binned in track $|\vec{p}|$ (GeV/c). This shows improvement at low track $|\vec{p}|$, but clearly is not the full solution to the problem.

get from the usual stochastic fluctuations from an electron/photon or hadron, then that remainder may be considered for inclusion in the neutral energy sum too – with the appropriate scale (see section 4.3.2). The justification for including associated clusters in the neutral energy sum is that often a charged and neutral particle will end up in the same cluster in the LAC, and so we will want to try to include the contribution of the neutral particle to this cluster. Figure 4.16, which is from MC *as are all the plots in this track-clustering section*[9], shows the particle content of the four different types of clusters. Immediately, one sees the justification for the omission of the Unassociated Hadronic clusters: $\pi^{\pm}$s dominate. A further inspection of these $\pi^{\pm}$s reveals that they are almost always decay products produced by the swimmer that don't get a good chance to form a track in the CDC. This is also the primary source of the $\pi^{\pm}$s in the Unassociated Electromagnetic clusters. Similarly, one can investigate the electrons in Unassociated Electromagnetic clusters and see that they come entirely from the swimmer – γ conversion: $\gamma \rightarrow e^{-}e^{+}$, to be precise.

Since it is true that neutral and charged particles convert into each other (*e.g.*

[9] The Data track-clustering performance is quite similar to the MC, and in the places, which are coming in a couple paragraphs, where plots that are MC dependent are shown, I appeal to section 3.3.6.2 for validation that the MC is truly representing what's going on in the data.

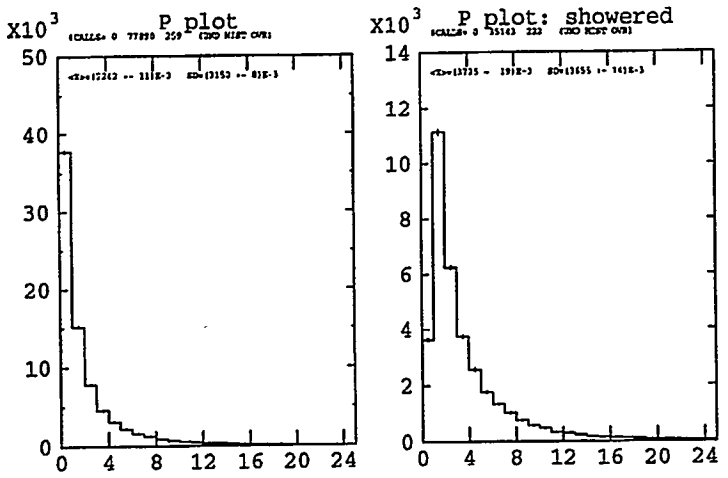

Figure 4.14: MC: $|\vec{p}|$ (GeV/c) of all tracks, before and after the requirement that the particle showers in the LAC. This shows that particles of $|\vec{p}| \lesssim 1$ (GeV/c) rarely make it out to the LAC and shower.

$\gamma \rightarrow e^+e^-$, it is worth asking if (in the MC) sum of the energies of neutral particles which enter the LAC and make clusters is equal to the neutral energy in the event[10]. Figure 4.17 shows the histograms of the MC true neutral energy and of the MC measured neutral energy. The averages shown on the plots and the similarity of the shapes indicate that this method of gathering the neutral energy in an event may be reasonable. Of course, similarity of shapes is not the criteria to be passed for inclusion of a quantity where event-by-event connection with reality is desired. To see, finally, that the decision is reached to omit associated clusters please see section 5.2.

4.3 LAC Energy Scale

4.3.1 LAC Energy Response

There are two main issues to consider when converting ADC hits in clusters into energies: energy response and the appropriate scale. It is necessary to understand the second of these two issues in order to assign the appropriate energy to a cluster, and it will be covered in the next subsection. The first issue involves an understanding

[10] defined here to mean the energy in all neutral, stable particles, ns, γs and K^0_Ls *or* strange particle decay from fragmentation.

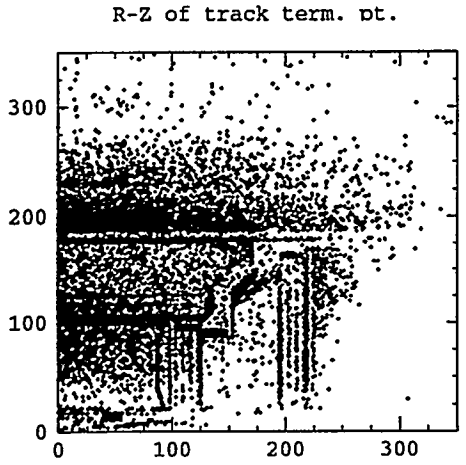

Figure 4.15: MC: An $r - |z|$ plot of the termination point of all particles that do not leave a shower in the LAC. Compare this effective detector X-ray to figure 3.7.

of the uniformity of response of the calorimeter to incident hadrons.

Upon examination of the plot of $|\cos\theta_{thrust}|$ in figure 3.29 one sees that in the range of polar angle $|\cos\theta_{thrust} < 0.7|$ the energy response is fairly uniform, and in the endcap it takes a dive. In itself, this is not necessarily a problem if it is taken into account. One approach [75] to accounting for it which is independent of the MC is to calculate the hadronic cluster multiplication factors in the data (as will be described in the next subsection) that are required so that the cluster sum adds up to m_{Z^0} for many discrete regions of $|\cos\theta_{thrust}|$.

Alternatively, one may proceed from the tower-level data as in reference [78], selecting "good" two-jet events – making sure to include events whose thrust axes span as much of the polar angle as is covered by the calorimeter – and sum up the towers, each multiplied by a factor determined by minimizing the χ^2 on each factor such that the sum gives an event energy of m_{Z^0} over many events. This procedure has the advantage that the calibration is also done entirely from the data, omitting any MC dependence. The disadvantage is the need to keep the hit-level data, which takes up such a huge amount of space that any reasonably sized data sample must be stored on tape, rather than on disk, and computation time becomes large. This

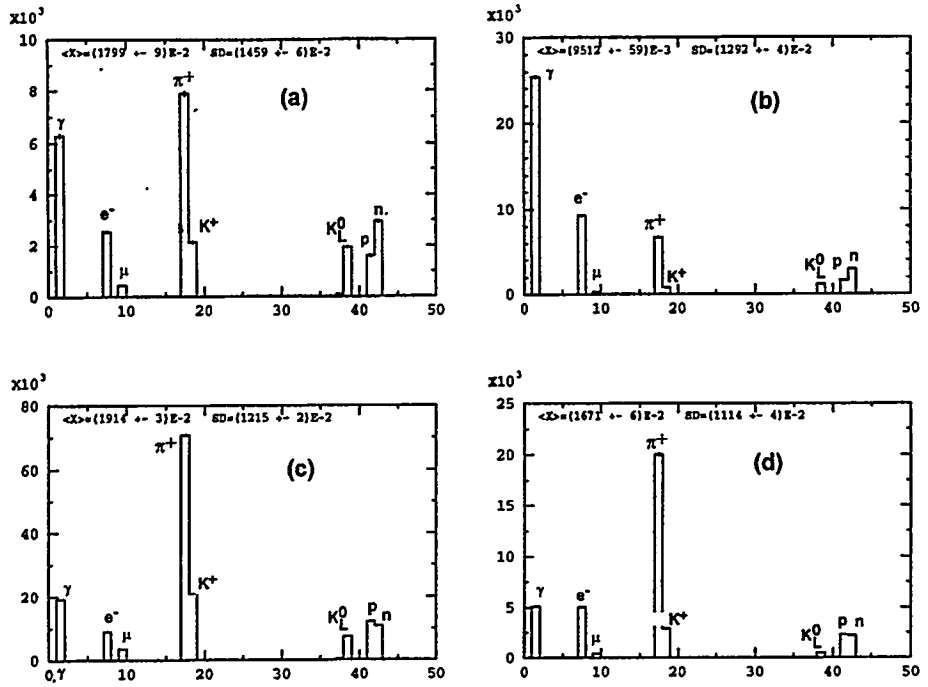

Figure 4.16: The energy-weighted particle populations of the four types of clusters for hadronic events. A particle label symbolizes both the particle and the anti-particle. The vertical scale in a particular plot represents the amount of energy a particular particle deposited in $\approx$ 4500 events. See text for meaning of hadronic and electromagnetic here: (a) Unassociated Hadronic, (b) Unassociated Electromagnetic, (c) Associated Hadronic and (d) Associated Electromagnetic clusters.

approach was tried in this analysis, but found to not be better[11] than the far-less cumbersome alternative, described below.

The alternative to both the above is to use barrel-averaged cluster multiplication factors, but to first scale the observed data cluster energy in a given polar angle bin to the value that, on average, the MC particle responsible in that bin deposits. One immediately encounters a problem: the MC in the endcap does not agree with the data. (See the plot of E_{event} vs. $\cos\theta_{thrust}$ in figure 3.30 and the upper few bins of the plot of $|\cos\theta_{thrust}|$ in figure 3.30). This is a famous [93, 72, 75] discrepancy – one that

[11] mainly because the endcap calorimeter gets very limited use due to our event cut of $|\cos\theta_{thrust}| < 0.71$.

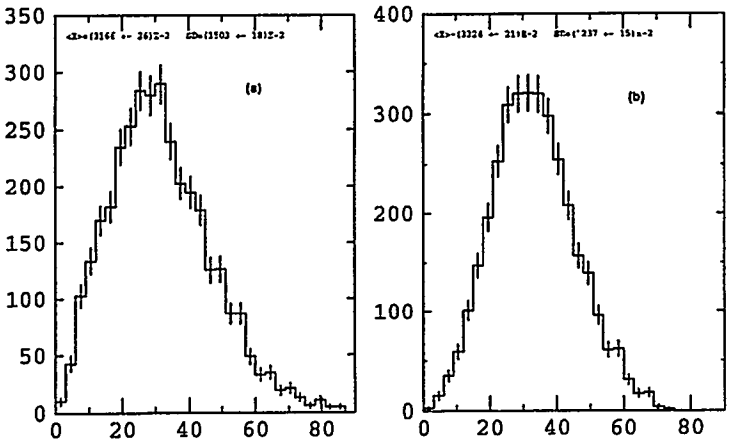

Figure 4.17: MC: (a) The Monte Carlo true E_{Neu} and (b) the reconstructed E_{Neu}, according to the algorithm described.

has only been "solved" by those who care about it[12] by pasting material liberally in the endcap of the GEANT [94] detector simulation. Upon *making* the MC look like the data and dividing the MC generator output by the MC GEANT output, one obtains the relative LAC response – the correction factors to be applied to the data before energy scaling in order to get back the "real" particle (pre-scaled) energy [93] (see figure 4.18). Notice that the Correction factor is uniform and equal to ≈ 1 in the polar angle range we care about for this analysis. The biggest value is in the polar angle region $0.408 \leq |\cos\theta| \leq 0.466$ – the location of the washer separating the central barrel from the end section barrels[13].

4.3.2 Setting the Scale

The response of the LAC to hadronic showers is different than it is to electromagnetic showers, and both are different from the response to minimum ionizing particles. Minimum ionizing particles are the simplest to understand: a particle travels through a tower with a low enough cross section for other processes that it just loses energy by dE/dx according to the value at the minimum of its Bethe-Bloch curve. The

[12] it has not been fully done in the official SLD MC

[13] *However*, this is all a moot point when, soon, we bypass this issue by using only unassociated electromagnetic clusters.

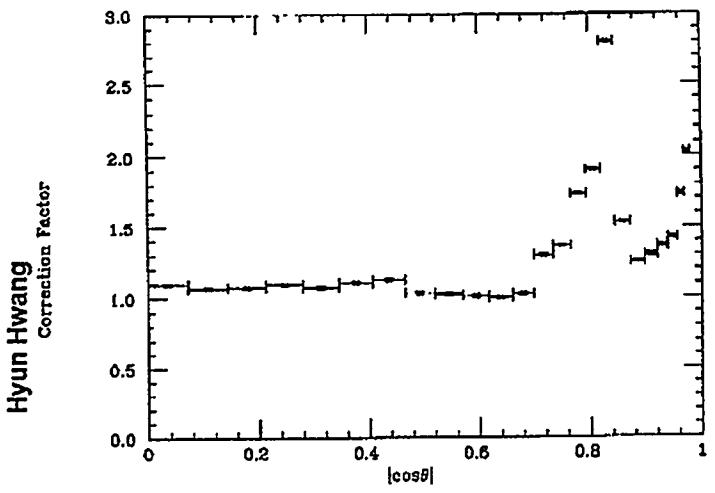

Figure 4.18: The amount by which we multiply the cluster energy as a function of its $|\cos\theta|$ for hadronic clusters. The bin sizes are chosen to match LAC tower boundaries.

charge collected becomes some number of ADC counts that needs to be multiplied by a constant factor to come up with an energy loss in that tower. This is the *mip* scale.

We've already described electromagnetic showers in section 3.2.3. Their ADC counts need to be scaled by another number, a number which is generally given relative to the *mip* scale, called the $\frac{e}{\mu}$ scale.

Hadronic showers begin on average a distance of λ_{int} into the LAC on high-Z material, namely lead. They result from a mixture of reactions, dominated by multiple particle production, including π^0s which decay to two photons, and thus hadronic showers include an electromagnetic component [95]. For an *uncompensating* calorimeter, as we have at SLD, we expect to have to divide our *mip*-scale energy by a smaller number than 0.67 (or multiply by a bigger number than 1.50) to arrive at $\frac{\pi}{\mu}$. The next two short sections deal with the two ways in which $\frac{e}{\mu}$ and $\frac{\pi}{\mu}$ can be measured.

$\frac{e}{\mu}$ Determination

One way to extract $\frac{e}{\mu}$ is to plot the $\gamma\gamma$ invariant mass for all pairs of γs in hadronic

events, as π^0s are plentiful there[14]. This is done in figure 4.19. The requirements on the photon-candidate clusters are the following:

- The energy in the electromagnetic section of the calorimeter must constitute at least 93% of the cluster's energy.
- The number of hits that comprise the cluster must satisfy $4 < N_{hits} < 200$.
- The sum of the energy in the three most energetic hits in the cluster must comprise at least 80% of the the cluster's energy.
- The cluster must not be associated to a charged track.

It is further required that the two photon clusters being combined must make an angle of less than 60°.

The invariant mass for two massless objects (photons here) takes the particularly simple form

$$p^2 = m^2_{\gamma\gamma} = 2(E_{cl_1}/\frac{e}{\mu})(E_{cl_2}/\frac{e}{\mu})(1 - \hat{p}_{cl_1} \cdot \hat{p}_{cl_2}),$$

where the $\hat{p}$s are unit vectors pointing in the directions of the two photons, as determined by the cluster direction information. It can be seen from figure 4.19 that the value used here, $\frac{e}{\mu} = 0.67$, puts the peak at m_{π^0}.

$\frac{\pi}{\mu}$ Determination

To find the hadronic scale we will simply look at $Z^0 \rightarrow q\bar{q}$ events and force the total energy in these events to be $2E_{beam} = m_{Z^0}$, ignoring the relatively tiny contributions of non-hadrons in these events that originate from the decay of other hadrons. We will ignore the WIC. Thus,

$$E_{vis} = \lambda_{EM} E^{Tot}_{EM} + \lambda_{HAD} E^{Tot}_{HAD} = m_{Z^0}.$$

One can form the equation of a line [75] by dividing by, say, E^{Tot}_{EM}, plotting in the data the left hand side vs. the right hand side, and fitting for the two parameters λ_{EM} and λ_{HAD}, the y-intercept and slope respectively, of the line – with E^{Tot}_{EM} and E^{Tot}_{HAD} in units of the *mip*-scale. This is done for 1993 data in figure 4.20 for both barrel and endcap events, defined by $|\cos\theta_{thrust}| < 0.70$ and $|\cos\theta_{thrust}| > 0.70$, respectively. The fit values for the barrel, which is all we care about here (see section 4.1.3 to be reminded of the event cuts) are $\lambda_{HAD} = 2.910 \pm 0.019$ and $\lambda_{EM} = 2.608 \pm 0.008$.

[14] $\tau_{\pi^0 \rightarrow \gamma\gamma} = 8.4 \times 10^{-17}$ sec

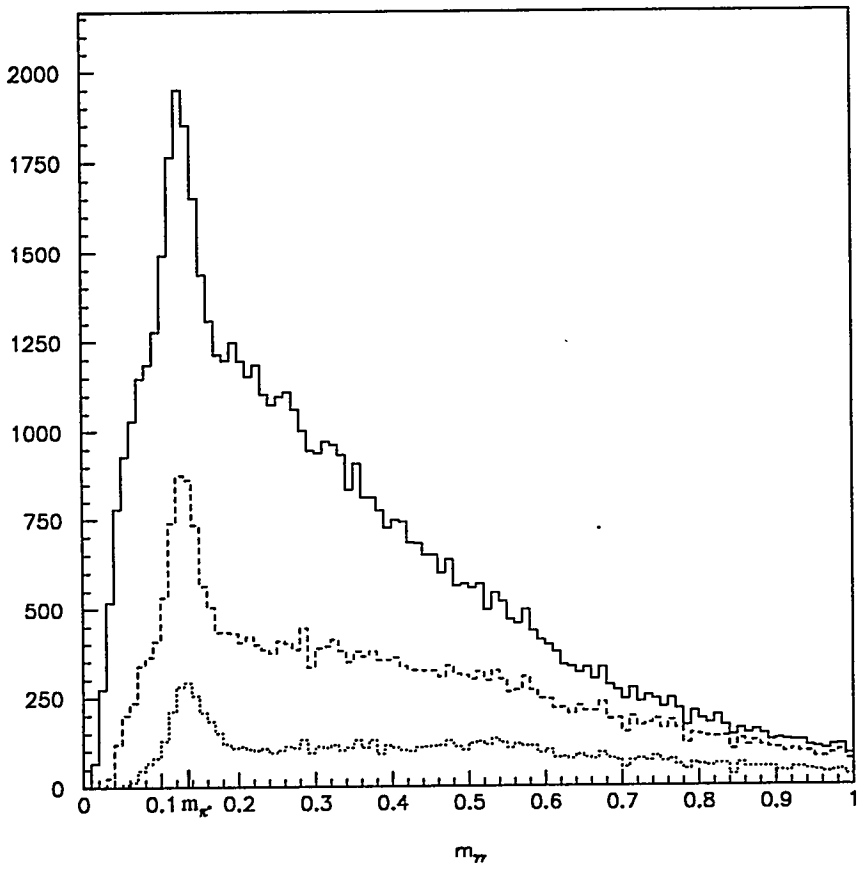

Figure 4.19: The invariant mass of pairs of photons, found and combined as explained in the text. This is 1993 data. The scale is in GeV/c^2, and the mass of the π^0 is indicated. $\frac{e}{\mu} = 0.67$ to get the peaks to fall at m_{π^0}. The solid line requires that the energy (*mip* scale) of each photon, $E_{cl_1,2}$, is greater than 100 MeV, the dashed line requires $E_{cl_1,2} > 400$ MeV and the dotted line requires $E_{cl_1,2} > 700$ MeV.

It is true that depending on how one defines quality clusters, these parameters will change. The 1994 data yield the same values for the λs to within the quoted errors.

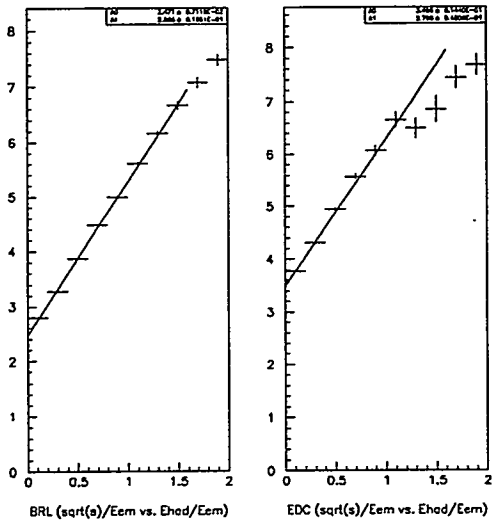

Figure 4.20: Extraction of $\frac{e}{\pi}$. BRL(EDC)means the thrust angle is well-contained in the barrel(endcap) LAC. Notice that the last 2(4) points are omitted from the fit. One can check that it is extremely rare ($\approx$ 2% of good clusters) that the ratio of hadronic energy to electromagnetic energy in a given cluster is as large as 1.5.

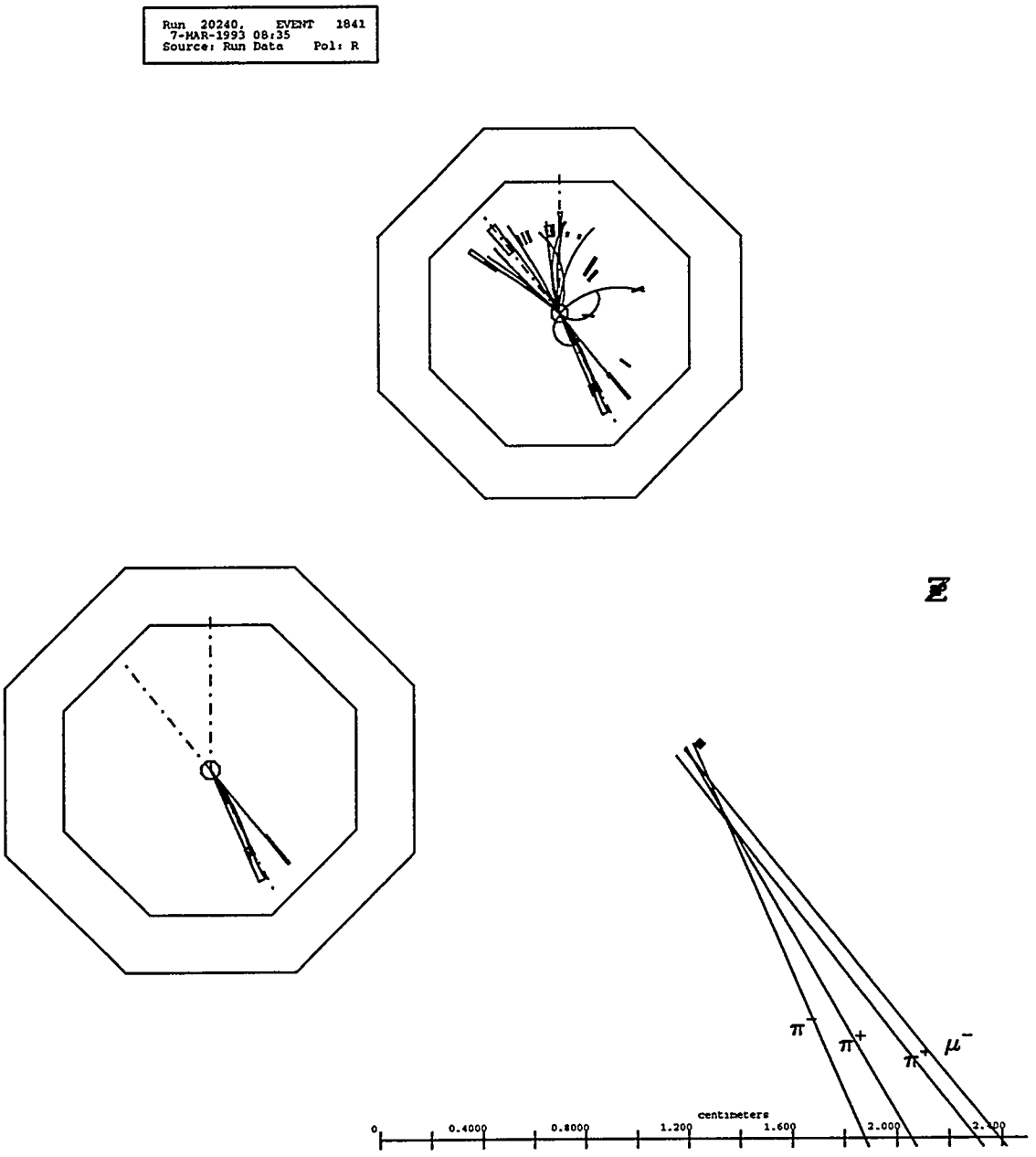

Figure 4.21: Three views of a B $\rightarrow$ D$\mu\overline{\nu}_\mu$ data event: the whole event, the isolated four B decay tracks and two clusters, and the four B tracks zoomed well inside the VXD2, showing the separate B and D vertices. Detector elements shown are the WIC and VXD2 only. The IP is shown in the zoomed-in display. Dashed lines are the (three, in this case) jet axes. The label $\pi^\pm$ means $\pi^\pm$, $K^\pm$, etc. Note also that the tracks are extrapolated back far enough to determine their would-be crossing point with the IP, and are not terminated at the secondary vertex.

Chapter 5

RESULTS

5.1 The Event Sample

From 150,000 Z^0s collected at the SLD, we have extracted a sample of s.l. B hadrons with which to measure the b quark fragmentation function.

The motivation for choosing semi-leptonic events for the measurement is at least two-fold. First, with the lepton, one has one track with which to form the B vertex. The remaining B tracks in the vertex come from the resultant formed by the D vertex tracks, and so in the zeroth order approach the assignment of tracks to the B is straightforward. In hadronic events in principle one must reconstruct both vertices in order to find all the tracks that originate from the B. Second, from MC we learn that the average ratio of non-neutrino neutral B Energy to total B energy in s.l. B hadrons is smaller than in hadronically decaying B hadrons (see figure 5.1). This is a consequence of having no π^0s at the s.l. B decay, as are present in hadronic B decays. And if the B's non-neutrino neutral energy is small, we will make a smaller error in measuring and then attributing some amount of the total hemisphere's non-neutrino neutral energy to the B.

5.2 The Energy Measurement

We will make use of the notation E_B^{True} and E_B^{Rec}, to mean the true and reconstructed B energy, respectively, which have meaning in both the MC and data, even though in the data E_B^{True} is not known to us, as it is in the MC. The goal of the study is in fact to measure E_B^{True} in the data. We will try to be clear when we are speaking of MC and when we are speaking of data if the distinction is important.

The B energy is reconstructed using a partially reconstructed vertex and tracks and clusters in the hemisphere/jet.

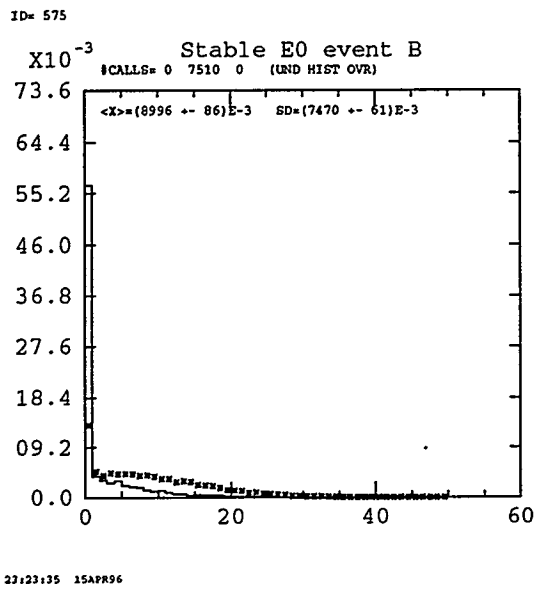

Figure 5.1: MC: E_0 in s.l. B hadrons and all B hadrons. The stars are the all-B sample, and the histogram is the s.l. B hadrons, showing the relative lack of neutral energy in s.l. B decays. The histograms are normalized to the same area.

5.2.1 E_B^{Rec}

One begins by identifying events as described in section 4.1.3. The goal is to form $E_B = E_l + E_\nu + E_D$. Here, as always, B means any B hadron and D means the charmed hadron left after the s.l. B decay. Since the neutrino is invisible to our detector we will invoke energy conservation, $E_\nu = E_{beam/Jet} - (E_l + E_D + E_{frag})$, where $E_{beam/Jet}$ is the energy the b quark carries away from the IP and E_{frag} is the total energy in the *beam/jet* not attributed to the B. For $N_{jets} = 3$, we use E_{Jet}, and for all other values of N_{jets} we use E_{beam}. The reason for this is that in the three jet case it is seen [78, 93] that the underlying parton directions are well-reproduced while the energies are not, and we may accurately re-calculate the jet energies by enforcing $\vec{p}$ conservation, where $\vec{p}$ is the total jet 3-momentum and we take $m_{Jet} = 0$.

The result is

$$E_{Jet_{1,2,3}} = \sqrt{s}\frac{\sin\theta_{23,13,12}}{\sin\theta_{12}+\sin\theta_{13}+\sin\theta_{23}},$$

where the the numbers indicate the particular jet number, and the angles $\theta_{23,12,13}$ are the angles between the two jet axes indicated. The notation is meant to suggest three equations – one for each jet. For all higher jet numbers conservation of 3-momentum does not constrain the energies, and we use the whole hemisphere, $E_{beam} = 45.6$ GeV, as the initial b energy. As usual, we rely on the unfolding matrix, built with the aid of the MC, to make corrections such as the one that may be needed to accommodate the assumption that the incident b energy is 45.6 GeV and all the daughters of the B remain in the hemisphere we choose in higher-than-four-jet events.

Simply then

$$E_B = E_{beam/Jet} - E_{frag}. \tag{5.1}$$

Figure 5.2 shows that this simple-minded application of energy conservation does in fact work. E_{frag} consists of two parts,

$$E_{frag} = E_{neu} + E_{chg}.$$

E_{chg} is evidently the sum of the energy of all charged tracks in the $beam/Jet$ not assigned as the lepton or daughters of the D. E_{neu} is trickier potentially, and we fall back on the discussion beginning on page 94 to decide what to include in it.

Measurement of E_{neu}

First, it should be acknowledged that cluster finding is not an exact science. We clump hits together in a way that seems to reproduce the energy of the responsible particle, but there are ambiguities inherent in splitting and joining that our algorithm must try to resolve (section 4.2). Sometimes it does not work. One obvious thing that can happen is that one cluster can contain more than one particle. Thus, a decision must be made. One may attempt to end-run around the whole clustering procedure by, for example, going back a step to the hit-level data and including all hits outside of certain-sized windows in the calorimeter, with each window centered around the LAC entry point of the extrapolated track. Such an approach makes sense often in photon (γ) identification applications [78]. Here we want to actually make an energy measurement. Nevertheless, this approach was tried briefly and found

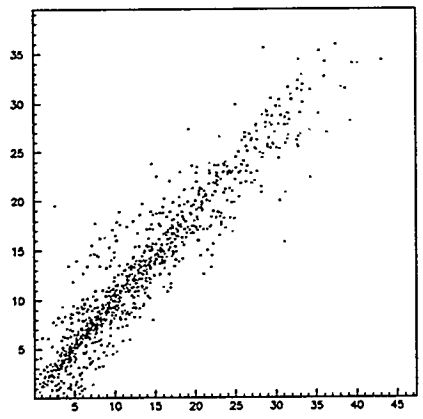

Figure 5.2: MC(2 jet only): $45.6 - E_B$ vs. $E_{chg_{true}} + E_{neu_{true}}$.

to work to some degree, but not so well that it was worth carrying around the huge amount of data this necessitates. And such a procedure is subject to some of the same problems: one will miss hits near tracks that are really slop from a nearby neutral particle. Thus, the decision was made that some sort of clustering is necessary, and an attempt would be made to extract as much of the neutral energy as possible from the SLD calorimeter clusters.

Therefore we categorize calorimeter clusters into four classes: each is either associated or unassociated to a track, and each is either hadronic in character or electromagnetic. It is conceivable that one may extract the energy deposited by neutral particles from each of the four categories. In the discussion of page 94, however, we noted the pollution of $\pi^{\pm}$s in unassociated hadronic clusters. This was sufficient to omit this category. Here we take up the reasons for excluding both types of the associated clusters too.

Remembering first the strategy: subtract the track's energy (using the measured momentum and assuming $m_{\pi^{\pm}}$) from the associated cluster, and if what remains is greater than that which would be expected given the resolution ($15\%/\sqrt{E}$ for electromagnetic clusters, $65\%/\sqrt{E}$ for hadronic clusters) of the calorimeter it should be considered as neutral spill-over into an associated cluster and possibly included. A MC study is required. The middle pair of plots in figure 5.3 shows the recon-

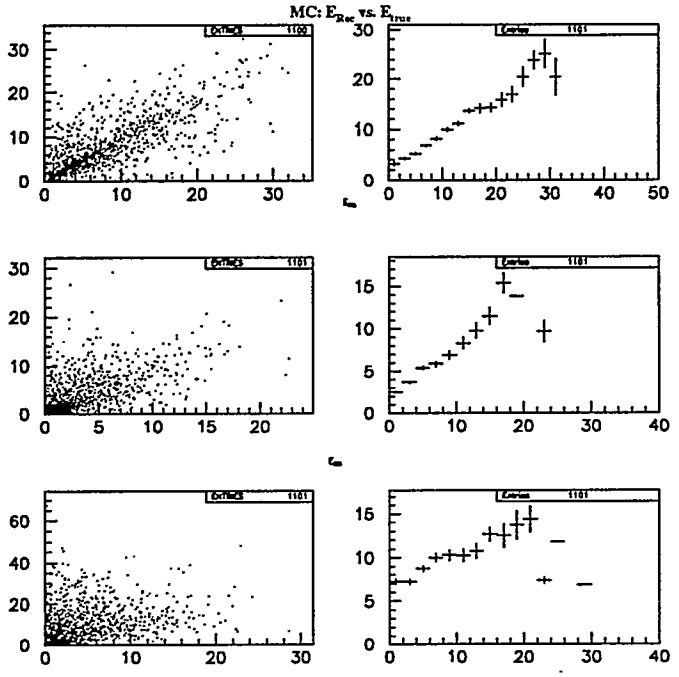

Figure 5.3: MC: The three rows are reconstructed vs. true fragmentation energy for, respectively, charged, neutral(without Associated clusters), neutral(with Associated clusters). The plots in the second column are the binned versions of the corresponding scatter plot in the first column. The lesson here is 'don't use the contribution from the associated clusters.'

structed vs. true neutral energy including this associated-subtracted contribution. The bottom pair is the unassociated contribution and the x-axis there is the true E_γ contribution, since we expect γs to dominate this category. (The corresponding plot for the associated clusters can not be made, since we expect γs,ns, etc. all to contribute. Thus, we make only the middle pair of plots as described. See table 5.1 for the hoped-for contributors to the various categories of clusters.)

In this way all possible neutral, stable particles are considered for inclusion. Inspection of a few event dumps reveals that while sometimes we do catch the desired neutral particles in associated clusters, most of the time we catch far more garbage: *i.e.* charged particles that were produced by decays in flight and thus did not form tracks, low momentum charged tracks that were not associated to their clusters, etc.

Table 5.1: MC: cluster type and hoped-for energy in them.

	Unassociated	Associated
EM	$E_{true} = E_\gamma$	$E_{true} = E_\gamma + E_{n,K^0_L}$
HAD	$E_{true} = E_{n,K^0_L}$	$E_{true} = E_{n,K^0_L}$

The only question that remains is: does the energy in unassociated electromagnetic clusters maintain a correlation with the true, *total* neutral fragmentation energy, E_{neu}, rather than just with E_γ in a B event? That is the correlation of interest in the end. The top two plots in figure 5.4 reveal that it does. This is a statement that γs (mainly from π^0s) make up the great majority of all neutral particles and do not usually slop over into the associated clusters. We plot the inverse of this correlation, since after all we have in the data the reconstructed energy, from which we correct to the neutral energy. That is shown at the bottom of figure 5.4 along with the 2^{nd} order polynomial fit to it. That correction is the one used in the data, and the error on the fit is used to calculate the systematic error contributed by the process of neutral energy reconstruction. One might wonder if the tracking acceptance or the previously-referred-to degradation in the endcap calorimeter leads to a dependence in our energy reconstruction on $\cos\theta_{thrust}$. Figure 5.5 shows the binned scatter plots as a function of this quantity, demonstrating in particular that the fit variation is within the error range already considered in the neutral fragmentation energy correlation. The charged fragmentation energy has little variation as well.

This whole neutral energy assignment, clearly is a somewhat-shady business. We are in fact, relying on the B decay model in the MC to give a correct description of the neutral energy. We would like not to do that, but there is little alternative, given that, unlike the B *tracks* in the drift chamber, we can not precisely infer from the clusters in the calorimeter where they point – even if we had perfect energy resolution. The claim here is that the error on the correlation correction is sufficiently large to accommodate the uncertainty on the B's rather meager neutral energy production.

Measurement of E_{chg}

The charged fragmentation energy, E_{chg}, is merely the energy of all the tracks not associated to the B vertex, summed with $m = m_{\pi^\pm}$. The top pair of plots in figure 5.3 shows the nice correlation in this quantity.

In the end we hope that our reconstructed E_B^{Rec} is correlated with the true E_B.

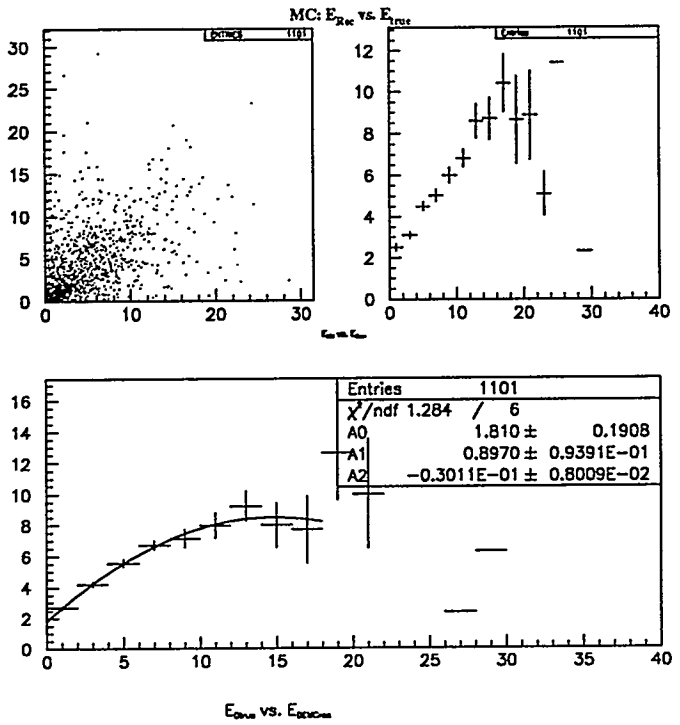

Figure 5.4: MC: The top row is reconstructed vs. true *total* neutral fragmentation energy, defined as in the text. The plot in the second column is the binned version of the scatter plot in the first column, as before. The bottom plot just has the x- and y-axes switched with respect to the top plot, and is fit with a 2^{nd} order polynomial This, finally, is what is used to get the neutral contribution to the fragmentation energy. The systematic error on finding the neutral fragmentation energy comes from varying the parameters of the fit by the errors on them coming from MINUIT [96].

Figure 5.6 is a histogram and a two-gaussian fit of $(E_B^{Rec} - E_B^{True})/E_B^{True}$, (the "residuals") from which we learn the core of the inner gaussian is $\approx 10\%$, and $\approx 96\%$ of the entries come from the inner core[1]. This may be compared to typical "boost" algorithms from B-mixing analyses that quote $\approx 7-8\%$ inner cores with only $\approx 50\%$ of their events in the core[9]. Figure 5.7 shows the reconstructed energy distributions for both data and MC. There is no particular reason they should agree.

[1] A two-gaussian fit is a standard measure of the quality of one's residuals.

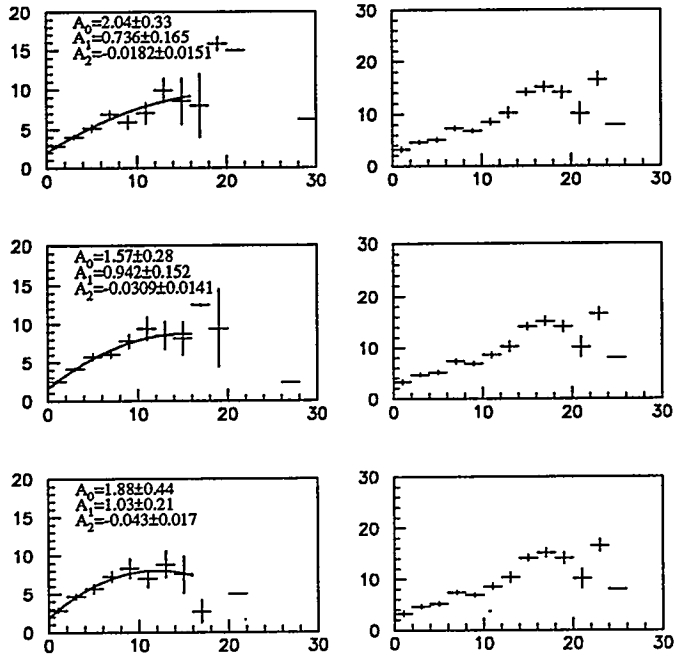

Figure 5.5: MC: Event orientation dependence. The left column is true vs. reconstructed, total neutral fragmentation energy, defined as in the text. The right column is the reconstructed vs. true (backwards compared to the neutral energy plots) charged fragmentation energy. The top row is for $|\cos\theta_{thrust}| < 0.23$, the middle row is $0.23 < |\cos\theta_{thrust}| < 0.46$, and the bottom row $0.46 < |\cos\theta_{thrust}| < 0.71$. And the variation on the charged correlation is minimal. The fit is taken only over the range where there are reasonable statistics. The units are GeV on all axes. One sees that the variation in the fit on the neutral correlation is within that already considered just due to the errors on the correlation over all $\cos\theta_{thrust}$ (see errors on figure 5.4).

5.2.2 E_B^{True}

In the next section we discuss the procedure for mapping E_B^{Rec} into the E_B^{True}. However, before doing that it is necessary to discuss one correction we make to E_B^{True} in the MC. That is this: the JETSET7.4 MC we use makes no accounting for the production of orbitally-excited B** mesons. Heavy Quark Effective Theory predicts four such states [97], and there is now evidence for their existence [98].

One worries about such particles because measuring the b quark fragmentation

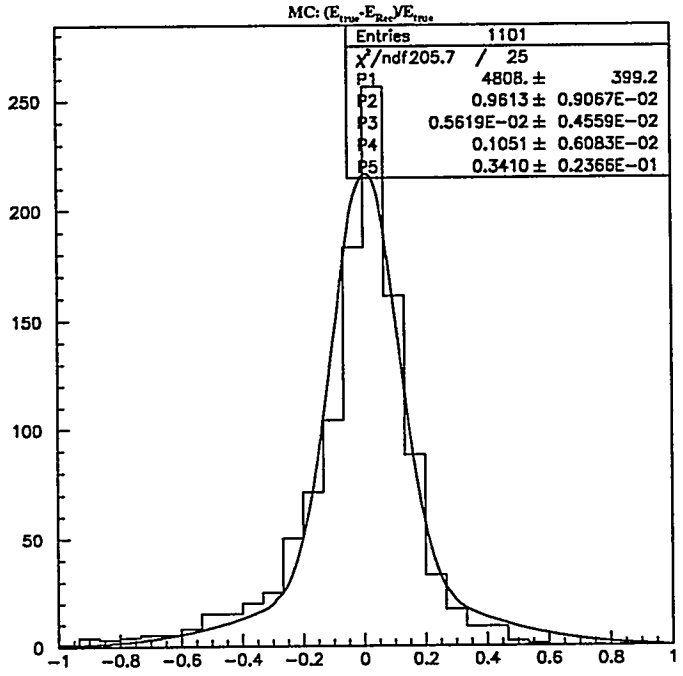

Figure 5.6: MC: Energy residuals calculated for the non-3-jet part of the sample, along with the parameters of a two-gaussian fit, demonstrating that $\sim$ 96% of the events reproduce the true energy with $\sim$ 10% accuracy. The 2-jet sample gives a very comparable fit.

function requires measuring the energy of the initial B in the event, starred or otherwise, and if $B^{**} \rightarrow B\pi^{\pm}$ the algorithm will measure the B energy, and not the desired B^{**} energy. $m_{B^{**}} - m_B \approx 0.51$ GeV, which may be significant, while $m_{B^*} - m_B = 46$ MeV, which we will take to be negligible.

Since these mesons don't exist in the simulation, we will take the simple 2-body decay $B^{**} \rightarrow B\pi^{\pm}$, and calculate $E_{\pi^{\pm}}$ according to [99] $E_{\pi_{\substack{max \\ min}}} = \gamma E^*(1 \pm \beta\beta^*)$, with $E_{\pi_{max}}$ the π's maximum and minimum energy in the lab frame given the B^{**}'s boost γ and the $\pi^{\pm}$'s energy E^* and velocity β^* in the B^{**}'s rest frame. We use the B^{**} production rate $f_{B^{**}} = 20.7 \pm 7\%$ and mass $m_{B^{**}} = 5.7 \pm 0.20$ GeV. We use a MC procedure to assign the $\pi^{\pm}$ an energy between $E_{\pi_{min}}$ and $E_{\pi_{max}}$. We then adjust the MC true energy according to $E_B^{True} \rightarrow E_B^{True} + E_{\pi^{\pm}}$. The indicated variation on $f_{B^{**}}$

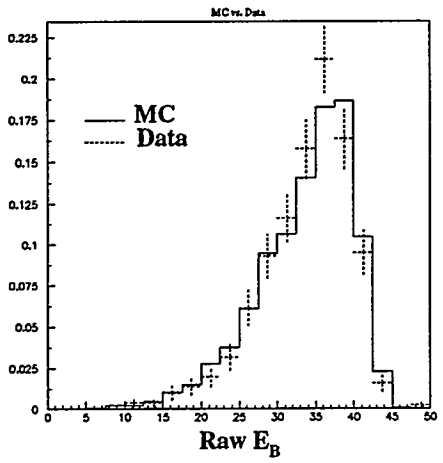

Figure 5.7: MC/Data: Reconstructed E_B for MC and Data. No background, unfolding or acceptance correction has been made. There's no reason these should necessarily agree.

and $m_{B^{**}}$ is that considered for the systematic error calculation.

5.3 Unfolding

We now have a collection of energy measurements. Given that we have ≈ 500 events available we bin the result in 15 bins. The resulting spectrum we call $D_b^{raw}{}_i$, where i is the scaled, binned B energy $i = \texttt{INTEGER}(\frac{E_B^{Recon}}{E_{beam}} \cdot 15)$ and $D_b^{raw}{}_i$ is the number of events in bin i. It is clear that one must subtract the background from this sample, according to some MC study. It should also be clear that in the end we will have to make an acceptance correction – namely, high i events are generally found in the analysis at the expense of low i events, mainly due to the vertexing requirements (see figure 4.8) but also because the jet axis with respect to which we demand a high p_T lepton isn't exactly the same as the B direction.

It is important also to correct for the effect of migration of a B event of true energy E_B^{True} into one of reconstructed energy, E_B^{Rec}. In measurements of quantities like the B lifetime or of mixing parameters this effect is included in the form of one or many gaussians in a log-likelihood function which do(es) just this smearing. Here we don't claim to be extracting a physical parameter from the data and thus we have no likelihood function, and as a result we must characterize our migration

with a *folding* matrix. Further, it is observed that B hadrons of a given energy are measured (reconstructed) to have a different energy that is not described by a simple gaussian smearing from the true energy.

Therefore, to fix the raw data it is necessary to unfold:

$$\mathbf{D}_{\mathbf{true}}^{\mathbf{data}} = \epsilon \cdot \mathbf{E} \cdot \mathbf{B} \cdot \mathbf{D}_{\mathbf{raw}}^{\mathbf{data}} \tag{5.2}$$

$$= \mathbf{M} \cdot \mathbf{D}_{\mathbf{raw}}^{\mathbf{data}} \tag{5.3}$$

with ϵ, $\mathbf{E}$ and $\mathbf{B}$ the diagonal acceptance correction (or efficiency) matrix, the non-diagonal unfolding matrix and the diagonal background correction matrix, respectively. The $\mathbf{M}$ is the product of the three matrices. We alternately use index notation, *i.e.* $D_{raw\,i}^{data}$, and matrix notation, $\mathbf{D}_{\mathbf{raw}}^{\mathbf{data}}$. We obtain ϵ and $\mathbf{B}$ from the "default" MC by just comparing the post-cuts distribution to the pre-cuts distribution and the post-cuts signal to background distributions, respectively. More on these matrices in section 5.4.1. It is the unfolding matrix, $\mathbf{E}$ on which we focus in the remainder of this section, though since the other matrices are straightforward to find, we will use $\mathbf{E}$ interchangeably with $\mathbf{M}$.

The root problem with arriving at $\mathbf{M}$ is that it is not constrained mathematically. We have, from the MC, a similar equation to 5.3 above, namely

$$\mathbf{D}_{\mathbf{true}}^{\mathbf{MC}} = \mathbf{M} \cdot \mathbf{D}_{\mathbf{raw}}^{\mathbf{MC}} \tag{5.4}$$

which, if we have a fifteen-bin problem, represents fifteen equations and fifteen-squared unknowns.

5.3.1 Naive method

One way to proceed might be to find $\mathbf{M}$ as it stands on the right-hand side of equation 5.4. This is to say every time a true energy in bin i is reconstructed in bin j, M_{ij} is incremented by one. One does this over all events, and in the end normalizes the columns of $\mathbf{M}$ to add up to one in order that event number is conserved. One is left with M_{ij}, the probabilities that an entry in bin j, reconstructed, came from bin i, true. From the language alone one might suspect a problem, and this is confirmed by inspecting the result of using a new $\mathbf{D}_{\mathbf{true}}^{\mathbf{MC}}$, on which the unfolding matrix had better

not depend. A new, true input MC distribution is obtained by merely re-weighting the old one,

$$\begin{aligned} D^{MC'}_{truei} &= D^{MC}_{truei} \cdot \frac{D^{MC'}_{truei}}{D^{MC}_{truei}} \\ &= D^{MC}_{truei} \cdot f_i, \end{aligned} \tag{5.5}$$

where there is not a sum here over the repeated index i and, of course, both the old un-primed and new primed distributions must integrate to the same number and be smooth over $0 \leq x \leq 1$ ($0 \leq i \leq 15$). Now, when this is done, the new $\mathbf{M}$ becomes

$$M'_{ij} = f_i \cdot M_{ij}, \tag{5.6}$$

where, again, there's no sum over i. Normalizing over j to conserve events gives $\sum_j f_i \cdot M_{ij}$ which is *not* equal to $\sum_j M_{ij}$, and thus, upon dividing, the new M'_{ij}s are not equal to the old M_{ij}s without the primes, and the unfolded data will be different depending on the MC model. This is not good.

5.3.2 Correct, but Afflicted with Problems

In a perfect world, we would proceed differently. Namely, we would build $\mathbf{M}^{-1}$ on the left-hand side of equation 5.4. This matrix is the one that smears (folds) and applies any offset to the true distribution to get to the raw one. We would then invert this matrix to get $\mathbf{M}$ and apply it to the right hand side of 5.3. One builds $\mathbf{M}^{-1}$ event-by-event, as before, and normalizes each of its elements by the sum of the elements in its columns in order to maintain event number conservation. Now the ij^{th} element of $\mathbf{M}^{-1}$ has the interpretation that it is the probability that an entry in true bin i migrates to bin j of the reconstructed distribution. The words this time lead us to suspect that this is correct, and this is demonstrated by repeating the re-weighting exercise above. Equation 5.6 becomes

$${M^{-1}}'_{ij} = f_i \cdot {M^{-1}}_{ij} \tag{5.7}$$

and then in the sum over j one can pull out the common factor f_i. Then, upon dividing $f_i \cdot {M^{-1}}_{ij}$ by this sum, it cancels and ${M^{-1}}'_{ij} = {M^{-1}}_{ij}$. Woo-hoo.

This strategy was pursued temporarily, even getting so far along as to invert $\mathbf{M}^{-1}$, apply it to the raw, MC distribution and show that it reproduced the input. Disaster was met immediately upon applying this $\mathbf{M}$ to the raw data. Negative bin contents and an oscillatory solution with increasing i of $D^{data}_{true\,i}$ were observed.

Upon consultation of reference [100], one is perhaps not so surprised. There both raw and unfolded distributions are expressed as Fourier series, where the functions being expanded are taken to be periodic over the range of interest. In [101] and [100] it is shown that the Fourier coefficients of the unfolded distribution are equal to those of the raw distribution, but amplified by the factor $\exp(\nu^2\sigma^2/2)$, where ν is the index of the frequency of the mode to which the coefficient is associated and σ is a width of a gaussian characterizing the smearing. The ever-decreasing coefficients (with increasing ν) of the presumably smooth, true distribution become amplified and rely on delicate cancellations with other now-large coefficients to satisfy the Fourier expansion. However, generally, the high frequency coefficients will *not* be reproduced from the raw distribution because those high-frequency coefficients are measured only to within statistical errors – which get amplified by the exponential function. The result is statistical fluctuations in the unfolded result.

So far the question has not been answered as to why the inversion procedure suffers from this problem while the "non-inversion" procedure does not. The answer given in [101] is that in the non-inversion procedure the output is still given as a Fourier expansion, but each reconstructed bin's contents are not arrived at by summing entries from the true bins with gaussian smearing. The reconstructed bins are considered to just be some fraction of the contents of the true bins, in accordance with the language of section 5.3.1. Therefore, there is no $\exp(\nu^2)$ behavior to drive oscillations. Instead, one gets out what one puts in in the non-inversion method.

5.3.3 The Procedure Used Here

Here we describe the method used to unfold from the raw distribution in this analysis. Equations 5.4 and 5.3 represent the 30 equations that must be satisfied, and from which we must extract a consistent value of $\mathbf{M}$. The inspiration for this procedure is reference [8]. The procedure is the following, with $\mathbf{E}$ used in place of $\mathbf{M}$, as the distinction is now necessary.

1. At the zeroth iteration take the unfolding to be purely diagonal with no smearing, $\mathbf{E} = \mathbf{1}$, so that
$$\mathbf{D}_{\mathbf{true}}^{\mathbf{data}} = \epsilon \cdot \mathbf{B} \cdot \mathbf{D}_{\mathbf{raw}}^{\mathbf{data}}.$$
2. Fill the first two kinematically allowed bins with the value from a Peterson parametrization, since the acceptance in those bins is not good and subject to big modeling errors. The error due to the selection of this particular parametrization will be accounted for in a way to be described in section 5.4.1. The possible parametrizations are all (with the exception of the third-order polynomial, P_3) single peaked and inspired by fragmentation models, though this is unnecessary. Table 5.2 shows the x—dependence of the chosen functions.
3. Fit $\mathbf{D}_{\mathbf{true}}^{\mathbf{data}}$ with a chosen function using `MINUIT`.
4. Use this function as the input MC model. In practice this means re-weighting the MC events according to this function. If the above step had been omitted, and we tried to just use the data as it stood for the input MC model, its lack of smoothness would prevent convergence.
5. Now from the Monte Carlo, extract $\mathbf{E}$ in the way described above in section 5.3.1. Use this in the data, as in equation 5.2. The first two bins, however, are filled from the last fit. Go to step 3.

The above procedure is followed until the final distribution has moved in each bin by less than 10%. At that point one is finished and has the final distribution. This procedure was shown to be able to reproduce, to within statistical errors, "data" spectra from toy Monte Carlo models with a wide range of input $\langle x_E \rangle$.

5.4 Errors

The statistical errors are tricky due to correlations and will be handled in detail in the appropriate subsection below. However, all plots that show statistical error bars show only the uncorrelated contribution.

The systematic errors in this measurement may be categorized as either detector or physics modeling errors. The physics modeling errors are handled by a standard event weighting scheme, wherein the parameter of the MC that controls the systematic effect under study is varied by the amount indicated. Generator level MC is run to

Table 5.2: Functions used in the iterative unfolding, up to normalization constants. Below, their initial and final χ^2s and final $\langle x_E \rangle$ on the corrected data.

$$
\begin{aligned}
f_{Peterson}(x) &\sim \frac{1}{x}(1 - \frac{1}{x} - \frac{\epsilon_b}{1-x})^{-2} \\
f_{Lund}(x) &\sim \frac{1}{x}(1-x)^a exp(-bm_T^2/x) \\
f_{BCY_{P/V}}(x) &\sim \frac{r(1-2r)(2r)^2}{(1-(1-r)(1-2r))^6}[6+\ldots] \\
f_{AL}(x) &\sim a\frac{1+b(1-x)}{x}(1 - \frac{c}{x} - \frac{d}{1-x})^{-2} \\
f_{P_3}(x) &\sim 1 + ax + bx^2 + cx^3
\end{aligned}
$$

Fnl. form	χ^2_i	χ^2_f	$\langle x_E \rangle = \frac{\int dx\, x\, f(x)}{\int dx\, f(x)}$
Peterson	33.0/10	2.4/10	0.712
Lund	157./9	.9/9	0.708
BCY	71./10	4.4/10	0.691
AL	18.4/8	2.5/8	0.721
P_3	115./8	3.6/8	0.677

determine the relative weight given to the event under the new condition and the new ϵ, $\mathbf{E}$ and $\mathbf{B}$ matrices are constructed. $\mathbf{E}$, as always, is only the *initial* unfolding matrix in each case, which we re-weigh by the data (as explained in section 5.3) in each zeroth iteration before really getting started iterating. Similarly, we investigate the effect of the various y_cs and of the neutral energy correlation fit by using those new conditions in the MC and re-making all three matrices.

In all cases we run the analysis on the data with the appropriate y_c and E_{neu} correction with the exact same code as in the MC. Thus, to investigate the effect of the 97 sources of systematic error of table 5.3 we perform the iteration 97 times with the 97 sets of MC-derived matrices.

5.4.1 Systematic Errors

The detector modeling errors are dominated by the energy resolution in the calorimeter, and the error on it is taken to be the error on the fit of the MC correlation, as shown in figure 5.4. Another source of detector error that one could imagine considering is the uncertainty on the MC track multiplicity. However, the final number of tracks in a vertex are in good agreement with the data, and that is our chief concern about the track multiplicity. The good correlation between reconstructed and true charged fragmentation energy shows that the error on that fit will be small compared to the neutral energy fit. It is also worth explicitly stating that we could apply a correction there as we do with the neutral energy, but the unfolding process will make that correction for us.

There are a lot of uncertainties that could potentially be troublesome in B physics analyses. Some of the production ratios for excited mesons and decay branching ratios are not known to better than 25%, for example. The various B and D hadron production proportions are uncertain, as is also true of their various decay branching ratios. In particular, the variation of Λ_b and B_s° production is taken to be $\approx 90\%$. It's also possible that backgrounds will vary with things like strange hadron production. We thus vary the $s\bar{s}$ "popping fraction" (which produces a different amount of $s\bar{s}$ pairs from the QCD vacuum and thus a different number of Ks and Λs) by 10%. If the c quark fragmentation function is stiffer or softer than we expect, then we may get more Ds and Λ_cs, which may give a different vertexing rate. Thus, it is varied around its world-average uncertainty. We also vary the rate of production from the Z^0 of $c\bar{c}$ and $b\bar{b}$ pairs (R_c and R_b) by 2σ and 1σ, respectively, around their central values. The B and D decay track multiplicities are varied and are shown to produce small errors. Since this analysis has presumed that Bs are produced only as a result of the hadronization of the initial $b\bar{b}$ pairs and not as a result of such pairs popping out of the QCD vacuum or from gluon splitting to $b\bar{b}$ and $c\bar{c}$, the errors on these quantities are varied by 50% around their Lund-inspired expectations (see equation 2.18). The errors on $f_{B^{**}}$ and $m_{B^{**}}$ have already been mentioned and are shown to be small. The effect of ignoring B**s is shown in the table. The line with numbers in brackets indicates that without B**s ($f_{B^{**}} \to 0$) $\delta\langle x_E \rangle = -3.27\%$.

None of these is too large, reflecting the fact that this type of inclusive analysis is not very sensitive to the fine details of the B physics. This might be compared to the

case of reference [8], in which the D and D* are reconstructed, and only such events producing nice D* mass peaks are considered for energy reconstruction.

It turns out that the biggest physics error is that due to the variation of the jet parameter y_c in the standard [60] range. The error, 2.57%, is from $y_c = 0.002$, a value at which there are considerably more multi-jet events than at the standard $y_c = 0.005$, making lepton-jet assignment more difficult.

The next biggest error of 2.27% comes from the variation due to the choice of fitting function. Though considerable by comparison to the others, it actually demonstrates dramatically the stability of the iterative method employed here against the initial starting point of the iterations and of the explicit functional form. In fact, functions that were chosen for the fit were not omitted from consideration merely because their first fit to the raw data yielded poor χ^2s. This is in contrast to the criteria used in [8]. Table 5.2 shows the initial and final χ^2s for all the functions, demonstrating that all the functions, by their last iteration, give a good fit. That is to say, the process of iteration drives the data to look like the particular functional form being used, so that there does exist an unfolding matrix $\mathbf{E}$ that can take the reconstructed MC into the true MC and simultaneously make the data converge. Thus, there is no reason to have excluded any of those functions from the outset. We have used a wide variety of functions in the iterative process and and thus give a conservative error.

Table 5.3 is the collection of the sources of systematic error and the size of their effects.

5.4.2 Statistics

Care must be taken in the treatment of the statistical errors. Changing notation in order to be general, we have a problem of the form

$$\mathbf{y} = \mathbf{M} \cdot \mathbf{x}, \tag{5.8}$$

where $\mathbf{y}$ is the true distribution unfolded using the matrix $\mathbf{M}$ from the raw distribution $\mathbf{x}$. The errors on the number of entries in each of the raw bins x_i are taken to be the usual Poisson errors $\delta x_i = \sqrt{Np_i(1-p_i)}$. N is the total number of entries in the raw distribution and p_i is the probability of finding an entry in bin i. δx_i reduces to the usual $\sqrt{x_i}$ if p_i is small – *i.e.* in the limit of very narrow bins. The errors on the y_i, which is what we care about in the end, are found by expanding 5.8 in a Taylor series. For our simple function the Taylor series terminates after two terms, which makes the approximate treatment of covariance matrices exact.

In general, the covariance matrix of $\mathbf{y}$ in terms of the independent variables $\mathbf{x}$ is [102]

$$V_{y_i y_j} = \frac{\partial y_i}{\partial x_k} V_{x_k x_l} \frac{\partial y_j}{\partial x_l}. \tag{5.9}$$

We assert that the correlation among the raw bins is given by

$$V_{x_m x_n} = Np_m(1-p_m)\delta_{mn}.$$

In other words, there is no correlation at the raw level, as we measure an entry in a bin at the raw level in one event with no bearing on which raw bin we measure it in in the next event. (Things would be different if we started with some assumption about the overall shape of the initial spectrum. There, there might be a correlation that would be given according to the correlation between any two bins k and l in a multinomial distribution, namely $-Np_kp_l$.) Therefore, equation 5.9 becomes

$$V_{y_i y_j} = \sum_k M_{ik} M_{kj} N p_k (1-p_k),$$

showing that a correlation is induced among the unfolded variables, even though none is present at the raw level. For a case such as ours where the x_is are uncorrelated, the diagonal covariance terms from 5.9 have the form familiar from naive application

of standard error propagation

$$V_{y_i y_i} = (\frac{\partial y_i}{\partial x_k})^2 V_{x_k x_k}$$

or

$$\sigma^2_{y_i y_i} = (\frac{\partial y_i}{\partial x_k})^2 \sigma^2_{x_k x_k}.$$

The average value of y, $\overline{n}$, is a function of the independent variables y_i according to $\overline{n} = \sum_i i y_i / \sum_i y_i$. Then

$$\begin{aligned} \delta\overline{n}^2 &= \frac{\partial \overline{n}}{\partial y_k} V_{y_k y_l} \frac{\partial \overline{n}}{\partial y_l} \\ &= V_{y_k y_l} \cdot \frac{1}{N^2}(k - \overline{n})(l - \overline{n}) \qquad (5.10) \\ &= M_{km} V_{x_m x_n} M_{ln} \cdot \frac{1}{N^2}(k - \overline{n})(l - \overline{n}). \qquad (5.11) \end{aligned}$$

If one ignored the correlations introduced by the unfolding, then $V_{y_k y_l} = \sigma^2_k \delta_{kl}$, and 5.10 is instead

$$\delta\overline{n}^2 = \frac{1}{N^2} \sum_i (i - \overline{n})^2 \sigma^2_i \qquad (5.12)$$

which, if $\sigma_i = \sqrt{y_i}$, gives the familiar

$$\delta\overline{n} = rms/\sqrt{N}. \qquad (5.13)$$

We will use equation 5.11 and not 5.13.

The correlation coefficient, ρ, given by

$$\rho_{y_i y_j} = \frac{V_{y_i y_j}}{\sqrt{V_{y_i y_i} V_{y_j y_j}}} = \frac{V_{y_i y_j}}{\sigma_i \sigma_j} \qquad (5.14)$$

and shown in table 5.4 demonstrates the high degree of correlation of the statistical errors among the bins. This says that an entry in a reconstructed bin j does not have a probability near 1 to have come from the true bin j, but generally comes from a range of bins around true bin j.

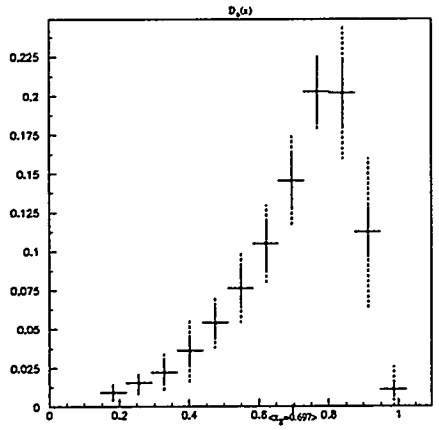

Figure 5.8: Data: Final E_B spectrum. The sold lines are statistical errors, the dashed includes systematic errors as well.

5.5 Results

The final, unfolded data gives the x_E spectrum shown in figure 5.8. The statistical error bars (uncorrelated only) are solid and the total error bars are dashed. Figure 5.9 shows this same spectrum with the various theoretical curves from chapter 2 overlaid.

It is worth pointing out that none of the curves in figure 5.9 is the final fit from the iteration procedure, listed in table 5.2. Those functions have the same general shape (and the same name) as many of the theoretical curves, but that can be considered to be merely convenient. Their purpose was just to aid in the unfolding. The curves in figure 5.9 are those shapes obtained by starting in the MC in the variable z – longitudinal energy fraction of the hadron with respect to the quark – the variable in which the functions from theory are defined, and using JETSET7.4 to give us the answer in terms of x. Many such curves were generated for each function over a range of its free parameters, and the ones that gave the best χ^2 for the final, unfolded data spectrum are the ones plotted. The exception is the curve labeled "Nason/Colangelo/Mele" which is constructed using code graciously supplied by Paolo Nason [103] for just two sets of parameters – those suggested by reference [43]. The one giving the better fit is shown here. That calculation is transformed from z into x directly, as explained in section 2.4.1. Note that none can be ruled out with the errors as shown.

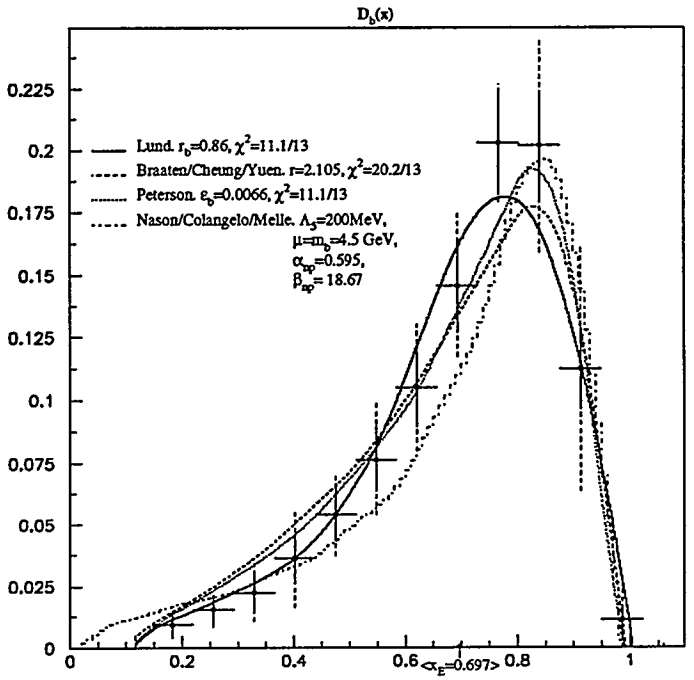

Figure 5.9: Data: Final E_B spectrum, exactly as in figure 5.8. Overlaid are four theoretical models. In the first three curves the calculated function in the variable z is taken into the measurable one, x, with JETSET7.4. The fourth curve labeled Nason/Colangelo/Mele is calculated directly in x, as explained in section 2.4.1.

5.6 Conclusions

We have demonstrated that we are able to measure the raw B energy on 96% of our sample to 10% accuracy. We have shown that we may unfold this raw result to get the true spectrum using an iterative procedure, and that the resulting value of $\langle x_E \rangle$ is largely independent of the initial starting point and of the functional form used in the iterative procedure. As a check, toy MC "Data" distributions with a wide range of input $\langle x_E \rangle$ were reproduced with this method.

We conclude that the b quark fragmentation function, as measured in this semileptonic B-decay sample at SLD, yields a value of $\langle x_E \rangle = 0.697 \pm 0.017(stat) \pm 0.034(sys)$. It may be observed from figure 5.10 that these errors are competitive with some of the measurements made from the LEP experiments with data samples 20 times larger.

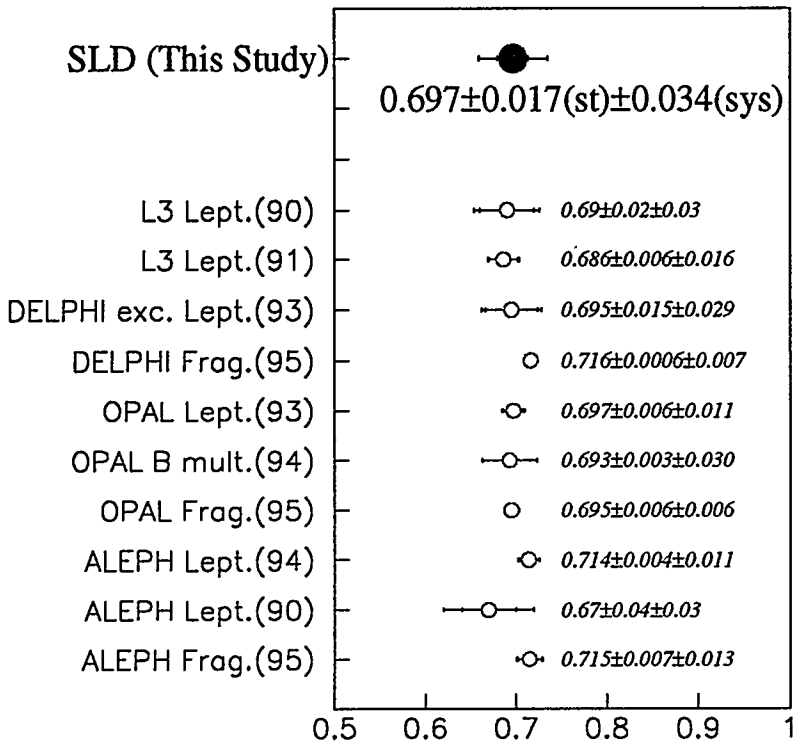

Figure 5.10: Data: Final $< x_E >$ for this measurement, with LEP results as shown. Statistical errors are indicated by the inner error bars, and the total error is shown with the outer error bars. See references [104] for the LEP results.

The measurement presented here is particularly competitive with the '95 ALEPH measurement which, we believe, comes the closest to correctly handling the uncertainties in the unfolding procedure. It is also true that given both systematic and statistical uncertainties many theoretical shapes are consistent with the measured function.

Table 5.3: Summary of detector and physics systematics for the b quark average scaled energy, $< x_E >$. The equation for the statistical error may be recognized as the expression 5.10 with y_i replaced by $D_b(x)$ and $\overline{n}$ replaced by $< x_E >$.

	ERROR (%)
STATISTICS	
$\{Tr[(\frac{\partial(x_E)}{\partial D_b(x)}) \cdot V \cdot (\frac{\partial(x_E)}{\partial D_b(x)})^T]\}^{\frac{1}{2}}$	2.4
DETECTOR MODELING	
E_0	3.16
PHYSICS MODELING	
Choice of Fitting Function	
$f_{Pete,AL,Bowl,BC,P_3}$	2.27
B-lifetimes	
($\tau_{Bmeson} = 1.55 \pm 0.10$ ps,	0.25
$\tau_{Bbaryon} = 1.10 \pm 0.30$ ps)	
$\mathbf{f_{B^{**}}}$ $(20.7 \pm 7\%)$	0.25
[-20.7%]	[-3.27]
$\mathbf{m_{B^{**}}}$ $(5.704 \pm 0.020$ GeV)	0.29
B-decay to D*/D $(3-1)$	0.34
B-decay to D/D** (3 ± 1)	0.32
$\mathbf{B_u, B_d, B_s, \Lambda_b}$ **production**	
$(40.1 \pm 20\%, 40.1 \pm 20\%, 11.6 \pm 8.0\%, 8.9 \pm 8.0\%)$	0.31
$\mathbf{B_u, B_d, B_s, \Lambda_b}$ **decay (6 modes each** $\pm 1\sigma$)	0.09
B-decay multiplicity (±0.25 tracks per B decay)	0.32
c-fragmentation	
(Peterson $\langle x_E \rangle$ for D* $= 0.501 \pm 0.025$)	0.02
$\mathbf{D^0, D^+, D_s, \Lambda_c}$ **production**	
$(56. \pm 5.3\%, 23. \pm 3.7\%, 12. \pm 7.\%, 8.9 \pm 0.5\%)$	0.02
c decay multiplicity ($\delta n_{D^0,D^+,D_s,\Lambda_c} = 6, 10, 31, 40\%$)	0.01
s production ($s\overline{s}$ **popping varied by 10%**)	0.27
$R_b(\pm 0.003)$	0.03
$R_c(\pm 0.02)$	0.05
$g \rightarrow b\overline{b}$ **splitting(±50%)**	1.22
$g \rightarrow c\overline{c}$ **splitting(±50%)**	0.15
Jet Axis Modeling	
(JADE y_{cut} varied from 0.002 to 0.020)	2.57
Sub-total	3.73
TOTAL	**5.44**

Table 5.4: The statistical correlation matrix, ρ.

	1	2	3	4	5	6	7	8	9	10	11	12
1	1.00	0.17	0.49	0.48	0.25	0.24	0.15	0.07	0.03	0.01	0.01	0.02
2		1.00	0.84	0.80	0.77	0.84	0.80	0.57	0.46	0.47	0.38	0.36
3			1.00	0.97	0.89	0.87	0.85	0.68	0.51	0.41	0.30	0.28
4				1.00	0.94	0.89	0.90	0.77	0.59	0.46	0.37	0.35
5					1.00	0.86	0.92	0.80	0.59	0.45	0.32	0.30
6						1.00	0.92	0.76	0.57	0.38	0.29	0.25
7							1.00	0.94	0.81	0.66	0.54	0.49
8								1.00	0.94	0.77	0.64	0.58
9									1.00	0.92	0.81	0.75
10										1.00	0.93	0.88
11											1.00	0.99
12												1.00

BIBLIOGRAPHY

[1] SLD Collaboration, K. Abe *et al.*, *Phys. Rev. Lett.* **73** (1994) 25.

[2] SLD Collaboration, K. Abe *et al.*, *Z. Phys.* **C62** (1994) 179.

[3] J. Jaros *et al.*, "B Lifetimes and Mixing With the SLD," SLAC-PUB-7067, (1995).

[4] SLD Collaboration, K. Abe *et al.*, "Measurement of the Average B Hadron Lifetime in Z^0 Decays Using Reconstructed Vertices," *Phys. Rev. Lett.* **75** (1995) 3624.

[5] B. Adeva *et al.*, "Measurements of $Z^0 \to b\bar{b}$ Decays and the Semileptonic Branching Ratio BR($b \to lx$)," *Phys. Lett.* **B261** (1991) 177.
DELPHI Collaboration, P. Abreu *et al.*, "A Measurement of B Meson Production and Lifetime Using Dl^- Events in Z^0 Decays," *Z. Phys.* **C57** (1993) 181.
ALEPH Collaboration, D. Buskulic *et al.*, "Heavy Flavour Production and Decay with Prompt Leptons in the ALEPH Detector," *Z. Phys.* **C62** (1994) 179.

[6] DELPHI Collaboration, P. Abreu *et al.*, "Inclusive Measurement of the b Fragmentation Function," DELPHI/95-103 Phys. 538 (1995).

[7] OPAL Collaboration, P.D. Acton *et al.*, "A Study of b Quark Fragmentation into B^0 and B^+ Mesons at LEP," CERN-PPE/95-122 (1995).

[8] ALEPH Collaboration, D. Buskulic *et al.*, "Measurement of the Effective b Quark Fragmentation Function at the Z^0 Resonance," *Phys. Lett.* **B357** (1995) 699.

[9] ALEPH collaboration, D. Buskulic *et al.*, CERN PPE-95-084 (1995).

[10] F.J. Hasert *et al.*, *Phys. Lett.* **B46** (1973) 138.

[11] C. Rubbia *et al.*, *Rev. Mod. Phys.* **57** (1985) 699.

[12] H. Dehmelt, R. Van Dyck, and Schwinberg, *Phys. Rev. Lett.* **59** (1987) 26.

[13] SLD Collaboration, K. Abe *et al.*, "Search for Jet Handedness in Hadronic Z^0 Decays," *Phys. Rev. Lett.* **74** (1995) 1512.

[14] SLD Collaboration, K. Abe *et al.*, "Measurement of the Parity-Violating Parameters A_b and A_c From the Left-Right Forward-Backward Asymmetry of Leptons in Hadronic Events at the Z^0 Resonance," *Phys. Rev. Lett.* **74** (1995) 2895.

[15] CDF Collaboration, F. Abe *et al.*, "Observation of Top Quark Production in $p\overline{p}$ Collisions With the Collider Detector at Fermilab," *Phys. Rev. Lett.* **74** (1995) 2626.

[16] D0 Collaboration, A. Bhatti *et al.*, "Observation of the Top Quark," *Phys. Rev. Lett.* **74** (1995) 2632.

[17] G. 't Hooft, "Recent Devolopments in Gauge Theories," in *Cargése Summer School* (1979) 135.

[18] R. N. Mohapatra, *Unification and Supersymmetry*, Springer-Verlag (1992).

[19] Peter C. West, *Introduction to Supersymmetry and Supergravity*, World Scientific (1990).

[20] J.A. Bagger, "The Status of Supersymmetry," Johns Hopkins University, (1995) hep-ph/9508392.

[21] D. Bailin and A. Love, *Supersymmetric Gauge Field Theory and String Theory*, Institute of Physics (1994).

[22] Pierre Ramond, *Field Theory: A Modern Primer*, Addison-Wesley (1990).

[23] D.J. Gross and F. Wilczek, *Phys. Rev.* **D8** (1973) 3633.

[24] K. Wilson, *Phys. Rev.* **D3** (1971) 1818.

[25] T. Cheng and L. Li, *Gauge Theories of Elementary Particle Physics*, Oxford University Press (1984).

[26] Chris Quigg, *Gauge Theories of the Strong, Weak and Electromagnetic Interactions*, Addison-Wesley (1983).

[27] E. Witten and N. Seiberg, *Nucl. Phys.* **B426** (1994) 19.

[28] C. Rosenzweig, "The QCD Vacuum," *Particle World* **4** (1995) 19.

[29] G. 't Hooft, *Phys. Scr.* **25** (1982) 13.

[30] S. Mandelstam, *Phys. Rep.* **C23** (1976) 245.

[31] Lewis H. Ryder, *Quantum Field Theory*, Cambridge University Press (1991).

[32] M. Baker, J. Ball, and F. Zachariesen, *Phys. Rep.* **209** (1991) 73.

[33] F. Halzen and A.D. Martin, *Quarks & Leptons: An Introductory Course in Modern Particle Physics*, John Wiley & Sons (1984).

[34] J.T. Friedman and H.W. Kendall, *Ann. Rev. Nuc. Sci.* **22** (1972) 203.

[35] T. Muta, *Foundations of Quantum Chromodynamics*, World Scientific (1987).

[36] T. D. Lee and M. Nauenberg, *Phys. Rev.* **133B** (1964) 1549.

[37] ALEPH Collaboration, D. Buskulic *et al.*, *Phys. Lett.* **B357** (1995) 487.

[38] Y. Dokshitzer, V. Khoze and S. Troyan, "Specific Features of Heavy Quark Production: Leading Quarks," LU-TP-92-10 (1992).

[39] Y. Dokshitzer, V. Khoze, A.H. Mueller and S. Troyan, *Basics of Perturbative QCD*, Editions Frontières Publishing (1991).

[40] A. Basetto, M. Ciafaloni and G. Marchesini, "Jet Structures and Infrared Sensitive Quantities in Perturbative QCD," *Phys. Rep.* **100** (1983) 202.

[41] R. Field, *Applications of Perturbative QCD*, Addison-Wesley (1988).

[42] B. Mele and P. Nason, "Next-to-Leading QCD Calculation of the Heavy Quark Fragmentation Function," *Phys. Lett.* **B245** (1990) 635.

[43] B. Mele and P. Nason, "The Fragmentation Function for Heavy Quarks in QCD," *Nucl. Phys.* **B361** (1991) 626.

[44] G. Colangelo and P. Nason, "A Theoretical Study of the c and b Fragmentation Function in e^+e^- Annihilation," *Phys. Lett* **B285** (1992) 167.

[45] E. Braaten, K. Cheung and T.C. Yuan, "QCD Fragmentation Functions for B_c and B_c^* Production," *Phys. Rev.* **D48** (1993) R5049.

[46] B. Andersson, G. Gustafson, G. Ingelman, T. Sjöstrand, *Phys. Rep.* **97** (1983) 32.

[47] J. Schwiening, "First Measurements on Gluon Splitting into Heavy Quarks in e^+e^- Annihilation," BONN-HE-95-03 (1995).

[48] E. Braaten, K. Cheung, S. Fleming and T.C. Yuan, "Perturbative QCD Fragmentation Functions as a Model for Heavy Quark Fragmentation," Fermilab-PUB-94-305-T (1994).

[49] T. Sjöstrand and M. Bengtsson, *Comp. Phys. Comm.* **43** (1987) 367.

[50] B. Andersson, G. Gustafson and B. Söderberg, LU-TP-83-2 (1983).

[51] M.G. Bowler, *Z. Phys.* **C11** (1981) 169.

[52] C. Peterson, D. Schlatter, I. Schmitt and P.M. Zerwas, "Scaling Violations in Inclusive e^+e^- Annihilation Spectra," *Phys. Rev.* **D27** (1983) 105.

[53] RHIC Spin Collaboration, "Proposal on Spin Physics Using the RHIC Polarized Collider," August (1992).

[54] M. Seymour, "Heavy Quark Pair Multiplicity in e^+e^- Events," *Nucl. Phys.* **B436** (1995) 163.

[55] ARGUS Collaboration, H. Albrech *et al.*, *Phys. Lett.* **B234** (1991) 297.
CLEO Collaboration, J. Bartelt *et al.*, *Phys. Rev. Lett.* **71** (1993) 4111.

[56] N. Cabibo and L. Maiani, *Phys. Lett.* **B79** (1978) 109.
M. Suzuki, *Nucl. Phys.* **B145** (1978) 420.

[57] M. Neubert, *Phys. Lett.* **B264** (1991) 455.

[58] S. Stone, "Semileptonic B Decays," in *B Decays*, World Scientific Press (1994) 283.

[59] G. Marchesini and B.R. Webber, in *Proceedings in Z Physics at LEPI*, edited by Z. Kunszt and P. Nason, **1** (1988) 373.

[60] SLD Collaboration, K. Abe *et al.*, "Measurement of α_s from Hadronic Event Observables at the Z^0 Resonance," *Phys. Rev.* **D51** (1995) 962.

[61] S. Bethke, Z. Kunszt, D. Soper and W. Stirling, *Nucl. Phys.* **B370** (1992) 310.

[62] David C. Williams, "The Left-Right Forward-Backward Asymmetry for b Quarks at the SLD," PhD Thesis, Massachusetts Institute of Technology (1994).

[63] M. Breidenbach, "SLC and SLD – Experimental Experience With the Linear Collider," SLAC-PUB-6313 (1993).

[64] "The SLD Design Report," SLAC Report 229 (1980).

[65] M.L. Swartz, "Polarization at SLC," SLAC-PUB-4656 (1988).
T. Maruyama *et al.*, *Phys. Rev. Lett.* **66** (1991) 2351.
T. Maruyama, R. Prepost, *Annual Review of Nucl. Part. Sci.* **45** (1995) 41.

[66] C. Adolphson *et al.*, SLAC-PUB-6118 (1993).

[67] M. Breidenbach *et al.*, Presented at the 2nd International Workshop on Physics and Experiments with Linear Colliders, Waikala, Hawaii, SLC-PUB-6313 (1993).

[68] M.J. Fero, "The Compton Polarimeter for SLC," SLAC-PUB-6026 (1992).

[69] G. Blaylock, "The WISRD Beam Energy Measurements," SLC-Physics Note 22 (1993).

[70] "The SLD Design Report," SLAC Report 273 (1984).

[71] SLD Collaboration, K. Abe *et al.*, "The Compton Polarimeter for SLC," SLAC-PUB-6026 (1992).

[72] K. Pitts, "Electroweak Coupling Measurements from Polarized Bhabha Scattering at the Z^0 /Resonance," PhD Thesis, University of Oregon (1994).

[73] C. Damerall, F. Farley, A. Gillman and F. Wickens, *Nucl. Instr. & Meth.* **185** (1981) 33.

[74] G. Agnew *et al.*, SLAC-PUB-5905 (1992).

[75] S.G. Martirena, "A Calorimetric Measurement of the Strong Coupling Constant in Electron-Positron Annihilation at a Center-of-Mass Energy of 91.6 GeV," Massachusetts Institute of Technology (1994).

[76] W.J. Willis *et al.*, "Liquid Argon Ionization Chambers as Total-Absorption Detectors," *Nucl. Inst. and Meth.* **120** (1974) 120.

[77] D. Axen *et al.*, "The Pb-Ar Sampling Calorimeter of the SLD," *Nucl. Inst. and Meth.* **A328** (1993) 472.

[78] SLD Collaboration, K. Abe *et al.*, *Phys. Rev. Lett.* **75** (1995) 4173.

[79] SLD Collaboration, K. Abe *et al.*, "Measurements of R_b With Impact Parameters and Displaced Vertices," *Phys. Rev.* **D53** (1996) 1023.

[80] SLD Collaboration, K. Abe *et al.*, "A Status Report on the SLD Data Acquisition System," *IEEE Trans. on Nucl. Sci.* **36** (1989) 23.

[81] G. Marchesini *et al.*, "HERWIG 5.1 - A Montecarlo Event Generator for Simulating Hard Emission Reactions with Interfering Gluons," *Comput. Phys. Commun.*, **67** (1992) 465.

[82] T. Junk, "Measurement of the Polarized Forward-Backward Asymmetry of b Quarks Using Momentum-Weighted Track Charge at SLD," PhD Thesis, Stanford University (1995).

[83] H. Neal, "A Measurement of $\Gamma(Z^0 \to b\bar{b})/\Gamma(Z^0 \to hadrons)$ Using the SLD," PhD Thesis, Stanford University (1995).

[84] J. Yamartino, "A Measurement of the e^+e^- Decay Width of the Z^0," PhD Thesis, Massachussetts Institute of Technology (1994).

[85] R. Wang, PhD Thesis, University of Minnesota (1994).

[86] ALEPH Collaboration, D. Buskulic *et al.*, *Phys. Lett.* **B313** (1993) 535.
OPAL Collaboration, P.D. Acton *et al.*, *Z. Phys.* **C60** (1993) 579.
OPAL Collaboration, D. Akers *et al.*, CERN-PPE/94-106 (1994).
DELPHI Collaboration, P. Abreu *et al.*, CERN-PPE/94-131 (1994).

[87] ALEPH Collaboration, D. Buskulic *et al.*, *Z. Phys.* **C62** (1994) 179.
DELPHI Collaboration, P. Abreu *et al.*, *Z. Phys.* **C56** (1992) 47.
L3 Collaboration, 0. Adeva *et al.*, *Phys. Lett.* **B259** (1991) 199.
OPAL Collaboration, P.D. Acton *et al.*, *Z. Phys.* **C58** (1993) 523.

[88] SLD Collaboration, K. Abe *et al.*, "The Lifetime Probability Tag Measurement of R_b Using the SLD," SLAC-PUB-95-7004 (1995).

[89] SLD Collaboration, K. Abe *et al.*, *Phys. Rev. Lett.* **74** (1995) 2895.

[90] D. Jackson, "ZVTOP - A Topological Vertex Finding Algorithm for Hadronic Jets," SLD Physics Note (1996).

[91] G. Grindhammer *et al.*, *Nucl. Instr. Meth.* **A290** (1990) 469.

[92] S. Youssef, *Comp. Phys. Comm.* **45** (1987) 423.

[93] H. Hwang, "QCD Test in Three-Jet Z^0 Decays at SLD and Detector Development for $H^0 \to \gamma\gamma$ Searches in High Energy Hadron Colliders," PhD Thesis, University of Oregon (1995).

[94] R. Brun *et al.*, "GEANT3 User's Guide," CERN-DD/EE/84-1 (1989).

[95] R. Bock *et al.*, *Data Analysis Techniques for High-Energy Physics Experiments*, Cambridge University Press (1990).

[96] F. James and M. Roos, "MINUIT Manual," CERN-D506 (1989).

[97] D. Yubing, *High En. Phys. and Nucl. Phys.* **19** (1995) 748.

[98] OPAL Collaboration, P.D. Acton *et al.*, *Z. Phys.* **C66** (1995) 19.
DELPHI Collaboration, P. Abreu *et al.*, *Phys. Lett.* **B345** (1995) 598.
ALEPH Collaboration, D. Buskulic *et al.*, CERN-PPE/95-108 (1995).

[99] R. Bigelow, M. Moloney, J. Philpott and J. Rothberg, *Nuclear Particle Physics Simulations*, J. Wiley & Sons (1995).

[100] V. Blobel, "Unfolding Methods in High Energy Physics Experiments," Proceedings of the CERN School of Computing (1984) 88.

[101] V. Blobel, Private Communication (1995).

[102] A.G. Frodesen and O. Skeggestad, *Probability and Statistics in Particle Physics*, Columbia University Press (1979) 55.

[103] P. Nason, Private Communication (1996). The fortran program provided does the work explained in reference [44].

[104] ALEPH Collab., D. Buskulic *et al.*, *Z.Phys.* **C62** (1994) 179.
ALEPH Collab., D. Buskulic *et al.*, *Phys. Lett.* **B244** (1990) 551.
ALEPH Collab., D. Buskulic *et al.*, *Phys. Lett.* **B357** (1995) 699.
OPAL Collab., P.D. Acton *et al.*, *Z.Phys.* **C61** (1994) 219.
OPAL Collab., P.D. Acton *et al.*, *Z.Phys.* **C58** (1993) 523.
OPAL Collab., P.D. Acton *et al.*, CERN-PPE/95-122 (1995).
DELPHI Collab., P. Abreu *et al.*, *Z.Phys.* **C57** (1993) 181.
DELPHI Collab., P. Abreu *et al.*, DELPHI 95-103 PHYS 538
L3 Collab., O. Adeva *et al.*, *Phys. Lett.* **B241** (1990) 416.
L3 Collab., O. Adeva *et al.*, *Phys. Lett.* **B261** (1991) 177.

Appendix A

THE SLD COLLABORATION

K. Abe,[29] I. Abt,[14] C.J. Ahn,[26] T. Akagi,[27] N.J. Allen,[4] W.W. Ash,[27]†
D. Aston,[27] K.G. Baird,[25] C. Baltay,[33] H.R. Band,[32] M.B. Barakat,[33]
G. Baranko,[10] O. Bardon,[16] T. Barklow,[27] A.O. Bazarko,[11] R. Ben-David,[33]
A.C. Benvenuti,[2] T. Bienz,[27] G.M. Bilei,[22] D. Bisello,[21] G. Blaylock,[7]
J.R. Bogart,[27] T. Bolton,[11] G.R. Bower,[27] J.E. Brau,[20] M. Breidenbach,[27]
W.M. Bugg,[28] D. Burke,[27] T.H. Burnett,[31] P.N. Burrows,[16] W. Busza,[16]
A. Calcaterra,[13] D.O. Caldwell,[6] D. Calloway,[27] B. Camanzi,[12]
M. Carpinelli,[23] R. Cassell,[27] R. Castaldi,[23][a] A. Castro,[21]
M. Cavalli-Sforza,[7] E. Church,[31] H.O. Cohn,[28] J.A. Coller,[3] V. Cook,[31]
R. Cotton,[4] R.F. Cowan,[16] D.G. Coyne,[7] A. D'Oliveira,[8] C.J.S. Damerell,[24]
M. Daoudi,[27] R. De Sangro,[13] P. De Simone,[13] R. Dell'Orso,[23] M. Dima,[9]
P.Y.C. Du,[28] R. Dubois,[27] B.I. Eisenstein,[14] R. Elia,[27] E. Etzion,[4]
D. Falciai,[22] M.J. Fero,[16] R. Frey,[20] K. Furuno,[20] T. Gillman,[24]
G. Gladding,[14] S. Gonzalez,[16] G.D. Hallewell,[27] E.L. Hart,[28] Y. Hasegawa,[29]
S. Hedges,[4] S.S. Hertzbach,[17] M.D. Hildreth,[27] J. Huber,[20] M.E. Huffer,[27]
E.W. Hughes,[27] H. Hwang,[20] Y. Iwasaki,[29] D.J. Jackson,[24] P. Jacques,[25]
J. Jaros,[27] A.S. Johnson,[3] J.R. Johnson,[32] R.A. Johnson,[8] T. Junk,[27]
R. Kajikawa,[19] M. Kalelkar,[25] H. J. Kang,[26] I. Karliner,[14] H. Kawahara,[27]
H.W. Kendall,[16] Y. Kim,[26] M.E. King,[27] R. King,[27] R.R. Kofler,[17]
N.M. Krishna,[10] R.S. Kroeger,[18] J.F. Labs,[27] M. Langston,[20] A. Lath,[16]
J.A. Lauber,[10] D.W.G. Leith,[27] M.X. Liu,[33] X. Liu,[7] M. Loreti,[21] A. Lu,[6]
H.L. Lynch,[27] J. Ma,[31] G. Mancinelli,[22] S. Manly,[33] G. Mantovani,[22]
T.W. Markiewicz,[27] T. Maruyama,[27] R. Massetti,[22] H. Masuda,[27]
E. Mazzucato,[12] A.K. McKemey,[4] B.T. Meadows,[8] R. Messner,[27]
P.M. Mockett,[31] K.C. Moffeit,[27] B. Mours,[27] G. Müller,[27] D. Muller,[27]
T. Nagamine,[27] U. Nauenberg,[10] H. Neal,[27] M. Nussbaum,[8] Y. Ohnishi,[19]
L.S. Osborne,[16] R.S. Panvini,[30] H. Park,[20] T.J. Pavel,[27] I. Peruzzi,[13][b]

M. Piccolo,[13] L. Piemontese,[12] E. Pieroni,[23] K.T. Pitts,[20] R.J. Plano,[25]
R. Prepost,[32] C.Y. Prescott,[27] G.D. Punkar,[27] J. Quigley,[16] B.N. Ratcliff,[27]
T.W. Reeves,[30] J. Reidy,[18] P.E. Rensing,[27] L.S. Rochester,[27] J.E. Rothberg,[31]
P.C. Rowson,[11] J.J. Russell,[27] O.H. Saxton,[27] S.F. Schaffner,[27] T. Schalk,[7]
R.H. Schindler,[27] U. Schneekloth,[16] B.A. Schumm,[15] A. Seiden,[7] S. Sen,[33]
V.V. Serbo,[32] M.H. Shaevitz,[11] J.T. Shank,[3] G. Shapiro,[15] S.L. Shapiro,[27]
D.J. Sherden,[27] K.D. Shmakov,[28] C. Simopoulos,[27] N.B. Sinev,[20]
S.R. Smith,[27] J.A. Snyder,[33] P. Stamer,[25] H. Steiner,[15] R. Steiner,[1]
M.G. Strauss,[17] D. Su,[27] F. Suekane,[29] A. Sugiyama,[19] S. Suzuki,[19]
M. Swartz,[27] A. Szumilo,[31] T. Takahashi,[27] F.E. Taylor,[16] E. Torrence,[16]
J.D. Turk,[33] T. Usher,[27] J. Va'vra,[27] C. Vannini,[23] E. Vella,[27] J.P. Venuti,[30]
R. Verdier,[16] P.G. Verdini,[23] S.R. Wagner,[27] A.P. Waite,[27] S.J. Watts,[4]
A.W. Weidemann,[28] E.R. Weiss,[31] J.S. Whitaker,[3] S.L. White,[28]
F.J. Wickens,[24] D.A. Williams,[7] D.C. Williams,[16] S.H. Williams,[27]
S. Willocq,[33] R.J. Wilson,[9] W.J. Wisniewski,[5] M. Woods,[27] G.B. Word,[25]
J. Wyss,[21] R.K. Yamamoto,[16] J.M. Yamartino,[16] X. Yang,[20] S.J. Yellin,[6]
C.C. Young,[27] H. Yuta,[29] G. Zapalac,[32] R.W. Zdarko,[27] C. Zeitlin,[20]
Z. Zhang,[16] and J. Zhou,[20]

[1] *Adelphi University, Garden City, New York 11530*
[2] *INFN Sezione di Bologna, I-40126 Bologna, Italy*
[3] *Boston University, Boston, Massachusetts 02215*
[4] *Brunel University, Uxbridge, Middlesex UB8 3PH, United Kingdom*
[5] *California Institute of Technology, Pasadena, California 91125*
[6] *University of California at Santa Barbara, Santa Barbara, California 93106*
[7] *University of California at Santa Cruz, Santa Cruz, California 95064*
[8] *University of Cincinnati, Cincinnati, Ohio 45221*
[9] *Colorado State University, Fort Collins, Colorado 80523*
[10] *University of Colorado, Boulder, Colorado 80309*
[11] *Columbia University, New York, New York 10027*
[12] *INFN Sezione di Ferrara and Università di Ferrara, I-44100 Ferrara, Italy*
[13] *INFN Lab. Nazionali di Frascati, I-00044 Frascati, Italy*

[14] *University of Illinois, Urbana, Illinois 61801*
[15] *Lawrence Berkeley Laboratory, University of California, Berkeley, California 94720*
[16] *Massachusetts Institute of Technology, Cambridge, Massachusetts 02139*
[17] *University of Massachusetts, Amherst, Massachusetts 01003*
[18] *University of Mississippi, University, Mississippi 38677*
[19] *Nagoya University, Chikusa-ku, Nagoya 464 Japan*
[20] *University of Oregon, Eugene, Oregon 97403*
[21] *INFN Sezione di Padova and Università di Padova, I-35100 Padova, Italy*
[22] *INFN Sezione di Perugia and Università di Perugia, I-06100 Perugia, Italy*
[23] *INFN Sezione di Pisa and Università di Pisa, I-56100 Pisa, Italy*
[25] *Rutgers University, Piscataway, New Jersey 08855*
[24] *Rutherford Appleton Laboratory, Chilton, Didcot, Oxon OX11 0QX United Kingdom*
[26] *Sogang University, Seoul, Korea*
[27] *Stanford Linear Accelerator Center, Stanford University, Stanford, California 94309*
[28] *University of Tennessee, Knoxville, Tennessee 37996*
[29] *Tohoku University, Sendai 980 Japan*
[30] *Vanderbilt University, Nashville, Tennessee 37235*
[31] *University of Washington, Seattle, Washington 98195*
[32] *University of Wisconsin, Madison, Wisconsin 53706*
[33] *Yale University, New Haven, Connecticut 06511*
† *Deceased*
[a] *Also at the Università di Genova*
[b] *Also at the Università di Perugia*